UNIVERSITY OF OKLAHOMA
GRADUATE COLLEGE

CHARACTERIZATION OF ELECTRICALLY SMALL, PERIODICALLY TIME-VARYING ANTENNAS

A DISSERTATION
SUBMITTED TO THE GRADUATE FACULTY
in partial fulfillment of the requirements for the
Degree of
DOCTOR OF PHILOSOPHY

By

ADRIAN BAUER
Norman, Oklahoma
2026

CHARACTERIZATION OF ELECTRICALLY SMALL, PERIODICALLY TIME-VARYING ANTENNAS

A DISSERTATION APPROVED FOR THE
SCHOOL OF ELECTRICAL AND COMPUTER ENGINEERING

BY THE COMMITTEE CONSISTING OF

Dr. Jessica Ruyle, Chair

Dr. Hjalti Sigmarsson

Dr. Caleb Fulton

Dr. Sarah Sharif

Dr. Michael Santos

Dr. Kurt Schab

Dr. Kiersten Kerby-Patel

Acknowledgments

I dedicate this work to my parents whose tireless support allowed me to achieve everything. I would also like to thank my advisor, Dr. Jessica Ruyle, for her help and encouragement in my academic pursuit. I, of course, cannot forget the guidance of my committee in the course of this work. Finally, I would like to thank my friends and colleagues who allowed me to appreciate the journey and to persevere through the toil.

Table of Contents

List of Figures

Abstract

Linear, time-invariant (LTI) electrically small receive antennas have well known limits on their gain-bandwidth performance. As a method to circumvent these limits, non-LTI antennas, such as time-varying antennas, have become increasingly popular in the literature. One time-varying design of interest is that of a parametric amplifier implemented on the aperture of an electrically small receive antenna to create a parametrically-tuned receive antenna. This work implements a parametrically-tuned receive antenna in a non-degenerate architecture to achieve a 3.5 times improvement in 3 dB bandwidth and data throughput over a conventional LTI receive antenna using the same physical concentric loop antenna footprint. A suite of measurement methods is discussed in order to characterize time-varying antennas as the common measurement methods applied to LTI antennas makes assumptions regarding reciprocity and measurement frequencies that are no longer valid under the time-varying regime. Included is the development of a novel Y-Factor method for time-varying antennas that considers the impact of internal and external noise at the harmonics on the noise figure of the antenna and the receive system. Finally, the gain-bandwidth trade-off is analyzed for the LTI concentric loop antenna as well as the implemented time-varying antenna.

Chapter 1

Introduction

1.1 Electrically Small Antennas

Electrically small antennas can be incredibly useful for situations in which the size and weight of the receive antenna is restricted. This is more common at lower frequencies such as at UHF and below where the size of typical half-wave resonators becomes prohibitively large. While the small size of these electrically small antennas can be incredibly useful, this comes at the cost of performance. Electrically small antennas have performance limitations in the form of a gain-quality factor limit that is governed by their size. These bounds were first defined in [1] building on work in [2] with the electrical size of the antenna defined by ka where k is the wavenumber and a is the radius of the sphere that totally encircles the antenna. The early endeavors were focused on spherical geometries but later work has expanded the bounds and limits to be more accurate and more encompassing of different antenna geometries [3], [4], [5], [6]. Many electrically small antenna designs have been explored in the literature with a review of many of these designs that approach the limits discussed in [7]. An important assumption made in these limits on the performance of electrically small antennas is that they are passive and linear and time-invariant (LTI). If non-linear or time-varying (non-LTI) effects or components are incorporated into the design of electrically small antennas this assumption is broken and the fundamental limits can be surpassed.

1.2 Non-LTI Receiving Antennas

There recently has been renewed interest in electrically small non-LTI antennas specifically to circumvent the established bounds on gain and bandwidth. Many of these efforts have focused on transmit-based applications such as direct antenna modulation (DAM) where time-varying matching networks are used via switching circuitry to directly modulate the antenna [8], [9]. However, the receive-based non-LTI antenna literature has also grown in parallel to transmit. An example in relation to DAM is coherent antenna modulation (CAM) which can be thought of as the receive implementation of DAM [10]. This new approach seeks to tackle the issue of needing information from the incoming signal to accurately apply antenna modulation techniques using a phase-locked loop and real-time tuning of the antenna.

Another class of time-varying antennas, parametrically amplified electrically small antennas, have been demonstrated in degenerate mode operation [12]. While degenerate mode operation can lead to higher performance in certain cases, the phase relation that exists between the signal and the pump frequencies leads to difficulty in receive applications [13]. The degenerate parametrically amplified antenna in [11] has been shown on transmit and posited to function on receive as well but no receive results are shown. The receive characteristics would be severely degraded as previously mentioned due to the reliance on the phase relationship between the signal frequency and the pump frequency. Parametric upconversion designs have also been shown such as in [14] that convert the lower frequency incoming signal to a higher frequency for enhanced receiving capability. A downside with this

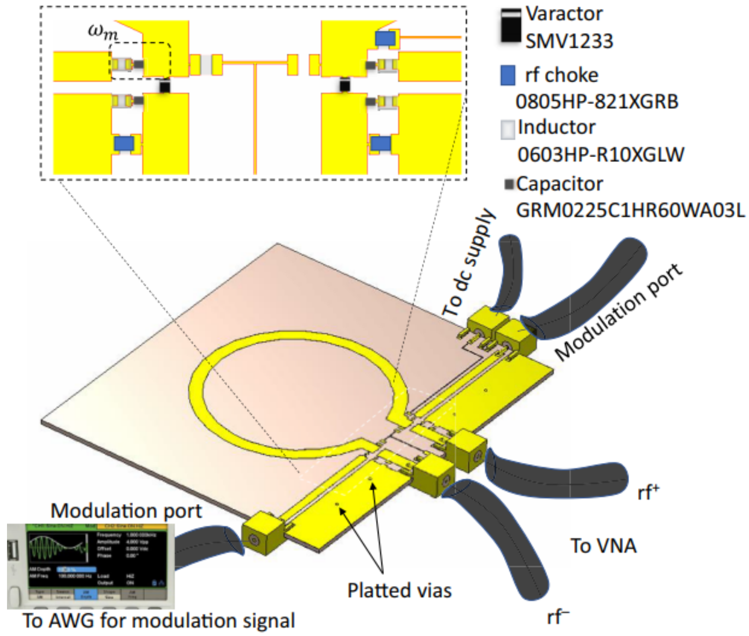

Figure 1.1: Degenerate parametrically amplified transmit antenna from [11] using a DC-biased varactor which is pumped and made time-varying via an arbitrary wave generator off-board.

method is that it no longer is a simple process to convert from using an LTI antenna to the proposed time-varying antenna. The receive system must be designed at the higher, upconverted frequency instead of the incoming frequency which an LTI antenna would operate at. This greatly increases the complexity of upgrading any existing system and higher frequency receive systems can be less forgiving and more expensive to implement as lumped elements become less usable. In addition, a non-classical parametrically amplified antenna in [15] includes an implementation using two different pump frequencies to obtain increased bandwidth and gain over standard electrically small antennas. This two pump solution does indeed improve the performance of the receive antenna, but the complexity of the design is increased compared to more conventional single pump parametric amplifier-based antennas.

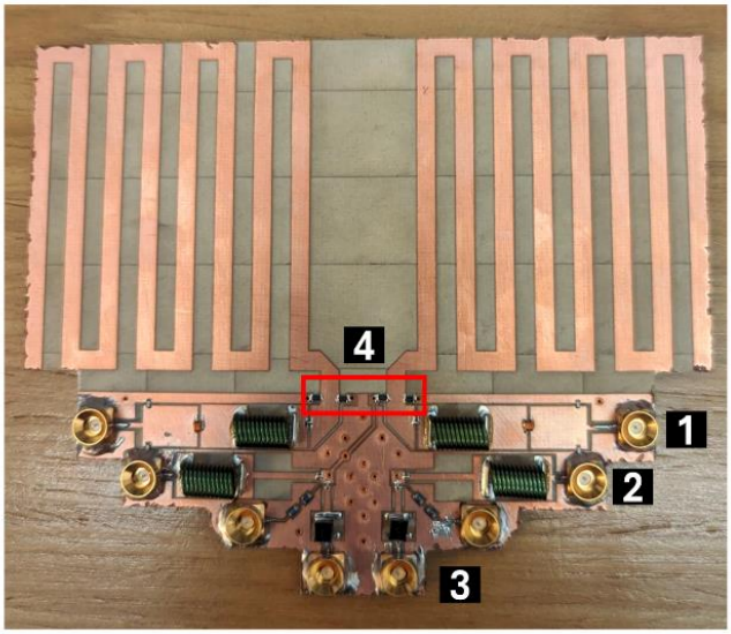

Figure 1.2: Double pump parametrically amplified antenna from [15] with the signal port marked 1, the two different pump ports marked 2 and 3, and the time-varying varactors marked 4.

Many of these recent forays into electrically small non-LTI antennas have been made possible by improvements in the understanding of non-LTI elements and their interactions with antennas as well as the development of new simulation techniques. Historically, accurately simulating these non-LTI antennas have been difficult due to computational limitations and the lack of support for antennas in many commercial solvers capable of also simulating non-LTI components. Recent advancements in antenna modeling methods capable of also modeling non-LTI components such as CMMoM have allowed further investigation into time-varying antenna designs [16]. Most commercial products, however, either don't support non-LTI components, such as ANSYS HFSS, or don't have the ability to accurately model complicated antenna designs using a full wave solution, such as Keysight ADS. There are time-domain based solvers such as XFDTD, but they have less robust built-in models and provide less flexibility in simulation style. To mitigate some of these issues, this work uses a method to combine HFSS for simulating complex antenna geometry while leveraging ADS to simulate the antenna as well as any LTI or non-LTI components as a cohesive circuit in both the frequency domain and the time domain [17]. The ability to simulate in the time domain is a key tool that can be used to easily send modulated signals through the design under test and can help identify potential instabilities that might otherwise be hidden in typical frequency domain simulations. This instability investigation in the time domain is especially important in the parametric amplifier based antenna design showcased in this work.

In addition to the advances in simulation that have allowed for more rapid development of these new non-LTI antennas, improved component technology has allowed for the complex on-aperture loading of antennas. High linearity hyperabrupt voltage dependent capacitors, or varactors, like the ones used in this work, the Skyworks SMV1232, were not widely available when parametric amplifiers were first being developed in the 1960s [18]. These more modern varactor components have the advantage of being smaller, less lossy, and boast a larger linear tuning range than those available earlier [19]. These characteristics allow for increased performance of parametric amplifiers which can be highly sensitive to loss in the time-varying capacitance at specific frequencies [20].

With this recent explosion in the investigation of non-LTI electrically small antennas as a way to improvement gain-bandwidth performance over their standard LTI counterparts, a formal test suite of measurements are needed to accurately measure and compare performance.

1.3 Measurement of Non-LTI Receiving Antennas

While the measurement methods of LTI receive antennas are well known, many of these same methods cannot be directly applied to non-LTI antennas. This is due to the reliance of LTI properties such as reciprocity for many of the standard LTI antenna measurement methods. New methods must be developed to fully characterize the performance of non-LTI antennas on receive, with this work focusing on measuring time-varying, electrically small receive antennas. These new measurement methods are outlined in this work and can also be applied to LTI antennas, allowing for direct comparisons in performance between non-LTI and LTI antennas.

Some key parameters of interest for typical electrically small receive antennas are bandwidth, gain, and noise figure. The maximum matching bandwidth of electrically small antennas specifically and highly reactive circuits generally compose a limiting factor governed by the Bode-Fano limit [21]. As such, matching – which impacts bandwidth and gain – is critical when discussing and measuring electrically small antennas.

For LTI antennas, the realized gain across frequency – and therefore the 3 dB bandwidth – are identical on both transmit and receive due to reciprocity. This is why on receive, realized gain, which is a transmit characteristic rather than a receive one, is measured. However, non-LTI antennas do not inherently possess reciprocity and must therefore be described on receive using only receive characteristics such as realized effective aperture. Realized effective aperture is a measure of a receive antenna's ability to capture energy from an incoming plane wave and is measured in units of dBsm or dB relative to a square meter [22]. Modifications to realized effective aperture must be made to include the cross-frequency coupling inherent in non-LTI designs which is discussed in more depth in 5.1.1.

The noise figure of electrically small antennas is minimally discussed in practice but is well documented in the literature [23]. Since most electrically small LTI antennas are passive, deriving the noise figure of the physical device is straightforward and relies only on the antenna's radiation efficiency, mismatch efficiency, and the physical temperature of the antenna. In addition to the noise contributed to the receive system due to the loss of the antenna itself, antennas couple noise into the system from the outside environment which requires additional consideration. These external noise sources can vary from the noise generated by the cosmic background radiation, to the noise radiated from the sun, to man-made noise among other sources [24]. The modeling of this noise and the effects of it on the overall receive system are explained in 2.2.2. Measuring the noise figure of non-LTI antennas is vital as it no longer can be easily calculated based on radiation efficiency. In addition, non-LTI antennas can couple in noise from harmonics and intermodulation products into the observation frequency greatly increasing the complexity of the antenna's apparent noise figure [25].

1.4 Motivation

This dissertation seeks to address the lack of standardized testing for electrically small, time-varying receive antennas by implementing and streamlining a mixture of existing methods – such as cross-frequency effective aperture and modulated signal testing – as well extending LTI-based measurement methods for novel application to time-varying antennas. In addition, the first implementation of a negative resistance, non-degenerate parametrically-tuned receive antenna in the literature is outlined, fabricated., and testing according to the measurement methods in this work.

1.5 Outline

This work encompasses the implementation and measurement of a parametrically-tuned receive antenna based on a parametric amplifier design as well as an investigation into the matching of state of the art LTI antennas. In Ch. 2, some background information regarding basic parametric amplifier theory and receive system noise is presented to provide a solid foundation from which the rest of the work can be understood. The implementation and fabrication of the parametrically-tuned receive antenna prototype and a comparison LTI antenna of the same physical footprint is showcased in Ch. 3 along with the simulation method used in their design. Different matching techniques for the LTI comparison antenna are investigated in various noise environments for their effect on signal-to-noise ratio (SNR) and modulated signal error vector magnitude (EVM) in Ch. 4. In addition, a brief overview of matching considerations for the parametrically-tuned receive antenna is presented to aid in the realization of future designs. In Ch. 5, a streamlined measurement method for measuring cross-frequency effective aperture of antennas is shown with results provided for the parametrically-tuned receive antenna and the LTI antenna. The reception of modulated signals is then investigated in Ch. 6 as a method to corroborate the findings in Ch. 5 and ensure the measured bandwidth is usable for data throughput. The noise characteristics of the LTI and parametrically-tuned receive antenna are explored using an extension of the Y-factor method developed specifically for electrically small antennas in Ch. 7. The gain-bandwidth trade-off trends of the parametrically-tuned receive antenna and the comparison LTI antenna discussed in Ch. 8 and examined for their differences. Finally, a brief review of the findings and novel methodologies used in this work is presented in Ch. 9.

Chapter 2

Background

2.1 Fundamentals of Parametrically-tuned Receive Antenna

Parametrically-tuned receive antennas are fundamentally time-varying in nature. They rely on a time-varying reactance in order to achieve amplification, and in practice are active devices. As such, these devices are no longer linear and time-invariant (LTI) which complicates their discussion and measurement. Receive gain is no longer a property that can be measured for a non-LTI antenna as it is formally defined as a transmit characteristic of antennas. However, LTI antennas leverage reciprocity to discuss gain on receive as well [26]. Non-LTI antennas are not reciprocal by default meaning that received power measurements must instead focus on figures of merit that are receive-based only–primarily effective aperture. Effective aperture is a receive measure that describes the ability of an antenna to capture power from an incoming wave and is treated as an effective area [26]. The effective aperture in general is given by

$$A_e = \frac{P_T}{W_i}, \tag{2.1}$$

where P_T is the power delivered to the terminals of the receive antenna, W_i is the power density of the incident wave, and A_e is the resulting effective aperture in square meters [26]. For LTI antennas, this can be related to gain with

$$A_e = \frac{\lambda^2}{4\pi} G, \tag{2.2}$$

where λ is the wavelength of the observation frequency and G is the gain of the LTI antenna. In addition, to capture behavior at frequencies other than the signal frequency, such as harmonics, cross-frequency effective aperture is needed. Cross-frequency effective aperture measures how effectively the receive antenna captures power at the signal frequency as well as at non-signal frequencies from an incoming signal [25] and is discussed in more depth in Ch. 5.

To better understand how a non-LTI antenna is not automatically reciprocal a simple derivation of antenna reciprocity is presented from [26], building upon the Lorentz Reciprocity Theorem [27]. Assume a system exists consisting of two antennas, a generator, and a load. The two antennas–one acting as the transmitter and the other as the receiver–have input impedances of Z_1 and Z_2. The generator has impedance Z_g and is assumed to be conjugately matched to the transmit antenna for simplicity while the load has impedance Z_L and is also assumed to be conjugately matched to the receive antenna. This system together creates a network with the transfer admittance represented by Y_{21}. The transmit antenna accepts power from the generator equal to

$$P_1 = \frac{1}{2}\text{Re}[V_1 I_1^*] = \frac{1}{2}\text{Re}\left[\left(\frac{V_g Z_1}{Z_1 + Z_g}\right)\frac{V_g^*}{(Z_1 + Z_g)^*}\right] = \frac{|V_g|^2}{8R_1}. \tag{2.3}$$

The power delivered to the load is then

$$P_2 = \frac{1}{2}\text{Re}[Z_2 (V_g Y_{21})(V_g Y_{21})^*] = \frac{1}{2} R_2 |V_g|^2 |Y_{21}|^2, \tag{2.4}$$

with the ratio of power between the two being

$$\frac{P_2}{P_1} = 4R_1R_2|Y_{21}|^2. \tag{2.5}$$

The transmit and receive antennas can then be swapped giving the power ratio

$$\frac{P_1}{P_2} = 4R_2R_1|Y_{12}|^2. \tag{2.6}$$

Antenna reciprocity then holds when $Y_{12} = Y_{21}$. This symmetry about the diagonal in the admittance matrix has been shown to hold for any general input and output signals only when the system is time-invariant [28]. Time-varying networks in general have impulse responses that depend on the time since the system was excited as well as the instant of measurement [29], meaning that transmit and receive properties examined at different times are not guaranteed to be symmetric. Reciprocity can, however, hold for periodically time-varying systems under certain circumstances [29].

Reciprocity can also be proven with receive power measurements for an antenna. The antenna under test–in this case the time-varying antenna–can be operated as a receive antenna receiving a signal from a standard, reciprocal LTI antenna and source. This results in some power transfer to the load according to the network's transmission coefficient, S_{21}. The antenna under test can then swapped to be the transmit antenna and the test repeated to find the transmission coefficient, S_{12}. If $S_{21} \neq S_{12}$, then the antenna under test is not reciprocal, assuming the medium of propagation in the network is reciprocal.

2.1.1 Parametric Amplification

Parametric amplifiers have been studied in the literature for decades and provide the basis for the parametrically-tuned receiver prototype used in this work. Therefore it will be useful to review the fundamentals of parametric amplification to better understand the parametrically-tuned receive antenna. Much of the basic negative resistance parametric amplifier theory provided here is based on work in [20].

The example parametrically-tuned receiver showcased in this work is based on a negative resistance non-degenerate parametric amplifier architecture. Parametric amplifiers make use of a nonlinear or time-varying reactance to move power from a pump frequency to another frequency of interest governed by the Manley-Rowe relations [30]. Since the amplification occurs–at least theoretically–through a purely reactive means, parametric amplifiers should have a low noise figure when compared to other amplifiers. By not relying on a noisy resistance, the noise of these amplifiers can be pushed to be extremely low, indeed close to the quantum noise dominated regime [31]. This theoretically superior noise performance has resulted in great interest in microwave engineering especially as diode quality factors have increased and non-linear and time-varying simulation methods have improved.

The parametric amplifiers discussed in this work make use of three main frequencies of interest in their operation: the signal frequency, f_s, the pump frequency, f_p, and the idler frequency f_i. The idler frequency is the first difference harmonic between the pump and signal frequency and is defined as $f_i = f_s - f_p$. This resulting idler frequency does become negative as the pump frequency is larger than the signal frequency. The negative idler frequency is then flipped over to the positive frequencies. As such it can be helpful to instead discuss the idler frequency as $f_i = |f_s - f_p|$ for general discussion [20]. The power at the pump frequency–which is assumed to be much larger than the power present at the signal or idler frequencies–is transferred to the signal and idler frequencies in a cross-frequency coupling behavior [13]. This power transfer is represented in a circuit model as a negative resistance to ease analysis.

The reactive element used for the parametrically-tuned receiver discussed in this work is a time-varying capacitance realized with a varactor. The varactor is DC-biased to obtain a certain center capacitance and then pumped around this center capacitance using power from the pump frequency. This results in a time-varying capacitance modeled by

$$C(t) = C_0(1 + \gamma \sin(\omega_p t)), \tag{2.7}$$

where C_0 is the static capacitance of the varactor when it is purely DC-biased, γ is the modulation factor of the time-varying capacitance pumped at frequency ω_p [13]. It should be noted that the above relation only holds if the varactor is varied in a linear or a weakly non-linear region of operation. If the pumping of the varactor results in a strongly non-linear relationship between the applied voltage and the capacitance of the varactor, more terms will be needed to accurately define the time-varying capacitance [13].

The modeling of the parametric amplifier in this way gives rise to the circuit schematic shown in Fig. 2.1 with different branches corresponding to resonators for the signal, idler, and pump frequencies. Each branch corresponding to the different frequencies are ideally isolated from one another and interact on the time-varying capacitance. It should be noted that a resonator for the pump frequency is not strictly necessary in theory, but in order to deliver power efficiently to the time-

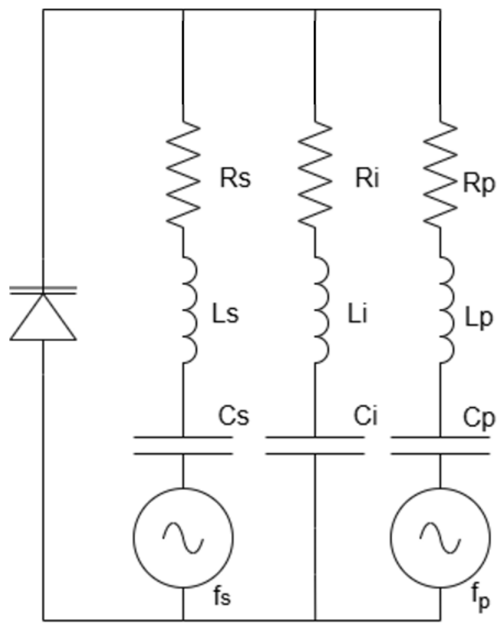

Figure 2.1: Circuit model of the general parametric amplifier. The pump resonance is not strictly necessary in theory with an idealized time-varying capacitance, but for a realistic implementation with a varactor, the pump resonance is necessary for efficient power transfer. Note that the bias circuitry for the varactor is omitted for simplicity.

varying capacitance a resonance at the pump frequency is recommended.

Degenerate Parametric Amplifier

Degenerate parametric amplifiers are a subset of the general parametric amplifier and rely on the idler frequency falling directly on or very close to the signal frequency. This occurs when the pump frequency is approximately twice the signal frequency. Since the signal and idler frequencies are effectively the same, the circuit diagram can be further simplified to the one shown in Fig. 2.2a where the signal and idler branches are merged into one. Again, the resonance at the pump frequency is not strictly necessary, but it is heavily recommended to ensure efficient power delivery to the time-varying capacitance. Looking at the frequency spectrum

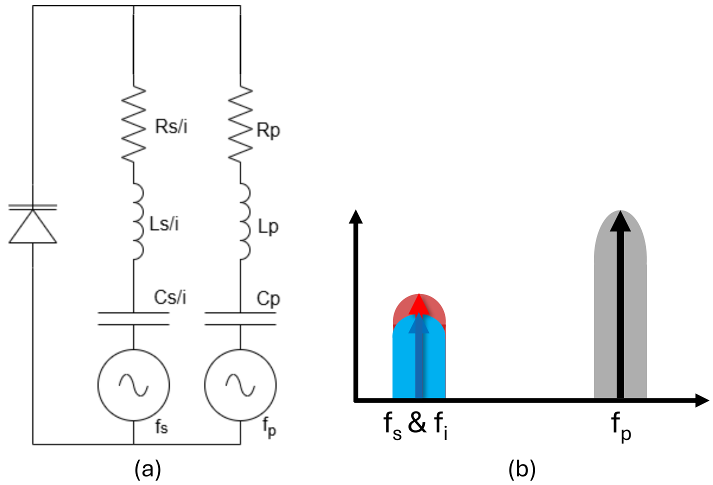

Figure 2.2: (a) Simplified circuit model of a degenerate parametric amplifier with an added pump resonance branch for efficient power transfer to a realistic varactor. Note that the bias circuitry for the varactor is omitted for simplicity. (b) Frequency overview of a degenerate parametric amplifier.

of the parametric amplifier seen in Fig. 2.2b, the signal and idler frequencies are on top of each other as expected since $f_i = |f_s - f_p| = f_s$ in the degenerate case. The idler harmonic and the signal existing at approximately the same frequencies results in potential constructive or destructive interference between the two. To ensure constructive interference between the two, which bolsters the signal level and maximizes performance, the pump and the signal must be in phase. On receive, ensuring the signal and the pump, and therefore the idler frequency, have the same phase greatly increases the complexity of the receive system. For receive systems that deal with modulated signals, the phase-sensitive nature of degenerate parametric amplifiers can lead to distortions in the received signal [32]. In addition, due to the idler frequency flipping from the negative frequencies to the positive frequencies, the idler is a mirrored version of the signal frequency. This can lead to additional distortion which can be mitigated at the cost of only using half the available bandwidth of the parametric amplifier or parametrically-tuned antenna such as

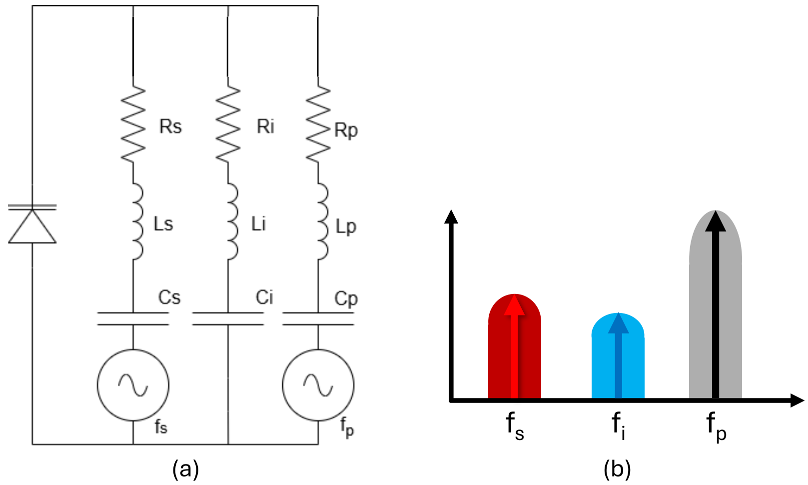

Figure 2.3: (a) Simplified circuit model of a non-degenerate parametric amplifier with an added pump resonance branch for efficient power transfer to a realistic varactor. Note that the bias circuitry for the varactor is omitted for simplicity. (b) Frequency overview of a non-degenerate parametric amplifier.

the signal content and the mirrored idler content do not overlap.

Non-Degenerate Parametric Amplifier

In contrast to the degenerate parametric amplifier, the non-degenerate amplifier does not have a reliance on the phase relationship between the pump and signal frequencies. The pump frequency no longer has to be approximately twice the signal frequency and can instead be chosen with few restrictions. This results in the need of an extra branch and resonator for the idler frequency compared to the degenerate case as seen in Fig. 2.3a which somewhat increases the complexity of the parametric amplifier. In addition the idler frequency no longer falls on top of the signal frequency in the frequency spectrum as demonstrated in Fig. 2.3b. This results in the maximum gain achievable by the non-degenerate parametric amplifier being less than that of the degenerate architecture as it cannot take advantage of any constructive interference between the idler and the signal. However, due to the phase agnostic relationship between the pump and signal frequencies, the non-degenerate architecture can be used to receive phase modulated signals with no additional constraints on the incoming signal. This makes the non-degenerate parametric amplifier more readily applicable to receive mode operation compared to the degenerate case.

Implementation on Aperture

The performance of parametrically-tuned receive antennas in terms of receive effective aperture and bandwidth is reliant on a number of parameters similar to those of standard parametric amplifiers. The maximum transducer gain of these time-varying antennas is given by

$$G_t^{max} = \frac{4R_L R_s}{[R_s^{net}(1 - |\gamma|^2 Q_s^C Q_i^C/4)]^2}, \tag{2.8}$$

where R_L is the load resistance, R_s is the resistance of the physical antenna itself at the signal frequency, and γ is the modulation factor of the time-varying capacitance [33]. R_s^{net} is the total resistance of the antenna at the signal frequency while Q_s^C and Q_i^C are quality factors associated with the signal frequency and idler frequency respectively. The maximum fractional bandwidth is given by

$$b = \frac{r_\omega(1 - \overline{R})}{\sqrt{(Q_i\overline{R} + r_\omega Q_s)^2 - Q_i^2(3\overline{R}^2 - 4\overline{R} + 1)}}, \tag{2.9}$$

where $r_\omega = \frac{\omega_i}{\omega_s}$ is the ratio of the idler and signal frequency, $\overline{R}$ is the normalized negative resistance, and $Q_{s/i}$ are the loaded quality factors for the subcircuits representing the signal and idler frequencies respectively [33]. This maximum transducer gain and maximum fractional bandwidth is discussed in more depth in Ch. 8.

There is of course a trade-off to be had between maximizing the transducer gain of the parametrically-tuned receive antenna and maximizing the bandwidth. This trade-off is also investigated in more detail for the specific parametrically-tuned receive antenna constructed in this work in Ch. 8 where it is compared directly to an LTI concentric loop antenna of the same footprint.

For the parametrically-tuned receive antenna discussed in this work, a few additional constraints on the standard parametric amplifier model must be noted. This time-varying antenna is based on a non-degenerate architecture and must therefore have a resonance for the signal frequency and the idler frequency as with all non-degenerate designs. For the realistic fabricated parametrically-tuned receive antenna, a resonance is provided for the pump frequency as well to facilitate efficient power transfer from the pump source to the time-varying varactor. The signal frequency is selected to be the resonant frequency of a loop antenna when it is tuned to resonance with some capacitance and the idler resonance is generated by a smaller loop inside the signal frequency loop. The pump frequency is made resonant using a lumped element matching network on the aperture which is only necessary for a realizable design. This gives rise to a concentric loop antenna as the base antenna footprint from which the parametrically-tuned receive antenna showcased in this work is buil. More information regarding the specific fabricated structure is provided in Ch. 3.

Parametric Amplifier Stability

A key parameter of interest for any amplifier including parametric amplifiers is stability. The stability of an amplifier ensures that the expected amplification takes place rather than devolving into oscillation. For most amplifier stability analysis, two requirements are examined: Rollett's Proviso and the invariant stability factor

[34].

The invariant stability factor (ISF) test in Rollett's work for a two port network is given by

$$k = \frac{2Re(\gamma_{11})Re(\gamma_{22}) - Re(\gamma_{12}\gamma_{21})}{|\gamma_{12}\gamma_{21}|}, \tag{2.10}$$

where γ_{ij} are either impedance or admittance parameters. For stability, this k must be greater than or equal to one and γ_{11} and γ_{22} must also be greater than or equal to one. This stability test has also been extended to use scattering parameters in the commonly used K-factor test as well as in the μ test which allows for more information on the relative stability of the device under test [35].

Rollett's proviso is assumed to be satisfied in many simple amplifier designs and rarely explicitly tested. The proviso states that the device under test must have poles only in the left half of the complex frequency plane when terminated with either an ideal open circuit or an ideal short circuit when looking at the impedance or admittance, respectively. While this proviso has been examined in specific parametric amplifier designs, a general methodology to examine Rollett's proviso for on aperture parametrically-tuned antenna has been absent until the one recently showcased in [13].

For simple, stand-alone negative resistance parametric amplifiers it can be sufficient to examine the resistance at the port [13]. If the resistance is less than zero then the amplifier is unstable, but if the resistance is greater than zero the device can be said to be stable. This simplistic stability analysis cannot easily be extended to all on-aperture parametric amplifiers and the method shown in [13] must be used instead. This is because Rollett's proviso cannot be assumed for all on-aperture implementations and the ISF cannot be easily verified [13]. The negative resistance seen at the port is a function of the modulation factor of the time-varying capaci-

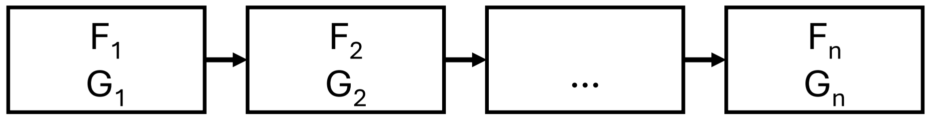

Figure 2.4: Individual components of a radio frequency system in cascade.

tance as well as the quality factor of the device at both the signal and idler frequencies [33]. These parameters are also closely related to the gain of the parametric amplifier resulting in the highest gain being on the cusp of instability.

2.2 Receive System Noise

The performance of a receive system is generally driven by the signal-to-noise ratio (SNR) in that system. As the name suggests, the signal-to-noise ratio is simply the ratio of signal power in the receive system to the noise power in the receive system. While components in the receive chain modify the power of the signal in various ways through gain or loss, each component adds some amount of noise to the system. The gains and/or losses of the subsequent components in the chain are then applied to the noise as well as the signal. Since any gains or losses in the system are applied equally to the signal and the noise and each component adds its own amount of noise, the signal-to-noise ratio in a receive chain always decreases as it progresses through the chain. A key goal for a receive chain is to minimize this degradation in signal-to-noise ratio. The standard method to calculate the degradation in signal-to-noise ratio in a receive chain is outlined below.

2.2.1 Overall Receive System Noise

The noise factor of a radio frequency system measures the decrease in the signal-to-noise ratio as a signal travels through that system. The more commonly cited noise figure is simply the noise factor in dB scale. A typical RF system is comprised of multiple components each of which has their own noise factor, F_n as well as an associated gain G_n. This can be represented as in Fig. 2.4, where each component in the system is shown as a block with an individual noise factor and gain. The noise figure of the system is simply the logarithmic analogue to the linear noise factor. It should be noted that for an accurate representation of the system in question, even the noise factor and gain of the transmission lines connecting the components of that system must be taken into account. With the characteristics of all the individual components and transmission lines of the system noted, the total system noise factor can be calculated by

$$F = F_1 + \frac{F_2 - 1}{G_1} + \frac{F_3 - 1}{G_1 G_2} + \frac{F_4 - 1}{G_1 G_2 G_3} + ... + \frac{F_n - 1}{G_1 G_2 G_3 ... G_{n-1}}, \tag{2.11}$$

where F_n is the noise factor and G_n is the gain of each individual component or transmission line in the system chain [36].

From this equation it can be seen that the position of components in the RF system can have a large impact on the system's overall noise factor. The first few components of the system have the largest influence on the system's noise factor with a high individual noise factor and a low individual gain resulting in a much larger overall noise factor. As the first few components are the most important in determining the overall system's noise factor, high gain and low noise factor components should be used at the beginning of the chain if possible.

The noise figure of a passive device is simply the loss of the device, or the inverse of its gain. This includes many different components such as transmission lines and passive filters with the more general equation used to find the noise figure of a mismatched component given by

$$NF = 10\log_{10}(\frac{T}{T_0}\left[\frac{(1-|S_{22}|^2)}{|S_{21}|^2}-1\right]+1), \tag{2.12}$$

where T is the temperature of the component and T_0 is the reference temperature, typically taken as 290 Kelvin [37]. The noise figure of non-passive devices is significantly more involved to calculate and will depend on the specific device. These more complicated noise figures are typically provided by manufacturers for consumer off-the-shelf components and can be measured using a number of techniques including the Y-Factor method discussed in Ch. 7.

2.2.2 Effects of Antennas on Receive System Noise

Many discussions on system noise figure omit the important impact that the receive antenna has on the system's noise performance. The antenna is the first component in a receive chain and governs the maximum signal-to-noise ratio possible in a receiver. Any effects from components after the antenna only serve to degrade the maximum signal-to-noise ratio according to that component's noise figure and gain. For a receive system using a traditional passive LTI antenna, the SNR of the system is given by

$$SNR = \frac{\tau\eta_r S_i}{kB(\tau\eta_r T_a + \tau(1-\eta_r)T_p + T_r)}, \tag{2.13}$$

which defines the SNR a system can achieve based on its antenna, outside noise environment, and receiving system. Here τ is the antenna's mismatch efficiency, η_r is the antenna's radiation efficiency, S_i is the received power of the matched and lossless antenna, k, is the Boltzmann constant, B is the bandwidth of the receive system, T_a is the noise temperature of the matched and lossless antenna, T_p is the reference temperature of the system usually taken to be 290 K, and T_r is the noise temperature of the rest of the receiving system [38]. The noise temperature of the matched and lossless antenna, T_a will be dependent on the RF noise environment external to the receive system as the antenna receives noise from this external environment and delivers it to the rest of the receive system.

External Noise

Noise external to the receive system can have a dramatic impact on the overall noise performance of the system and can easily disrupt the detection or processing of a desired signal. An LTI antenna will receive noise power based on its receive gain across frequency, the same as it would for a defined signal. Meaning that the degradation of the SNR at the terminals of a lossy receive antenna can be represented by

$$F = \frac{S_i/N_i}{S_o/N_o} = \frac{S_i}{kT_aB}\frac{kB(\tau\eta_r T_a + \tau(1-\eta_r)T_p)}{\tau\eta_r S_i}, \tag{2.14}$$

where F is the noise factor or degradation of the SNR at the terminals of the antenna, S_i is the received power of the matched and lossless antenna, k is the Boltzmann constant, B is the bandwidth of the measurement, τ is the antenna's mismatch efficiency, η_r is the antenna's radiation efficiency, T_p is the physical temperature of the antenna, and T_a is the noise temperature of the matched, lossless antenna [38]. This means that T_a is only dependent on the directivity characteristics of the receive antenna and the external noise environment. It can be found with

$$T_a = \frac{\int_0^{2\pi}\int_0^{\pi} T_b(\theta,\phi)D(\theta,\phi)sin\theta d\theta d\phi}{\int_0^{2\pi}\int_0^{\pi} D(\theta,\phi)sin\theta d\theta d\phi}, \tag{2.15}$$

where $D(\theta, \phi)$ is the antenna's directivity as a function of angle, and $T_b(\theta, \phi)$ is the brightness temperature of the external noise environment.

A non-LTI antenna must contend with noise both at and around the signal frequency of interest as well as at any harmonics. In the case of the non-LTI parametric receiver, any noise incident at the harmonics with be mixed down to the signal frequency and amplified. This can have a major impact on the external noise received by the system and must be taken into account. This ability of non-LTI antennas to couple external noise from the harmonics down to the signal frequency is discussed in more depth in Ch. 7.

Internal Noise

A traditional passive LTI antenna contributes internal noise equivalent to the losses apparent on it as with other passive RF components. For an antenna this can be described by

$$T_{AntLoss} = T_{pr}\tau_r(1 - \eta_r), \tag{2.16}$$

where $T_{AntLoss}$ is the noise temperature of the lossy antenna, τ_r is the antenna's mismatch efficiency, η_r is the antenna's radiation efficiency, and T_{pr} is the physical temperature of the antenna. In general, the lossier an LTI antenna, the more internal noise it generates. A similar idea is true for non-LTI antennas, but the definition of efficiency is not clear in this case so noise must instead be calculated based on loss resistance rather than radiation efficiency. In addition, similar to external noise, a non-LTI antenna must contend with non-negligible internal noise–such as thermal noise–at both the signal frequency as well as at all the harmonics. The internal noise generated at the harmonics is also coupled down to the signal frequency and is discussed in Ch. 7.

2.2.3 Parametric Amplifier Noise

Parametric amplifiers are known for their low noise due to relying on a, theoretically, only reactive element for amplification. Traditional transistor-based amplifiers in contrast have some inherent reliance on resistance and as such are noisier in the most simplified case. In addition to being primarily reliant on only a reactive element, phase-sensitive degenerate mode designs are especially low noise in certain circumstances due to noise-squeezing [39]. This is a method most common in parametric amplifiers for use with quantum signals whereby noise is squeezed into one of the quadratures of the signal. This sacrifices the signal-to-noise ratio in one of the quadratures to improve it in the other, allowing for ultra low noise measurements.

Noise in the general parametric amplifier is highly dependent on the pump-to-signal frequency ratio and the quality factor of the diode(s) used in the design [40]. This means that small increases in the series resistance or loss in the diodes that are typically used to implement parametric amplifiers can result in large increases in the noise figure of the device. As such, it is imperative to choose diodes with low loss at both the signal and idler frequencies to ensure the fabricated parametric amplifier is as low noise as possible. In addition to thermal noise from the diode, noise from the pump source can couple down into the signal frequency and add to the apparent noise figure of the amplifier. This means signal generators, which might be used as the pump source for parametric amplifiers or receivers during preliminary testing, can be a major source of noise as they typically use noisy wideband amplifiers [12]. The pump as a source of noise has been noted as an issue in [12] and is discussed in more depth in Ch. 7 along with mitigation efforts to reduce the effects of this pump noise.

2.3 LTI Antenna Measurements

There are a number of parameters of interest to characterize a typical LTI receive antennas. These parameters include receive gain or receive effective aperture and their associated patterns, bandwidth, and mismatch, as well as more advanced metrics such as signal fidelity. While this work does not focus on antenna patterns of time-varying antennas and instead focuses on broadside receive characteristics, the effective aperture, bandwidth, and signal fidelity are all investigated in addition to the noise figure of the active, time-varying antenna proposed. The mismatch of a time-varying antenna is ill-defined but the S-parameters of the non-pumped antenna design are still used to aid tuning with a procedure outlined in Ch. 3.

The most common characterization is the receive gain and radiation pattern of the antenna. This can be done using near-field measurements which are then transformed to far-field patterns [41] or the more straightforward far-field measurements. The receive effective aperture measurement method used in this work is based on the far-field gain-transfer or gain-comparison method where a calibrated antenna with known gain or effective aperture characteristics is used to associate a gain or effective aperture across frequency to an antenna under test [26]. While in LTI settings this can be done using a network analyzer measuring the same received frequency as the transmitted frequency, the method used in this work makes use of a spectrum analyzer to better measure the cross-frequency behavior of time-varying antennas as a function of transmit frequency. More information on this cross-frequency effective aperture measurement which is based on work in [42] can be found in Ch. 5.

Receiving modulated signals carrying information is of great interest for modern systems that deal with communications. As such, it can be helpful to test the capability of an antenna to receive these modulated signals without large distortion. A number of methods and measurements have been carried out to characterize the impact of an antenna under test on the error vector magnitude or EVM of the associated modulated signal [43], [44], [45], [46]. A method similar to one used in [47], where the data rate of the transmitted signal is increased while measuring EVM, is also used in this work in Ch. 6 as an additional investigation of the bandwidth of the antennas under test. This type of measurement method of directly measuring the EVM from the spectrum analyzer was preferred over methods directly investigating the signal distortion caused by the receive antennas such as in [48] due to the easier measurement implementation.

The noise characterization associated with loss for LTI antennas is fairly straightforward in theory and can be directly calculated given an antenna's radiation efficiency and mismatch efficiency as seen in Eqn. 2.16. For the large, directive antennas used in radio astronomy it can be helpful to measure the noise figure associated with the loss of the antenna in situ using a modification of the Y-Factor method which is commonly used for two-port devices [49], [50]. A novel extension of this antenna Y-Factor method is used in this work to characterize the noise contribution associated with the loss and cross-frequency coupling behavior of time-varying antennas in Ch. 7.

2.4 Conclusions

The foundational information regarding parametric amplifiers covered in this chapter helps set the stage for the parametrically-tuned receive antenna covered in the next chapter. This time-varying antenna, which is based on a non-degenerate parametric amplifier design, serves as the primary prototype for the measurement suite outlined throughout this work. Some basic characteristics of noise in receive systems has also been discussed as this features heavily in the matching discussion for LTI antennas in Ch. 4. The cascading of noise through a receive chain and sources of internal and external noise are also important aspects in the noise characterization of time-varying antennas investigated in Ch. 7 and the results of the modulated signal testing seen in Ch. 6. With a solid foundation on parametric amplifiers and how noise functions in receive systems, the prototype antennas–both the parametrically-tuned receive antenna and its LTI counterpart–can be examined.

Chapter 3

Time-Varying Parametric Receiver

The design of the parametrically-tuned receive antenna starts with the basic model of the parametric amplifier. Among the major modifications is, of course, the implementation of the amplifier onto the aperture of an antenna. This implementation is not trivial and is detailed below, starting from a more idealized simulated version to the final fabricated and measured prototype.

3.1 Physical Characteristics

The footprint of the base antenna used for the parametrically-tuned receive antenna and the LTI counterpart was chosen to be a loop antenna. Using a balanced design such as a loop antenna means that a large ground plane is not necessary for proper operation and ensures the entire design stays electrically small. A loop instead of a dipole means that loading the antenna is much easier, needing only small gaps in the copper of the loop to support the loading components. This means that the loading components can be placed directly opposite the antenna feed increasing the room available for circuitry. This allows for easy access to the varactors for biasing which would be more complicated if the loading was done at the feed. In addition, the loop is fairly insensitive to objects and components in the center of the

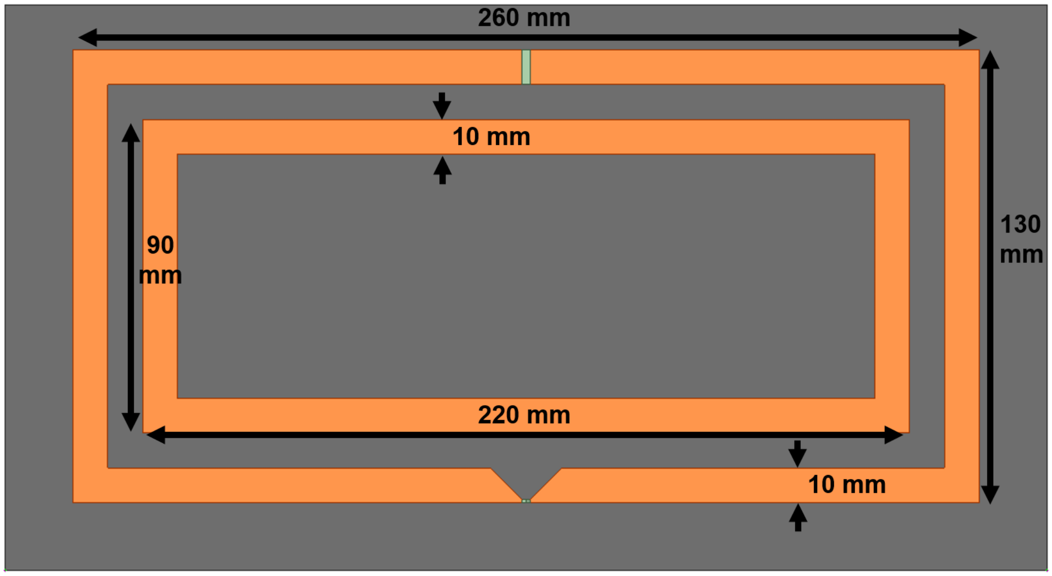

Figure 3.1: Concentric loop antenna configuration that provides the basis for the electrically small loaded LTI antenna design and the parametrically-tuned receive antenna design.

loop, allowing for the easy integration of any supporting circuitry in future designs without increasing the size of the antenna [26].

The main time-varying antenna used for testing is based on a non-degenerate parametric amplifier implemented on the aperture of a concentric loop antenna. The concentric loop antenna consists of two loops as seen in Fig. 3.1. The larger loop is 260mm by 130mm with a conductor width of 10mm while the smaller loop is 200mm by 100mm with the same conductor width of 10mm. The introduction of the smaller inner loop supports a resonance at the idler frequency of the parametrically-tuned receive antenna, approximately 500 MHz. The inner loop was constructed such that the two resonances of the signal and idler frequencies could be modified separately while ensuring the idler frequency was not too high. A higher frequency idler resonance would require a higher frequency pump which would limit the use of lumped elements in the implementation of the pump matching network which serves as the pump resonance. The idler resonance is required due to the non-degenerate architecture of the parametric amplifier which necessitates separate signal and idler resonators.

3.2 Idealized Parametric Receiver

To begin, an idealized model of the more complicated parametric receiver design is helpful to illustrate the main working principles. The main components necessary to implement the idealized parametrically-tuned receive antenna is a representation of the physical antenna and a time-varying capacitance. For the idealized version, the time-varying capacitance can be implemented in Keysight ADS as a symbolically-defined model of a time-varying capacitor as seen in Fig. 3.2 [51]. This time-varying capacitance has a center capacitance set by the static capacitor connect between ports 1 and 3 of the model and a modulation factor set by half the peak amplitude of the voltage source connected to port 2. This model allows for a time-varying capacitance without the need for a physical pump source, greatly simplifying the simulated implementation.

3.2.1 Simulations

The simulation of both the idealized model and the more complicated realized model of the parametric receiver is implemented using a mix of the full-wave solving capabilities of ANSYS HFSS and the circuit solver Keysight ADS. HFSS is used to model the physical structure of the antenna itself as well as find the necessary open-circuit voltages across the loaded ports as a result of an incoming plane wave. This method stems from representing the loaded antenna as a multiport Thévenin equivalent circuit which is itself an extension of representing un-

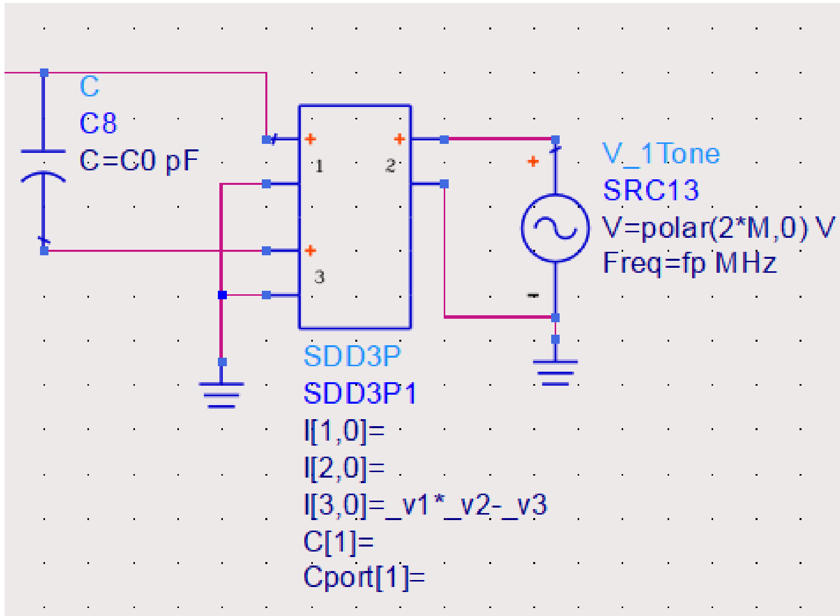

Figure 3.2: Idealized time-varying capacitance implemented in Keysight ADS using a symbolically-defined model approach.

loaded receive antennas as a single port equivalent circuit [17]. By using a Thévenin equivalent circuit for a general receiving antenna, the antenna can be represented by a one port scattering parameter matrix and an open circuit voltage. This is extended in [52] to loaded antennas for a multiport representation where each load on the antenna is represented by a port and an open circuit voltage at that port. Additionally, each feed point on the antenna is also represented as a port with an open circuit voltage. ADS then uses the antenna representation from HFSS–in the form of a two port SNP block and two voltage sources for the prototype showcased here–along with the supporting circuitry to accurate simulate the parametrically-tuned receive antenna. An example of the ADS schematic for the LTI antenna which uses the Thévenin equivalent circuit representation can be seen in Fig. 3.3.

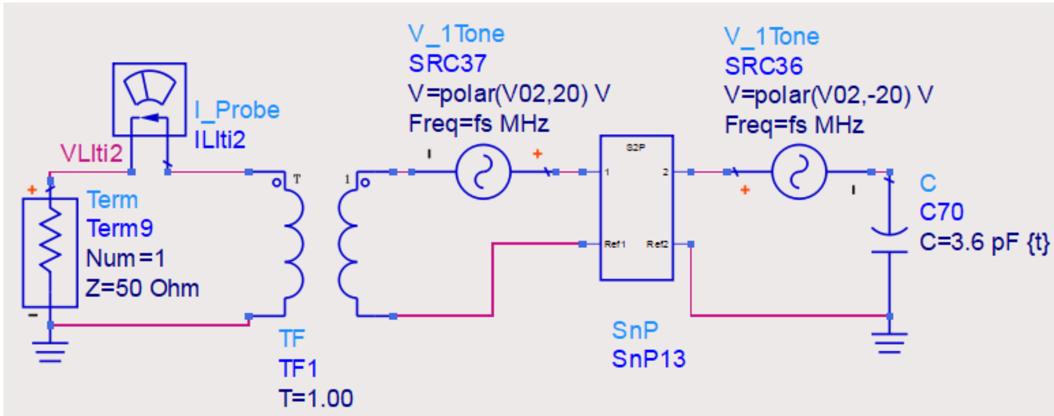

Figure 3.3: Schematic of the LTI antenna in ADS which uses the Thévenin equivalent circuit representation. The scattering parameter matrix and the necessary open circuit voltages for each port are found using HFSS. An ideal transformer is used here as a balun.

HFSS

The physical structure of the base antenna model was constructed in HFSS and is the same for both the LTI and non-LTI case which can be seen in Fig. 3.1. The design is a concentric loop antenna consisting of an inner and outer loop on 60 mil thick Rogers 5880 substrate. The substrate itself does not noticeably impact the behavior of the antenna and was used to ease fabrication and component integration as well as increase physical robustness. The copper is tapered near the feed to better support soldering the components necessary for the feed matching network. In HFSS, a lumped port is inserted, bridging the gap and acting as the main feed. Opposite the feed is a gap in the copper where the loading circuitry is incorporated. For the LTI design this is a simple capacitor, but for the parametrically-tuned design a much larger circuit is implemented here in ADS.

To generate the S-parameter block necessary to accurately represent the antenna in a circuit simulation, lumped ports are used at the feed and the loading site. By using lumped ports on the feed and each loading site on the antenna, the two port

S-parameters–one port for the loading point and one for the feed point–can be extracted from HFSS for use in ADS. The open circuit voltages across each port are also necessary for use in the circuit simulation. These voltages are obtained by creating poly lines across the feed and loading gaps, and using the HFSS fields calculator to find the magnitudes and phases of the voltages across these lines. An incoming plane wave excitation is used as the source generating the open circuit voltages. This wave is traveling in the positive x-direction in reference in Fig. 3.1 and is first incident on the side with the loading components. Plane waves incident from other angles can be used, but the magnitude and phase of the open circuit voltages will change in accordance to the direction of incidence. This particular direction was chosen as it corresponds to broadside and allows for the easiest measurement of the fabricated antenna. The power in this plane wave excitation is then used as the incident power density on the antenna for calculating the effective aperture in simulation. For the concentric loop design, the voltages at the feed and loading points are equal in magnitude and phase and remain consistent across the frequency band of interest.

ADS

The two-port S-Parameter file (S2P) of the physical structure of the antenna generated from HFSS is imported into ADS using an S2P block component. The necessary open circuit voltages found from the full wave solution are implemented using single tone voltage sources with a variable frequency. The magnitude and phase of the open circuit voltages do not vary greatly across the frequency band of interest as shown in Fig. 3.4 so these parameters remain static. The symbolically-defined time-varying capacitance discussed earlier and shown in Fig. 3.2 is added to the second port of the antenna representation while a resistive load is added to the

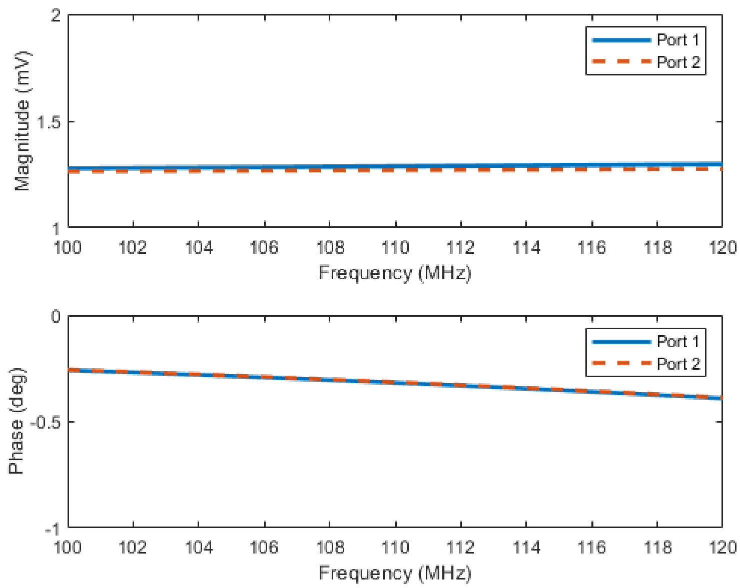

Figure 3.4: Open circuit voltages for the Thévenin equivalent circuit of the concentric loop antenna as a function of frequency.

first port, corresponding to the load and feed ports of the antenna respectively. The schematic of the idealized simulation can be seen in Fig. 3.5 with the time-varying capacitance model and the resistive terminal representing the feed port.

As a part of the ADS simulation process, harmonic balance as well as transient simulations are run. The harmonic balance simulations are significantly faster and allow for more rapid modifications to the prototype designs to improve performance. Transient simulations are used to ensure that the design simulated in harmonic balance is indeed stable. If the transient simulation fails to run completely or if the results of the transient simulation diverge, this points to the design under test being unstable. Therefore transient simulation becomes an incredibly important step in the simulation process to ensure stability that might not be uncovered if work is only done using the harmonic balance simulator. To support the use of transient simulations, the S-parameter information from HFSS discussed in

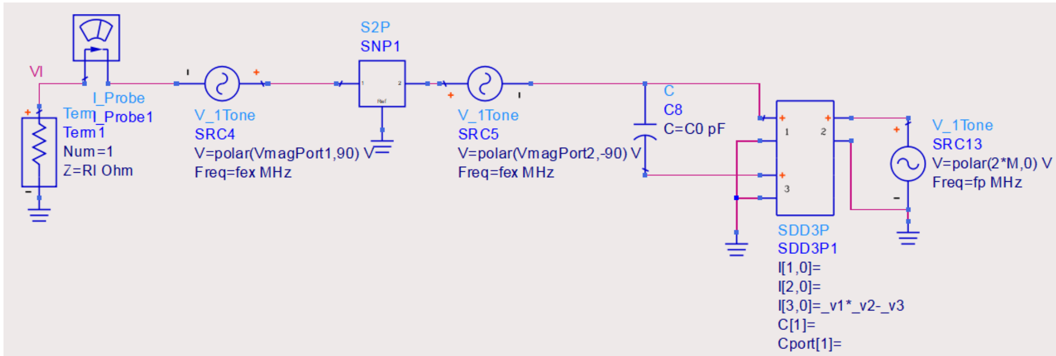

Figure 3.5: Schematic of the idealized parametrically-tuned receive antenna making use of the Thévenin equivalent circuit representation of the concentric loop antenna, a resistive load on the feed port, and a symbolically-defined time-varying capacitance model on the load port.

3.2.1 must incorporate a wider frequency range than one might expect. Since the information in the S2P block is translated into an impulse response for use in transient simulations, high frequency content is necessary to accurately capture small time-domain details in high quality factor structures. Therefore for the S-parameter data used in this work as a part of the Thévenin equivalent circuit representation of the concentric loop antenna, frequency data ranging from DC to 8 GHz was used. This range will likely need to be increased for designs that utilize a higher pump frequency.

3.3 Realized Parametrically-tuned Receiver

The idealized circuit presented earlier does not include many of the elements necessary to create a realizable prototype. Additional modifications to the circuit must be made to model a realistic time-varying capacitor. Varactors are used as the main component in the time-varying capacitor as they can vary their capacitance with voltage. Great care must be taken in varactor choice to balance capacitance swing, linearity, and series resistance. While the capacitance swing provided by a

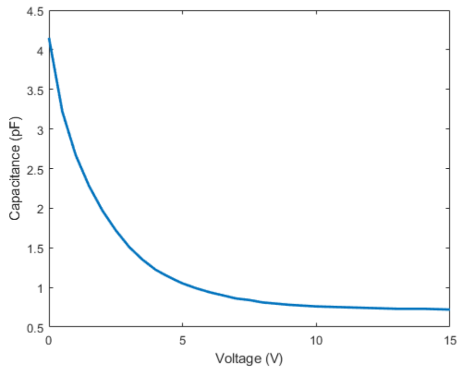

(a) Entire capacitance versus voltage curve for the Skyworks SMV1232 varactor diode.

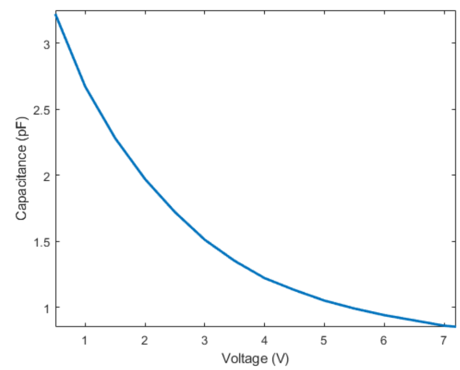

(b) Zoomed capacitance versus voltage curve for the Skyworks SMV1232 varactor diode.

Figure 3.6: The capacitance versus voltage curve for the Skyworks SMV1232 varactor diode. A subset of the full range of capacitances available from the varactor are used to increase the linearity of the component when used in the parametrically-tuned receive antenna.

varactor can be fairly large, the relationship between the applied voltage and the capacitance of a varactor is non-linear. This non-linearity can introduce significant issues in the parametric amplification design such as intermodulation products and must be avoided. A much smaller subset of the capacitance-voltage relationship is used such that it appears approximately linear as shown in Fig. 3.6a. A pair of SMV1232 varactors in parallel are used in the parametrically-tuned receive antenna. By using two varactors in parallel, the capacitance values the varactors provide increase while the series resistance of the two decrease. This decrease in series resistance is important as it subtracts from the negative resistance that powers the parametric amplification. In addition, the lowered series resistance can reduce the noise figure of the parametrically amplified design [40].

While in the idealized design the time-varying nature was baked into the SPICE model, an actual time-varying voltage needs to be applied to the varactors to produce a time-varying capacitance. This time-varying voltage comes from the pump source, which in the case of the prototypes discussed in this work, is a signal generator. To support this pump frequency on the aperture of the receive antenna additional circuitry including filtering, a matching network, and a balun is added. The matching network is necessary to match the 50 Ohm pump port–the standard impedance for instruments such as a signal generator–to the varactors to ensure as much voltage as possible is presented to the varactors to vary them for a given pump power. The more efficient the matching from the pump port to the varactors is, the less pump power is necessary to produce the desired performance. For this particular design, the voltage across the varactors varies from approximately 0.58 V to 7.2 V, producing an only weakly non-linear capacitance curve rather than the fully non-linear relationship that using the full range of the varactor would produce. This was deemed an acceptable amount of nonlinearity as no major nonlinear effects such as intermodulation products were seen. The balun serves to transform the balanced architecture of the antenna aperture to the single-ended port of the signal generator.

Both the LTI and the non-LTI antenna designs are based on a concentric loop and are therefore differential. To accurately represent the differential nature of the design, the reference ports of the S-parameter block are used as the second differential port on each side of the antenna as can be seen in ADS schematic for the LTI in Fig. 3.3.

3.3.1 Circuit Layout

The schematic for the realizable parametrically-tuned receive antenna in ADS can be seen in Fig. 3.7 with different portions of the design highlighted. The different portions include the base antenna representation using simulations from HFSS, a pump bandstop filter, a signal bandstop filter, matching networks for the

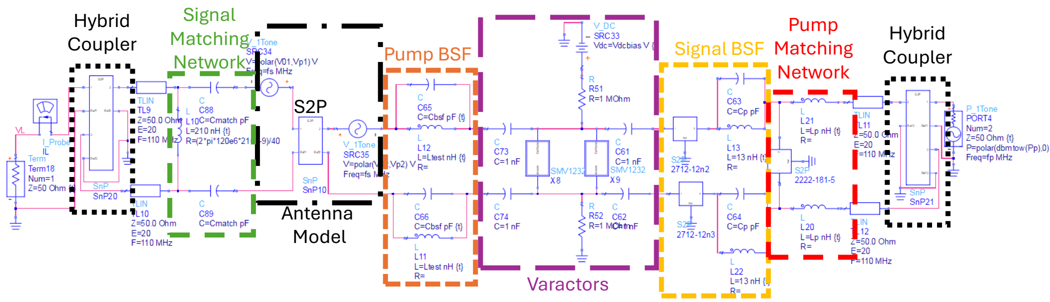

Figure 3.7: Schematic of the realized parametrically-tuned receive antenna in ADS.

pump and receive ports, and hybrid couplers acting as baluns for each port.

The Thévenin equivalent circuit representation of the basic concentric loop antenna is highlighted in black in Fig. 3.7 and consists of the two port scattering parameter model and the two voltage sources. This represents both the physical antenna including the copper and dielectric losses as well as incident power from an incoming plane wave. A differential signal matching network shown to the left of the S2P model seeks to match the impedance of the time-varying antenna as best as possible to the 50 Ohm singled-ended impedance of the signal port. This design of this matching network is discussed in more depth in 4.4.2. On the opposite side of the schematic is the differential pump matching network which matches the 50 Ohm single-ended impedance of the pump port to the varactors in addition to interacting with other lumped elements on the aperture to create a resonance near the pump frequency. This resonance allows for a more efficient power transfer from the pump source to the pumped varactors. Hybrid couplers on both the signal and pump ports serve as a balun solution to allow for interfacing single-ended instruments with the differential antenna aperture. The hybrid coupler on the receive side combine the signal on each branch of the balanced design with a 180 degree phase shift on one of the branches. The opposite occurs on the pump side where the single-ended pump signal is split into two branches with equal magnitudes but opposite phase. On either side of the varactors are bandstop filters. Highlighted in red is the pump bandstop filter which is designed to reject pump power and attenuate it before it reaches the signal port. In addition, this bandstop ensures that as much voltage as possible from the pump source is seen across the varactors to produce a larger modulation factor for a smaller pump power. On the opposite side of the varactors is another bandstop filter, this time for the signal frequency. This bandstop filter rejects at the signal frequency such that the incoming signal does not leak out onto the pump port and instead is direct towards the signal port. Finally, 1 nF capacitors are inserted on either side of the varactors to serve as DC blocks and 1 MOhm resistors serve as RF chokes on the DC bias lines feeding the varactors.

To support a realistic pump source, which in the case of preliminary measurements is a signal generator, an additional resonance must be added to the aperture of the non-LTI antenna. This resonance at the pump frequency is in line with the theory in Ch. 2 and must be designed and tuned to take into account loading from other elements on the aperture. In the case of this prototype, this resonance is generated with the combination of the differential matching network and signal bandstop filter.

The fabricated version of the parametrically-tuned receive antenna needs the transmission lines connecting different components to be as small as possible. An early iteration, shown in Fig. 3.8, used fairly small transmission lines (approximately $\lambda/30$), but this still appeared to detune the design and introduced a shift in the idler frequency. The S-parameters associated with this earlier design can be seen in Fig. 3.9 with port one corresponding to the signal port and port two corresponding to the pump port. As can be seen in S_{22}, there is a high amount of reflection on the pump port around the design pump frequency of 600 MHz. This results in poor power transfer to the varactors, degrading their time variation. In addition, the

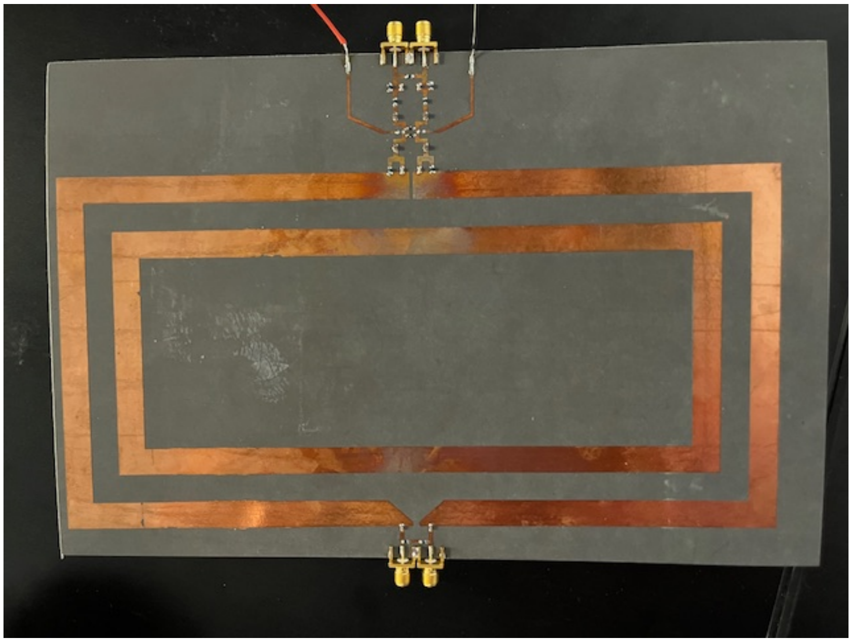

Figure 3.8: Early prototype of the parametrically-tuned antenna with longer transmission lines connecting the components. This iteration makes use of off board hybrid couplers as the balun solution.

idler resonance highlighted in the figure is detuned down in frequency by approximately 100 MHz from the design frequency of approximately 500 MHz. The signal resonance is also slightly detuned in frequency by a lesser amount. The resonances associated with the signal port and shown with S_{11} show less detuning than the resonance associated with the pump port and S_{22}. This is due to the signal side of the design having less overall transmission line length than the pump side implementation. As can be seen from this earlier design, the antenna is fairly sensitive to frequency shifts and parasitics caused by unnecessary lengths of transmission lines. This finding was used to implement the final parametrically-tuned receive antenna prototype with shortened transmission lines and off board hybrid couplers which can be seen in Fig. 3.10. Insets highlighting the components on the aperture of the finalized design are showcased with boxes corresponding to the segments of the circuit shown in Fig. 3.7. In addition to the shortened transmission lines, the

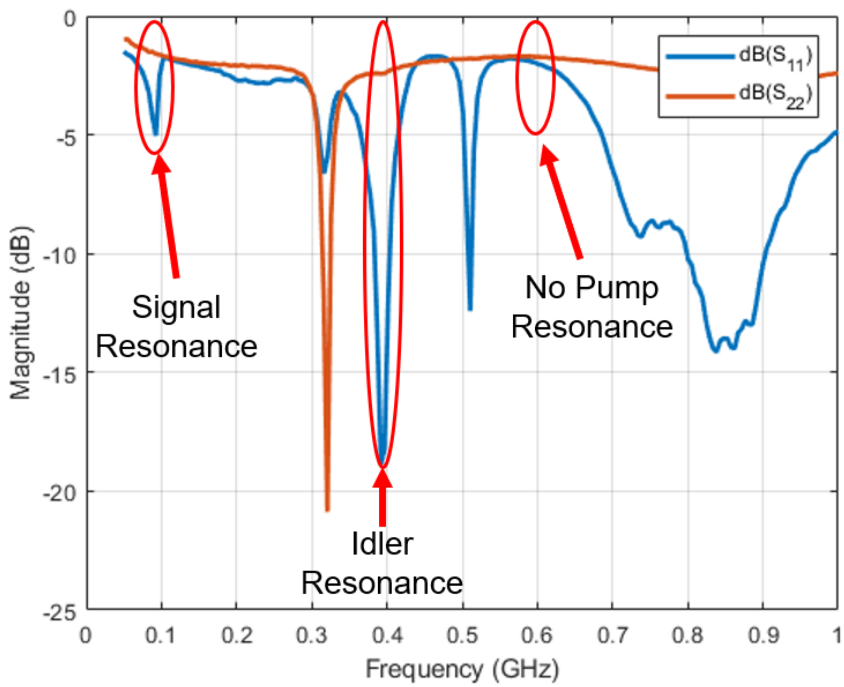

Figure 3.9: S-parameters of the early prototype parametrically-tuned antenna with longer transmission lines connecting the components. Port one corresponds to the signal port and port two corresponds to the pump port.

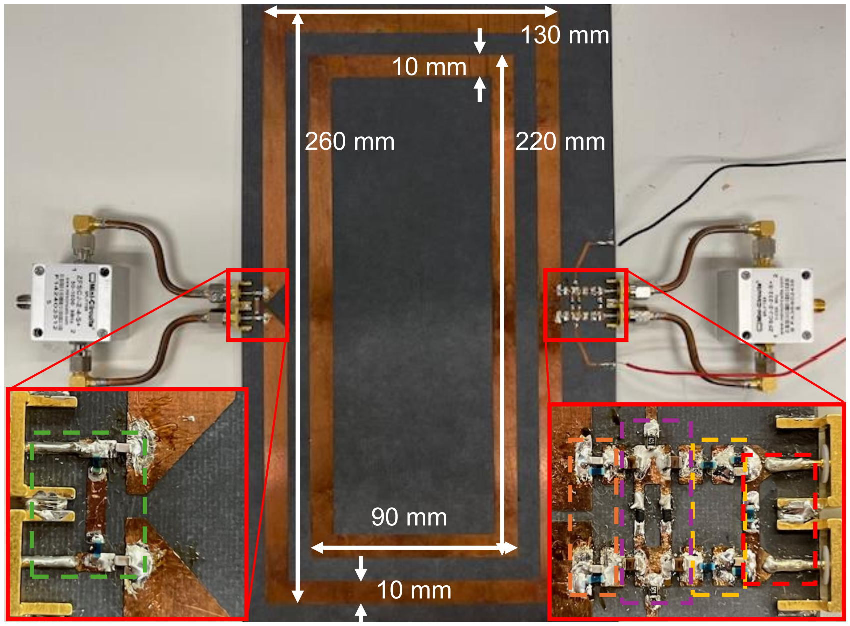

Figure 3.10: Final prototype of the parametrically-tuned receive antenna including the Minicircuits ZFSCJ-2-4-S+ hybrid coupler acting as a balun on the signal side and the Minicircuits ZFSCJ-2-232-S+ hybrid coupler on the pump side.

lengths were modeled in simulation to better account for the frequency shifts. The S-parameters of the finalized design are shown in Fig. 3.11 compared with the simulated results with the signal, idler, and pump resonances highlighted. The signal resonance is at the designed frequency, as are the idler and pump resonances.

3.3.2 Balun Implementation

A number of balun implementations were investigated to transform the differential signal side of the antenna to single-ended and the differential pump side to single-ended. The rest of the receive system, namely the LNA and RTSA used in measurement are single-ended so a balun was necessary to make the transformation. Similarly, the signal generator used as the pump source is also single-ended resulting in a need for a balun on the pump side of the non-LTI antenna as well.

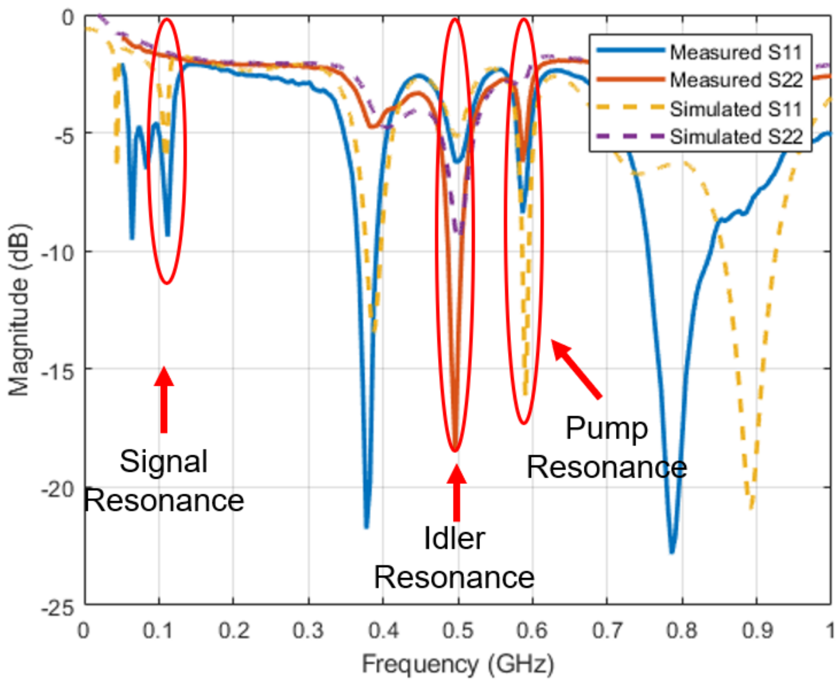

Figure 3.11: S-parameters of the finalized parametrically-tuned antenna with shortened transmission lines. Port one corresponds to the signal port and port two corresponds to the pump port.

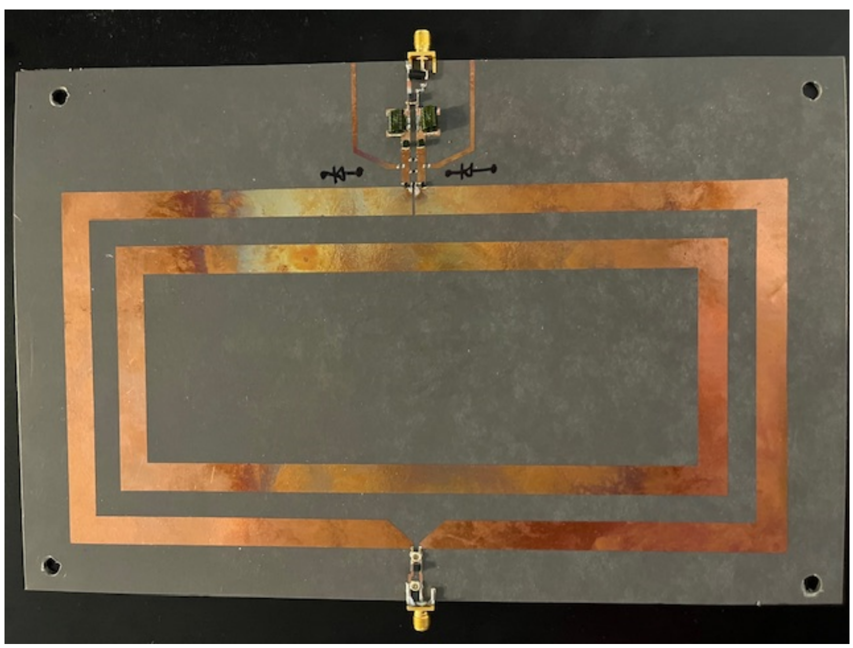

Figure 3.12: Early prototype of the parametrically-tuned antenna with chip baluns used on the pump and receive ports.

The first balun implementation that was prototyped was the use of a chip balun on both sides of the antenna. This parametrically-tuned receiver prototype can be seen in Fig. 3.12. While this solution was able to create an interface between the balanced antenna structure and the single-ended measurement equipment, the loss associated with the balun was significantly worse than expected, resulting in a much lower received effective aperture for both the LTI and the parametrically-tuned receive antenna. This impacted the parametrically-tuned receive antenna more so than the LTI antenna as the parametric amplification is more sensitive to increases in load resistance and on-aperture loss. The sensitivity of the parametrically-tuned receive antenna to on-aperture loss is discussed in Sec. 2.1.1.

The balun implementation that is used in the prototype discussed for most of this work is a hybrid coupler. This was chosen over the transformer implementation as a straight forward solution that suffered from less loss, improving peak effective aperture performance for both the LTI antenna and the parametrically-tuned receive antenna. The chosen hybrid coupler is already implemented as a stand alone, off-aperture component with the signal port hybrid coupler being the Minicircuits ZFSCJ-2-4-S+ and the pump port hybrid coupler being the Minicircuits ZFSCJ-2-232-S+. To connect the off board hybrid couplers to the antenna board, phase-matched semi-rigid cables were constructed to be connected to the two SMA connectors that made up the differential connections for each port. The final prototype design of the LTI comparison antenna including the hybrid coupler can be seen in Fig. 3.13.

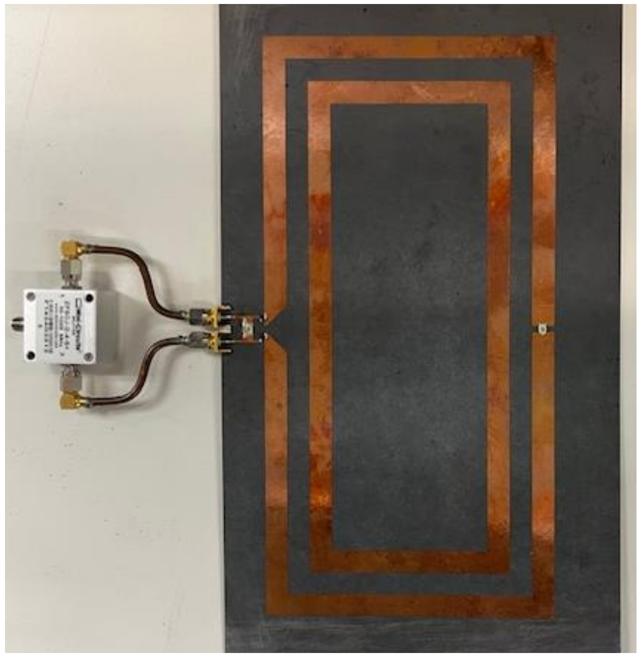

Figure 3.13: Final prototype of the LTI comparison antenna including the Minicircuits ZFSCJ-2-4-S+ hybrid coupler acting as a balun.

3.3.3 Tolerance Analysis

A tolerance analysis using a Monte Carlo simulation was run to assess how sensitive the parametrically-tuned receive antenna is to tolerance in the component values implemented on aperture. Each of the lumped element capacitors and inductors in the time-varying design were included in the analysis with a tolerance of 5%. While the majority of iterations yielded results within 3 dB of the nominal simulation, results from some of the more illuminating iterations of the Monte Carlo simulation of the time-varying antenna can be seen in Fig. 3.14. The base case, shown with the solid blue line, showcases a symmetric received power curve while the other iterations show reduced received power and unequal curves.

The iterations that were impacted the most by tolerance and resulted in the worst performance were ones in which the components on each leg of the balanced antenna design suffered from opposite ends of the tolerance spectrum. For example,

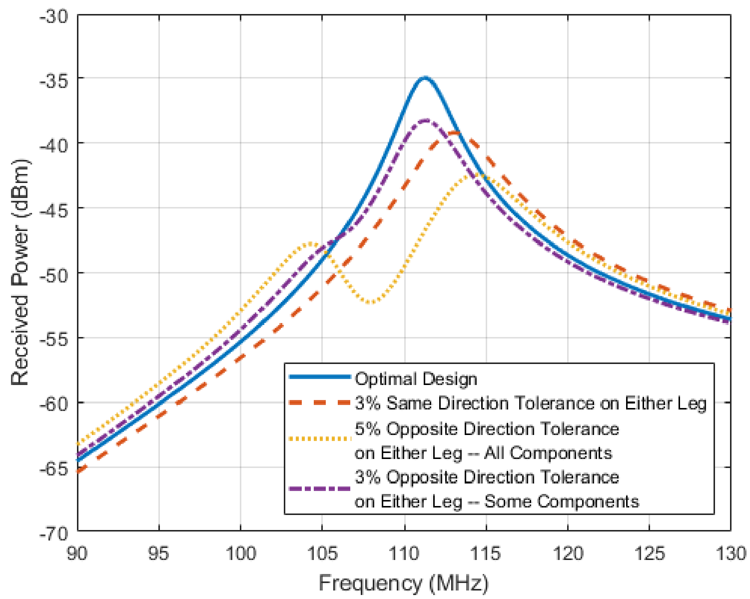

Figure 3.14: Received power results for various iterations of a tolerance analysis done in simulation.

the worst performing result shown in Fig. 3.14, the yellow dotted line, has inductors and capacitors in which one leg of the balanced design has values 5% higher than designed for and the other leg has all values 5% lower than designed for. This negatively impacts the balanced design and results in cancellation of received power. This highlights not only the sensitivity of this particular time-varying design to component tolerance, but also a downside of using a balanced design in conjunction with lumped elements in general. The result shown in the orange dashed line has component values that are mistuned from the optimal design, but the components on opposite legs of the balanced design are mistuned in the same direction. This results in the overall design being shifted in frequency and lower in received power, but remaining balanced and symmetric. In contrast, the result shown in the purple dot-dashed line has a few pairs of components mistuned in opposite directions but not all. This gives a decrease in received power and slight asymmetry due to a bump around 105 MHz, but is not nearly as bad as when every pair of components is unbalanced. In general, the time-varying design is most sensitive to tolerance in the components that compose the pump and signal bandstop filters.

3.3.4 Fabricated Design Tuning

Due to the sensitivity of the design to tolerance as highlighted in the previous section, the fabricated design needed to be slightly tuned to optimize the gain-bandwidth product. The tuning was performed while the antenna was connected to the rest of the receive system and focused on three primary parameters: pump frequency, pump power, and varactor DC bias voltage. The pump frequency was first tuned such that it approximately aligned with the pump resonance seen in the static S-parameters featured in Fig. 3.11. The pump frequency was then slightly adjusted and a brief receive power measurement was taken with an incoming signal before adjusting the pump frequency once more. The goal was to adjust the pump frequency such that the receive power of the incoming signal used during testing was maximized. The adjustment of the pump frequency was done in tandem with small adjustments to the varactor DC bias voltage to ensure that the idler frequency created by the interaction between the pump frequency and the incoming signal frequency landed on the idler resonance of the antenna structure. The varactor DC bias voltage also served to slightly adjust the signal resonance of the time-varying antenna. Finally, the pump power was modified such that the received power from the incoming signal matched the received signal power level of the LTI comparison antenna. The inductor in the signal side matching network could also be used to adjust the amplification and therefore the received signal power level along with the pump power. A higher inductance value in the matching network leads to a higher load resistance presented to the time-varying antenna which increases bandwidth at the cost of amplification. Since the pump power directly affects the voltage swing across the varactors and therefore the modulation factor, it must be limited to ensure that the varactors do not behave strongly nonlinear. During testing and tuning this was checked by reviewing the received power spectrum when an incident signal was received and ensuring intermodulation products were not present. Testing with the time-varying antenna and this receive system has previously shown strong intermodulation products if the pump power was set too high.

3.4 Conclusions

The design of an LTI concentric loop antenna as well as the more complicated parametrically-tuned receive antenna developed from the same footprint has been presented. Details regarding the simulation and fabrication of the prototypes have been discussed including pitfalls regarding the sensitivity of the time-varying design to transmission line lengths. The balun solutions for both of the designs were reviewed and the finalized prototypes of the time-varying antenna and its LTI counterpart was showcased. A tolerance analysis was run on the parametrically-tuned receive antenna and revealed the more sensitive portions of the simulated balanced design.

Chapter 4

Matching Network Considerations

This chapter focuses on the importance of matching for LTI receive antennas for maximum SNR and seeks to showcase how optimal matching solutions can change as a function of noise environment. An investigation of this nature that includes a modulated signal analysis in the form of OOK signals has not been shown before in the literature. The literature currently includes investigations in improving the SNR of the receive system through different matching solutions [53] as well as decreasing the noise figure of the receive system [54]. The investigation in [55] briefly mentions bandwidth by pointing out that high-impedance buffer amplifiers achieve larger bandwidths than standard matching networks, but bandwidth is never measured and has no impact on the results. As such there is a lack of investigation on the impact of the matching solution on receiving modulated signals that this work seeks to rectify. Receiving modulated signals serves as a realistic test bed for these electrically small LTI antennas that combines the effects of SNR and bandwidth. The investigation of matching network performance under different noise environments is also a novel contribution which has not been shown in the literature. In addition, important considerations for ensuring adequate power transfer to and from the parametrically tuned receive antenna are highlighted and discussed.

A large portion of this chapter deals with an investigation of different matching techniques for electrically small antennas on receive. This is in order to ensure the LTI antenna against which the time-varying antenna implemented in this work is compared to uses the optimal matching solution. For this investigation, a low-noise amplifier (LNA) was designed specifically for use in simulation in conjunction with a single order L-matching network in addition to a variety of high-impedance buffers as alternative matching solutions. The impacts of these solutions on the noise figure and signal-to-noise ratio of the receive system are investigated. A more in-depth investigation on the impact of different L-matching regimes on the SNR and modulated signal characteristics of the receive system is also completed.

4.1 LNA Design

A low-noise amplifier was designed for use in this investigation. While S-parameters for consumer off-the-shelf (COTS) LNAs are widely available, only the noise figure as a function of frequency is typically given. This noise figure assumes a source and load impedance of 50 Ohm and therefore does not accurately model the effects of different source impedances. Electrically small antennas typically do not present an impedance of 50 Ohm and used matching networks to transform the input impedance to value closer to the standard 50. As a part of this investigation, different matching networks were used resulting in different impedances being presented to the LNA in a source pull manner [56]. By starting with a vendor transistor model in ADS which has accurate noise parameters, the noise characteristics of the amplifier can be correctly represented as a function of both frequency and source impedance. The noise figure of the LNA changing as a function of source impedance is an important characteristic that would not be accurately modeled with only the use of LNA datasheet quantities necessitating the design of the LNA from a transistor model. The noise generated by an amplifier can be completely described by four noise parameters: r_n, the equivalent noise resistance normalized to 50 Ohm, Γ_{opt}, the magnitude and phase of the optimum noise reflection coefficient, and F_{min}, the minimum noise figure of the amplifier when optimally noise matched [57]. To find the noise figure of the amplifier as a function of the source reflection coefficient the equation,

$$F = F_{min} + 4r_n \frac{|\Gamma_s - \Gamma_{opt}|^2}{|1 + \Gamma_{opt}|^2(1 - |\Gamma_s|^2)}, \tag{4.1}$$

is used where Γ_s is the source reflection coefficient presented to the input of the amplifier. As can be seen from the equation, the closer the source reflection coefficient is to the optimum noise reflection coefficient, the smaller the amount of noise seen at the output of the LNA is. There is a minimum noise figure that is achieved when the LNA is perfectly noise matched. This minimum noise figure is largely determined by the transistor(s) used in the LNA design as well as the stability implementation.

The transistor chosen was a Infineon BFP720 SiGe:C NPN heterojunction bipolar transistor [58]. This transistor boasts a minimum noise figure of less than 0.6 dB and a maximum power gain of more than 36 dB at 150 MHz. Due to biasing, stability, and matching constraints this ideal noise figure and maximum gain can not be realized with the simple LNA design utilized here. The maximum gain and minimum noise figure create a trade-off space whereby one can only be optimized at the cost of the other. In addition, more complicated techniques to achieve stability than the ones used here can be applied to improve the noise figure and gain.

4.1.1 Design process

A transistor-based common emitter LNA was designed with the Infineon BFP720 transistor using the ADS amplifier design guide and details found in [59]. To begin the design process of this simple LNA, the biasing conditions for the transistor must be chosen. For this simple design, DC voltage supplies were used to set V_{CE}, the voltage from the collector to the emitter, and to set I_B, the current at the base of the transistor. Using a combination of the transistor datasheet and sweeps in ADS, V_{CE} was chosen to be 3 V and I_B was chosen to be 40 μA. These biasing conditions affect both the minimum noise figure achievable by the LNA as well as the maximum available gain. By increasing the bias voltages and currents, a higher gain can be achieved at the cost of a higher noise figure.

Once the biasing conditions were set, the LNA had to be stabilized. This prevents the LNA from oscillating which would destroy the signal and potentially the rest of the system. When the stability factor,

$$K = \frac{1 + |\Delta|^2 - |S_{11}|^2 - |S_{22}|^2}{2|S_{21}||S_{12}|}, \tag{4.2}$$

is larger than one and when $\Delta = |S_{11}S_{22} - S_{12}S_{21}|$ is less than one, then the amplifier is unconditionally stable [60]. To track the stability of the LNA, the stability factor K and the associated Δ factor were plotted across frequency while resistive stabilization was employed. Resistive stabilization involves the use of additional resistance on the LNA input and/or output to ensure that the reflection coefficients on either side are less than one. Instability can occur when the input or output reflection coefficient of the LNA exceeds unity. A parallel resistance of 40 Ohm was added to the output of the LNA before the DC block in order to increase the stability factor of the LNA to above one for a large range of frequencies as seen in

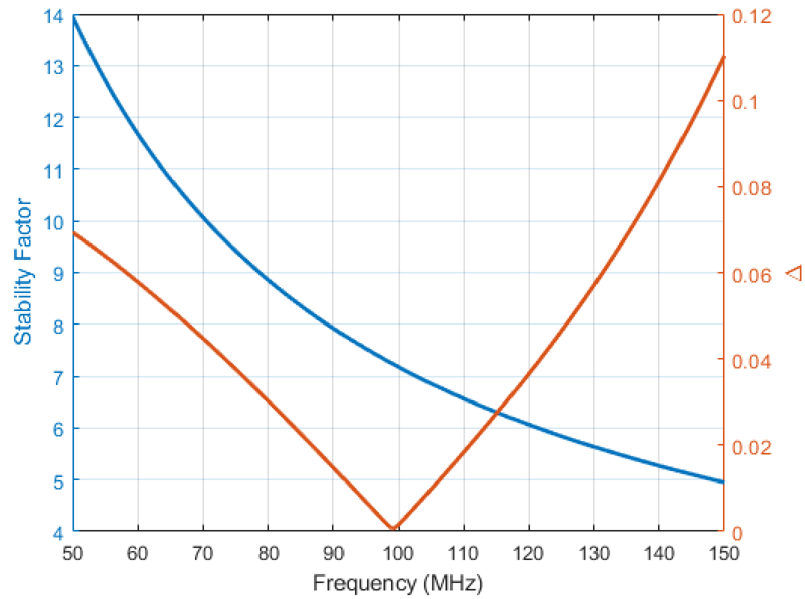

Figure 4.1: Stability factor, K, and Δ factor as a function of frequency for the designed LNA.

Fig. 4.1. For LNAs, resistive loading on the output to achieve stability is preferable to resistive loading on the input as the resistor will invariably add noise. By having the resistor be on the output of the amplifier, the noise generated by said resistor is not further amplified.

With the LNA biased and stable, the input and output matching networks could be designed. The matching networks for the LNA were first designed to match to 50 Ohm to compare to the other typical LNAs and ensure this basic LNA design had comparable performance. The noise figure performance and gain of the LNA when the input and the output is conjugate matched to 50 Ohm and for when the LNA is noise matched can be seen in Fig. 4.2. From the results in Fig. 4.2, we see that this LNA design is indeed comparable to COTS LNAs in both gain and noise figure for the chosen frequencies. The schematic for the LNA set up for a noise match with a 50 Ohm source impedance can be seen in Fig. 4.3.

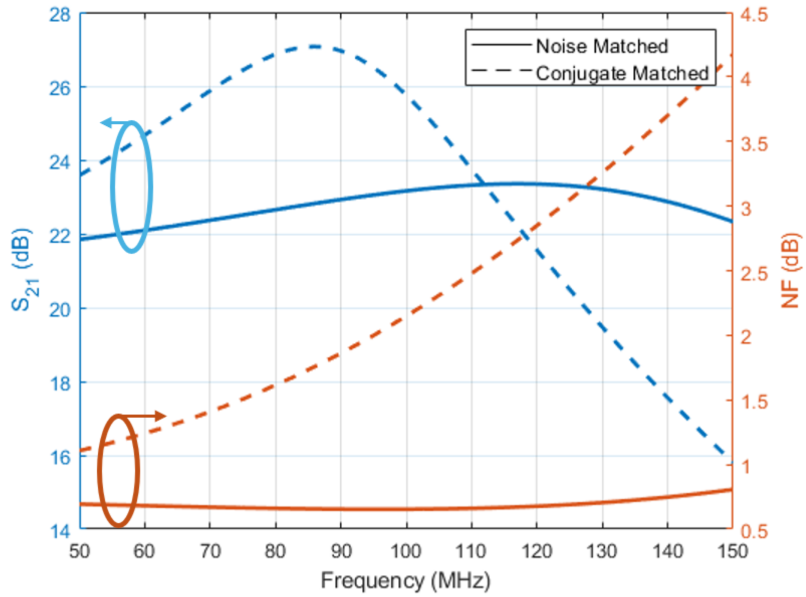

Figure 4.2: Gain and noise figure as a function of frequency for the LNA designed for a 50 Ohm input.

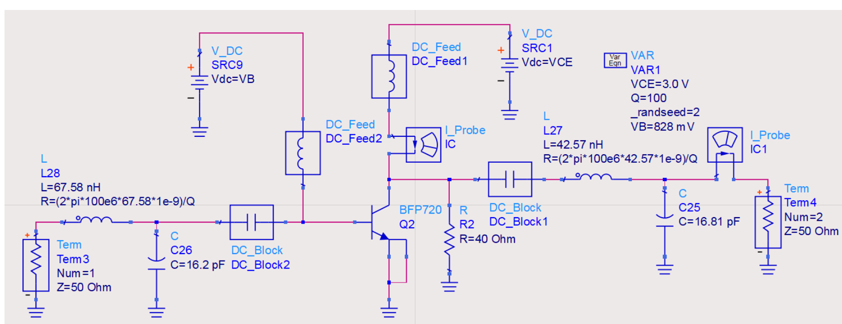

Figure 4.3: Keysight ADS schematic for the common emitter LNA designed for a 50 Ohm input.

4.1.2 Matching to the ESA

The ESA chosen for this analysis is an electrically small square loop antenna with a total footprint of 150 mm by 150 mm which is brought to resonance with a 3.975 pF capacitor. The input impedance of the antenna is approximately 0.65 Ohm which of course varies from the normal amplifier assumption of a 50 Ohm source, but a matching network is necessary anyway to bring a typical 50 Ohm source

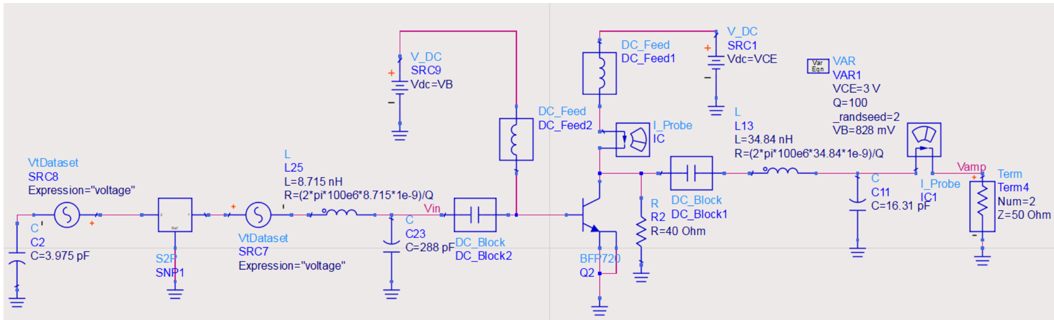

Figure 4.4: Keysight ADS schematic for the common emitter LNA designed for the electrically small loop antenna under investigation. The input matching network shown is for the noise match point of the LNA.

impedance to the conjugate match point of the transistor or to the optimal noise impedance for noise matching. These two matching points, the conjugate match point and the noise match point, are two different impedances that result in either optimal power transfer in the case of the conjugate match point or lowest noise generation from the transistor in the case of the noise match. As such, the typical L-matching network need only to be altered to match the transistor to a 0.65 Ohm source impedance. Matching networks were designed to match the input impedance of the ESA to the optimal noise impedance and the conjugate match point of the amplifier. The ESA connected to the LNA through a matching network designed to noise match the LNA can be seen in Fig. 4.4.

4.2 High Impedance Buffer

High impedance buffers can be very useful for wideband systems at lower frequencies such as HF. They negate the need for a matching network by presenting the antenna with an large impedance, effectively probing the antenna's open circuit voltage which is proportionally to the power in the incident plane wave. This open circuit voltage is then seen on the output of the buffer with no voltage gain but a cur-

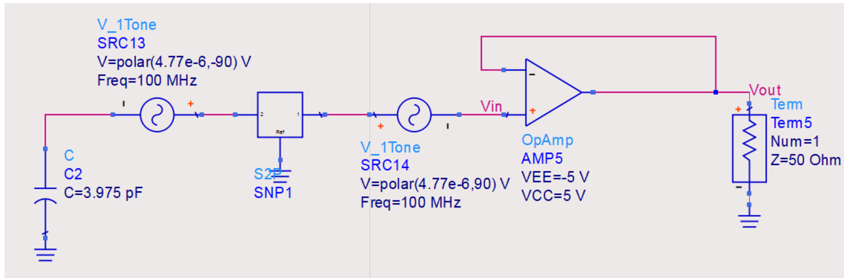

Figure 4.5: Keysight ADS schematic for a simplistic op amp based high impedance buffer.

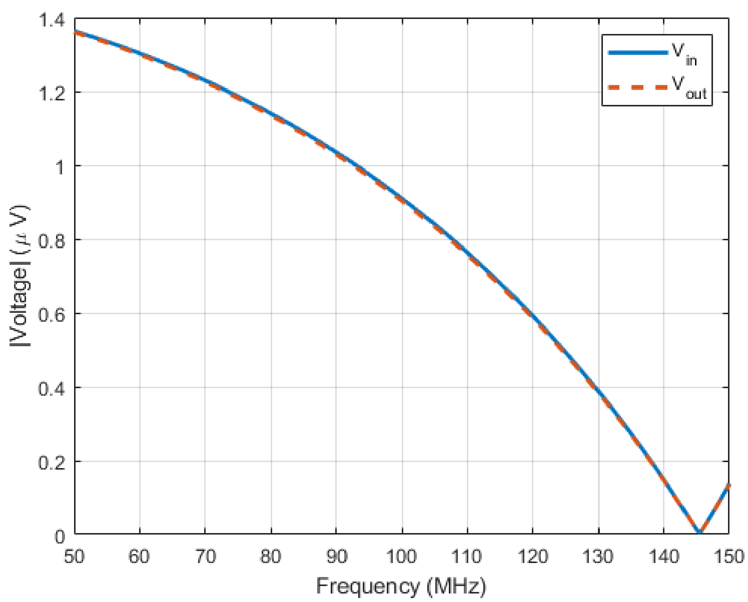

Figure 4.6: Input and output voltages in μV for the simplistic op amp based high impedance buffer. The input voltage was from the electrically small loop antenna which was receiving power from an incident plane wave of 200 μV/m.

rent gain instead. The voltage at the output of the buffer can then easily be further amplified without sacrificing any bandwidth to narrowband matching networks.

4.2.1 Op Amp Buffer Amplifiers

A simplistic op amp based buffer amplifier was designed based on [61] using a TI OPA856 op amp [62]. The schematic of the basic implementation can be seen in Fig. 4.5, with the input and output voltages shown in Fig. 4.6. While there is a tiny loss in voltage, the high impedance buffer does indeed function as intended with a high input impedance and a substantially smaller output impedance. Once the buffer amplifier was functioning correctly, the noise impact of the amplifier was investigated. The source impedance was changed to reflect the input impedance of the previously mentioned electrically small loop antenna which was 0.65 Ohm. The noise figure was then plotted across frequency as shown in Fig. 4.7. The noise figure at 100 MHz of approximately 18.97 dB for the given source impedance is not acceptable, especially considering this buffer amplifier would appear at the beginning of the receive chain and would therefore have a major impact on the system's total noise figure [36]. This high noise figure is due to the source impedance of the electrically small antenna under test being quite small compared to the optimal noise impedance of the amplifier of 600+j1 Ohm. While the high impedance input of the buffer amplifier negates the need for an input matching network for signal preservation, a reasonable source impedance for noise considerations is still necessary. The noise figure of the op amp buffer amplifier can be significantly improved if the source impedance is brought up from the antenna's 0.65 Ohm to a higher impedance of 50 Ohm or 600 Ohm as seen in Fig. 4.8.

A different implementation of an op amp based buffer amplifier, the instrumentation amplifier, was also designed. This buffer amplifier design makes use of three op amps to not only provide a high impedance buffer, but to also amplify the voltage of the incoming signal. This is done using a two-stage method with two of the op amps providing the high impedance input while the final op amp provides the voltage amplification. The two-stage method improves the buffer amplifier's resilience to the source loading down the high input impedance and also allows for easy implementation as a balun solution [61]. The input is differential with

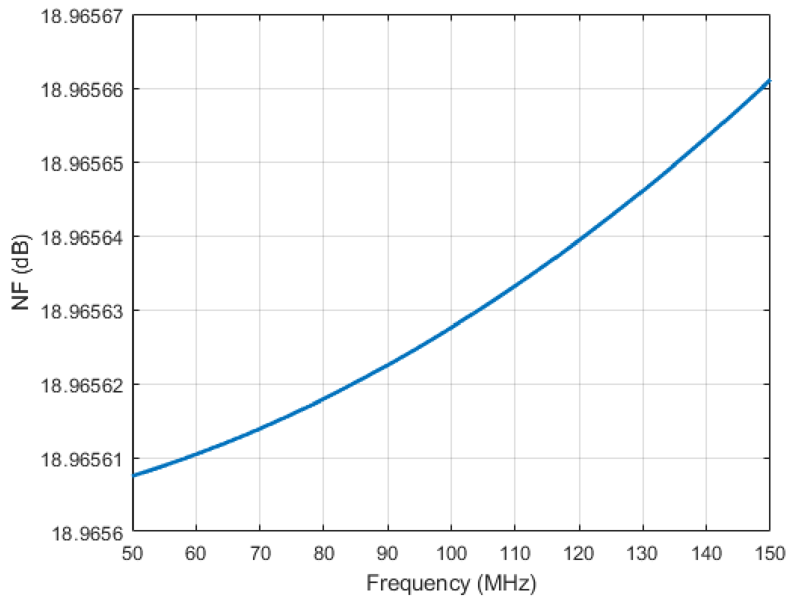

Figure 4.7: Noise figure across frequency for the simplistic op amp based high impedance buffer with the electrically small loop antenna as the input.

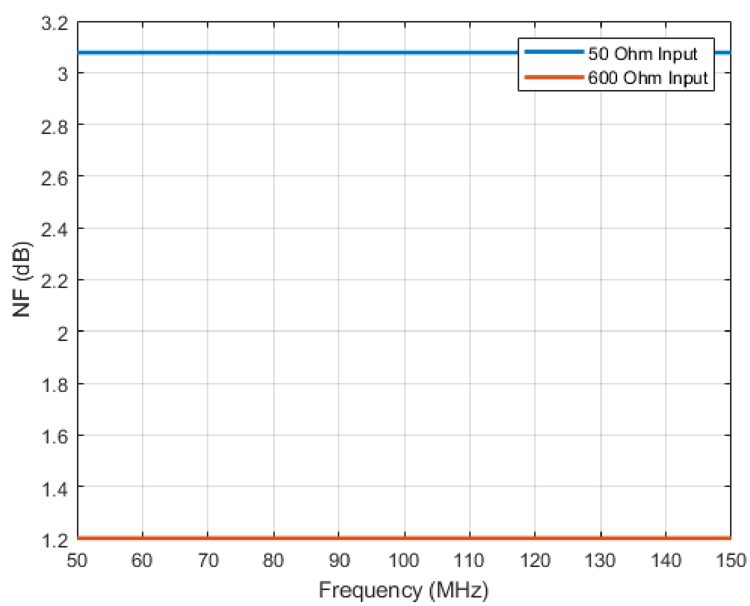

Figure 4.8: Noise figure across frequency for the simplistic op amp based high impedance buffer with different source impedances.

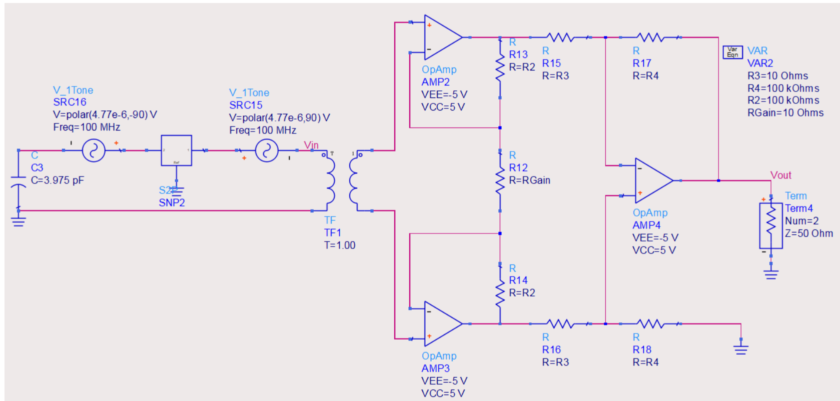

Figure 4.9: Keysight ADS schematic for the instrumentation amplifier with the electrically small loop antenna as the input.

the output being single-ended. The ADS circuit schematic for the instrumentation amplifier is shown in Fig. 4.9 with the resulting gain and noise figure shown in Fig 4.10. While a gain similar to that of the LNA can be achieved, the high noise figure due to the low source impedance makes this a problematic matching and/or balun solution. As with the simple single op amp high impedance buffer, this amplifier has a significantly lower noise figure if the source impedance is increased from 0.65 Ohm.

4.2.2 Transistor Buffer Amplifier

A buffer amplifier based on a transistor was also implemented using the ADS schematic from [63]. This buffer amplifier, seen in Fig. 4.11, is based on a common source MOSFET architecture. The same electrically small loop antenna was connected and the noise figure of the amplifier was investigated once again, shown in Fig. 4.12. While the noise figure shows a marginal improvement over the op amp buffer amplifier, it still remains high relative to many antenna and amplifier combinations. Other configurations using the LNA with this electrically small antenna model can yield noise figures on the order of 5 dB.

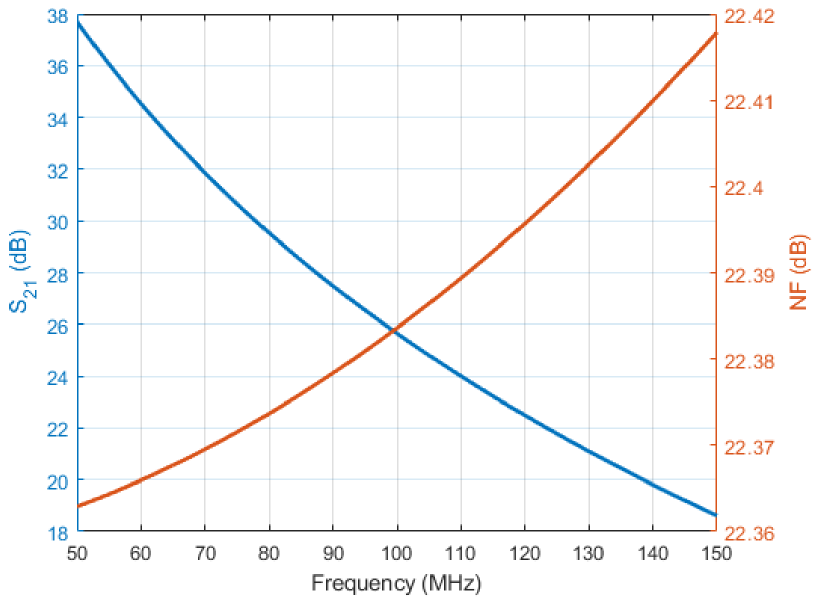

Figure 4.10: Gain and noise figure across frequency for the instrumentation amplifier with the electrically small loop antenna as the input.

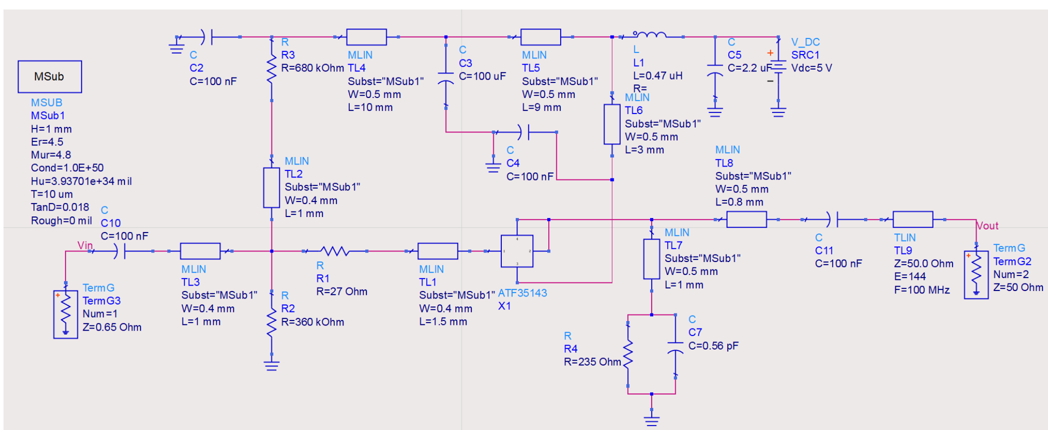

Figure 4.11: Keysight ADS schematic for the common source buffer amplifier with the electrically small loop antenna as the input. This schematic is based on work done in [63].

All of the buffer amplifier designs were abandoned due to high noise figures for this particular electrically small antenna. While the noise figures of these high impedance buffer amplifier designs can be manageable with more typical source impedances such as 50 Ohm, the low input impedance of the electrically small

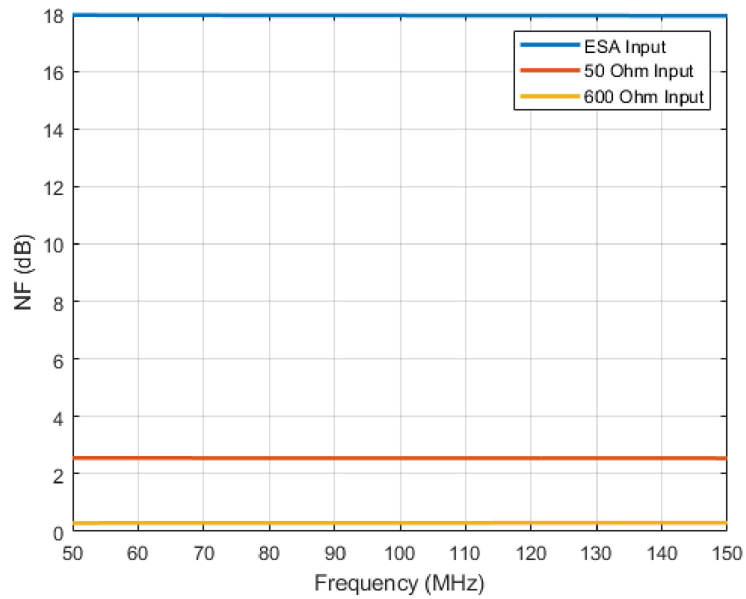

Figure 4.12: Noise figure across frequency for the common source buffer amplifier for different source impedances.

loop antenna is problematic. Other electrically small antennas which have higher impedances, such as meander line antennas [23] can function quite well with these buffer amplifiers [55]. Matching networks can also bring up the impedance of the electrically small loop antenna which improves the noise figure but sacrifices other benefits of the high impedance buffer such as the increased bandwidth.

4.3 L-Matching Network Performance Analysis

An investigation focusing on the optimal matching network strategy between an electrically small antenna, in this case an electrically small loop antenna, and a typical LNA is undertaken. The different strategies investigated here are a conjugate match, where the power delivered from the antenna terminals to the LNA is maximized, a noise match, where the noise produced by the LNA is minimized, as well as matching schemes in between the two that might perform better in different

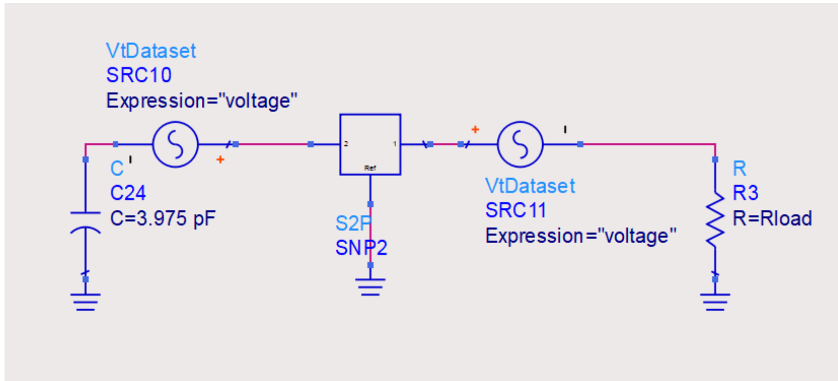

Figure 4.13: Keysight ADS implementation of the electrically small loop antenna. The implementation involves a multiport representation of the antenna with the first port loaded by either a load resistor or the impedance of a connected system and the second port loaded with a 3.975 pF capacitor to bring the antenna to resonance at 100 MHz.

noise environments. The high impedance buffers showcased previously will not be investigated here due to their high noise contribution for this particular electrically small loop antenna. The figures of merit for these cases are the signal-to-noise ratio (SNR) or the error vector magnitude (EVM) for the antenna plus LNA systems with the assumption that the receiver that comes after the LNA has a noise figure of 25 dB. The matching cases were investigated for both a single frequency tone as well as OOK signals with varying data rates.

4.3.1 Simulation Models

In addition to the LNA model and the high impedance buffer models used in ADS in this analysis, the model of the electrically small loop antenna is of importance. The MATLAB signal generation and noise modeling also use the loop model to accurately represent the port voltages of the signal and the external noise. It is of use then to discuss the ESA model used as well as an overview of the MATLAB portions of the analysis.

ESA Model

The ESA model is a multiport model of a square loop with a 150 mm side length and 3 mm wire width. The model is generated using a conversion matrix method of moments (CMMoM) approach that produces an impedance matrix that is then compressed down to only two ports [16]. These two ports are the ports on which a load is placed. For this antenna, the first port is the antenna feed which is connected to either the system in a system analysis or a resistor for pure antenna analysis. The second port is loaded with a 3.975 pF capacitor to bring the loop to resonance at 100 MHz. With the compressed impedance matrix, the open circuit voltage on each of the ports can be calculated as a function of the electric field intensity, polarization, phase, and direction of an incoming incident plane wave. These voltages can then be imported into ADS for use in frequency and time domain simulations. The ADS schematic for the ESA model can be seen in Fig. 4.13. This model is then connected to the input of the LNA via a lossy L-matching network utilizing an inductor with a Q value of 100.

Noise models

The external noise received by the ESA was modeled using the covariance method as described in [64] based on work found in [65]. The impedance matrix of the method of moments (MoM) model of the physical antenna is used in addition to the covariance spectrum matrix of the noise voltage(s) to find the power spectral density of the noise as seen by the antenna. The thermal noise due to the losses in the antenna model as well as the external noise due to the outside RF environment are contained within the external noise power spectral densities used in this analysis. Two different external noise levels were used: a quiet rural noise environment and a business noise environment as defined in ITU Recommendation P372-16 [66]. These noise powers are multiplied by the gain of the LNA to find the noise power seen by the receiver for the frequency domain simulations. For the time domain based analysis, the equivalent noise power was used to generate different iterations of random noise that were added to the received signal in ADS.

The internal receiver noise was implemented based on a 25 dB noise figure receiver located after the LNA. This corresponds to an equivalent noise temperature of 91416 K which, when combined with the Boltzmann constant and the receiver bandwidth, allows for the noise power contributed by the receiver to be calculated simply. As with the external noise, this noise power could be used directly in the frequency domain or used to generate random noise iterations in the time domain. The internal noise generated by the lossy matching networks and by the LNA itself was modelled in ADS using a noise bandwidth equal to the bandwidth of the signal used for testing.

4.3.2 Single Frequency Tone Signal

The first portion of the investigation focused on the effects of different matching techniques on the spectral SNR of a single frequency signal at 100 MHz. An ADS schematic was setup for an AC simulation as shown in Fig. 4.14. The L-matching network between the antenna model and the LNA was varied such that the impedance looking from the input of the LNA towards the antenna covered a representative portion of the Smith Chart. In other words, the source impedance seen by the LNA was varied by adjusting the L-matching network with the 23000 test points plotted on the Smith chart in Fig. 4.15. These many thousands of L-matching network parameters were generated using code from Kurt Schab and then

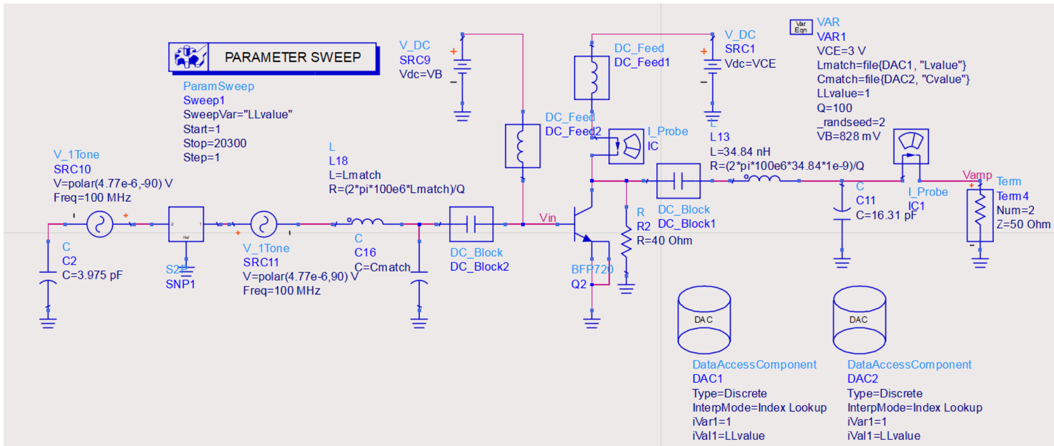

Figure 4.14: Keysight ADS schematic for the single frequency tone matching analysis. A total of 23000 different L-matching networks were calculated in MATLAB and the resulting inductor and capacitor values were imported into the schematic using Data Access Components and swept across.

modified into a form that could be imported into ADS [67]. This simulation was carried out in the frequency domain which is why so many different matching network values could be tested fairly quickly. The Data Access Components in ADS allowed for the necessary matching networks to be calculated in MATLAB and then imported for use in sweeping simulations.

A 200 μV/m plane wave at 100 MHz impinging onto the electrically small loop antenna resulted in voltages on the two compressed ports on the antenna model which were calculated using the antenna's compressed impedance matrix. The plane wave was modelled as impacting the antenna in between the capacitor and feed of the antenna resulting in voltages on the two ports that were equal in magnitude and $180°$ out of phase. The output signal and noise voltages of the schematic were taken at the 50 Ohm termination after the LNA.

The spectral SNR in dB for the different source impedances caused by altering the matching network is shown in Fig. 4.16 for a quiet rural external noise environment and in Fig. 4.17 for a business noise environment. Highlighted in each figure

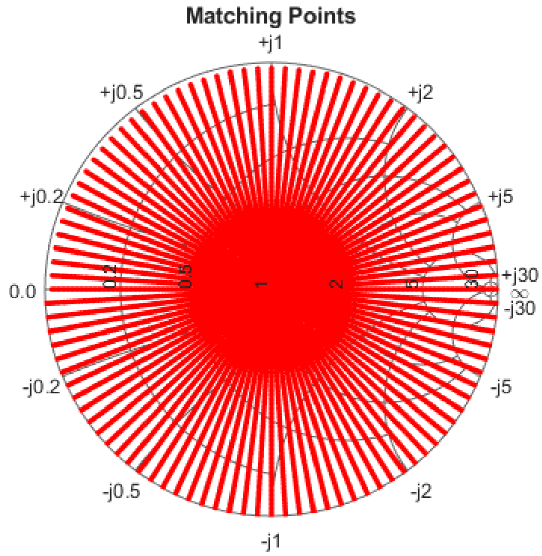

Figure 4.15: Source impedances seen by the LNA for the 23000 different L-matching network realizations utilized in the single frequency tone analysis. A fairly high inductor Q value of 100 used in the matching networks resulted in a good spread of impedances across the Smith chart.

is the conjugate match point to maximize the gain of the LNA, the noise match point to minimize the noise generated by the LNA, and the point of highest spectral SNR seen at the receiver after the LNA. The optimal matching point between the quiet rural and business cases does not seem to move much, however, in the business case the optimal matching point becomes a little more forgiving. The spectral SNR falloff is slower as the match point varies from the optimal SNR point in the business case.

To further clarify what happens to the optimal matching point under different noise environments, the analysis can also be expanded to look at more extreme cases. The spectral SNR results for a case where the external noise is made artificially high can be seen in Fig. 4.18. For this extreme case, the spectral SNR for all matching points is functionally the same. The external noise is so much higher than

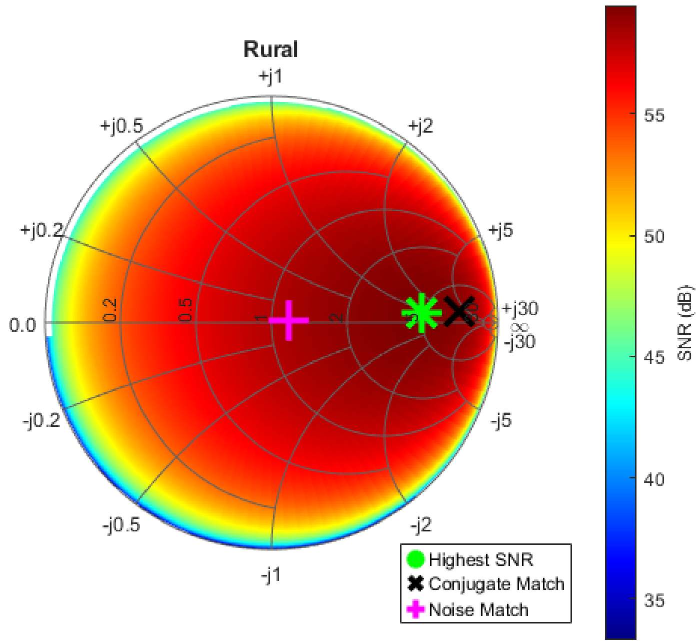

Figure 4.16: Spectral SNR as a function of the source impedance seen by the LNA for a quiet rural external noise environment.

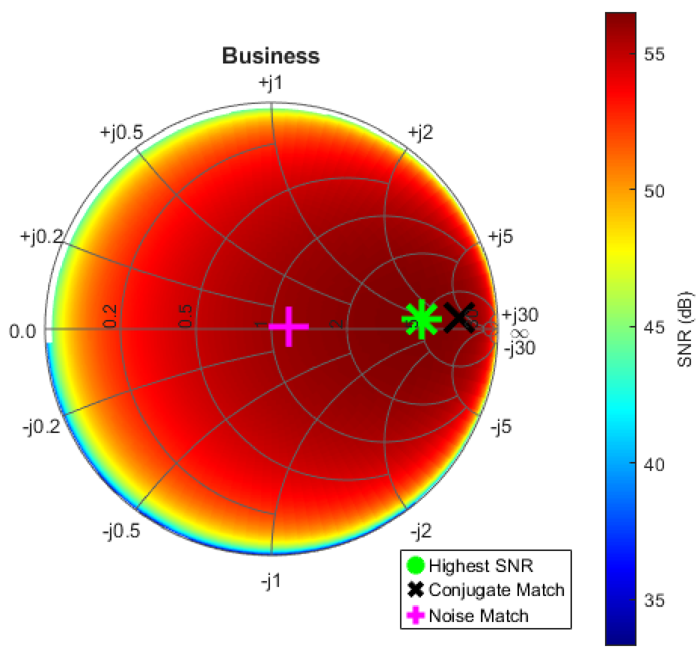

Figure 4.17: Spectral SNR as a function of the source impedance seen by the LNA for a business external noise environment.

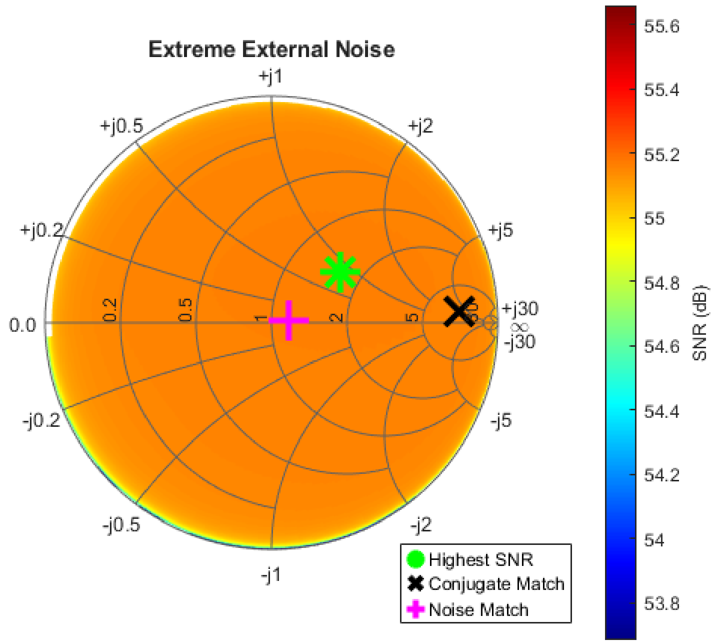

Figure 4.18: Spectral SNR as a function of the source impedance seen by the LNA for an extremely externally noise-limited system.

any internal noise that matching is no longer important and the SNR upper bound of the system, the external SNR, is always reached regardless of matching.

(Change scale to 54.6) The reverse case where the external noise is made artificially lower is also investigated for two different internal noise cases. If the receiver is made noiseless such that any internal noise that is generated comes from LNA itself and the external noise is very low, the spectral SNR results in Fig. 4.19 are achieved. We see when the primary source of noise is the LNA itself, the optimal matching point is the noise match of the LNA. This makes sense as the noise match point seeks to minimize the noise generated by the LNA. The other case is when the noise generated by the receiver dominates over the external noise and the noise generated by the LNA. The results of that case can be seen in Fig. 4.20. Here we see that conjugate matching is the optimal matching case. This is because with the high receiver noise, the optimal spectral SNR is achieved when the received signal

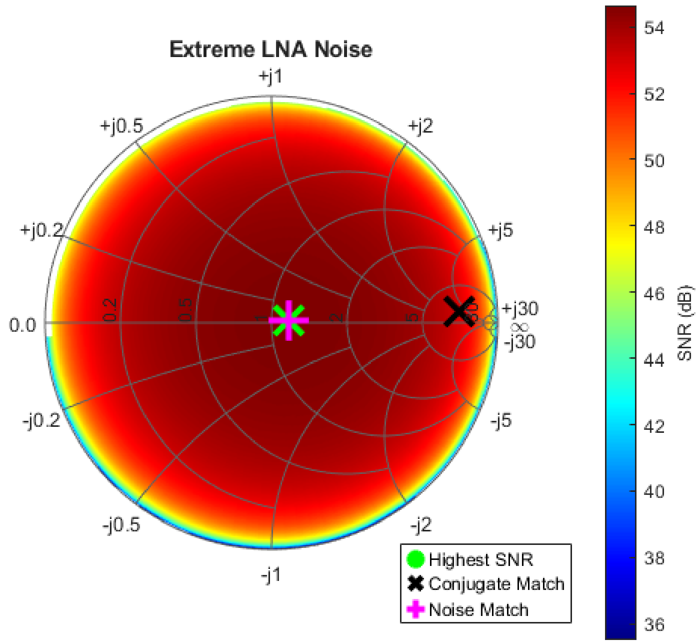

Figure 4.19: Spectral SNR as a function of the source impedance seen by the LNA for an extremely internally noise-limited system with the LNA as the primary source of internal noise.

is as powerful as possible which is true for the conjugate match.

This phenomenon can be explained in a more intuitive way if the spectral SNR is examined at different points in the system. The first spectral SNR of value in this discussion is the external spectral SNR. This is defined here as the spectral SNR seen at the aperture of the antenna before any antenna or mismatch losses. This is the highest the spectral SNR could ever be in the system as all other components in the receive chain, including losses from the antenna itself, will deteriorate the spectral SNR in accordance with their noise figure. This spectral SNR takes into account the power in the received signal as well as the external noise from the surrounding environment. The signal power and external noise power, in addition to the thermal noise power due to the losses in the antenna and the noise generated from the LNA, are then amplified by the LNA. Finally, the noise power from the receiver is added resulting in the total system spectral SNR.

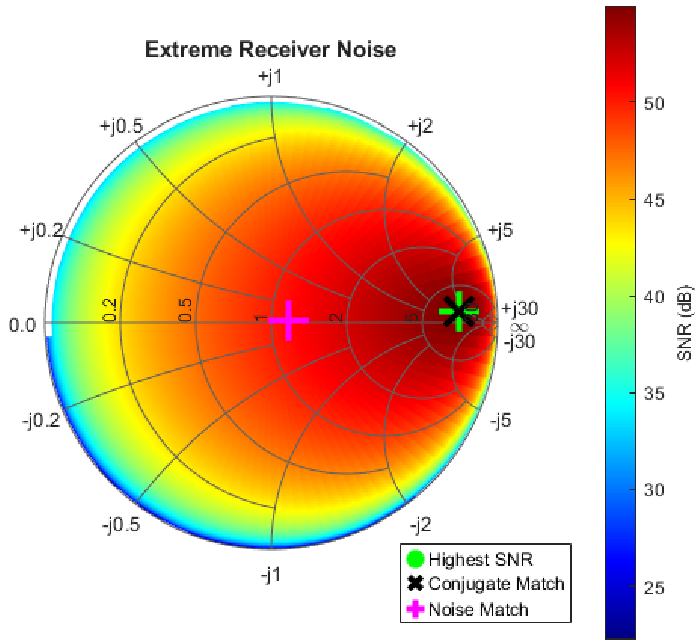

Figure 4.20: Spectral SNR as a function of the source impedance seen by the LNA for an extremely internally noise-limited system with the receiver as the primary source of internal noise.

If the external noise after amplification is significantly higher than the total internal noise, thereby making the system externally noise-limited, then matching is not important to the system spectral SNR. Changing the gain of the LNA in this case does not change the system spectral SNR as the received signal and the external noise are both amplified by the same amount. Therefore, manipulating the matching network to achieve more gain or to achieve less noise generated by the LNA is not important.

If the noise generated by the LNA dominates the system, then minimizing that noise is optimal. Noise matching is the fairly straightforward solution here as it minimizes the noise generated by the LNA by sacrificing some gain. If the internal noise generated by the receiver is significantly higher than the external noise seen at the receiver and the noise generated by the LNA, making the system internally noise-limited and dominated by receiver noise, then maximizing the gain of the LNA through conjugate matching is optimal. Since the internal noise is significantly higher than the external noise, the total system spectral SNR will be heavily degraded compared to the external spectral SNR upper bound. In order to minimize the degradation of the spectral SNR due to internal noise, the gain of the LNA is maximized. This provides as much amplification as possible to the received signal and external noise such that they can be made as powerful as possible compared to the internal noise power. The higher the gain of the LNA, the closer the total system spectral SNR can be to the external spectral SNR.

4.3.3 OOK Signal

For the case where the signal is modulated using on-off keying (OOK), the same analysis is done as in the previous section. However, this analysis is significantly slower and more complex due to the use of time domain analysis. The ADS schematic used for the time domain analysis is shown in Fig. 4.4 with the main difference between the frequency domain schematic and time domain schematic being the port voltage sources on the antenna model. In the time domain, arbitrary time domain voltage sources are used in order to implement the OOK signals which were generated in MATLAB. The resulting output voltages from ADS were demodulated and downconverted to baseband and then processed in MATLAB using an adaptive least mean square equalizer with 128 taps and a step size of 0.01. The figures of merit for these OOK cases are the SNR and the EVM of the demodulated baseband signals. For information carrying signals, EVM measures the normalized distance in the I-Q plane between where the received symbol was measured and where the corresponding ideal symbol should have been. Both noise and distortion in the receive system can adversely affect the received signal and therefore the

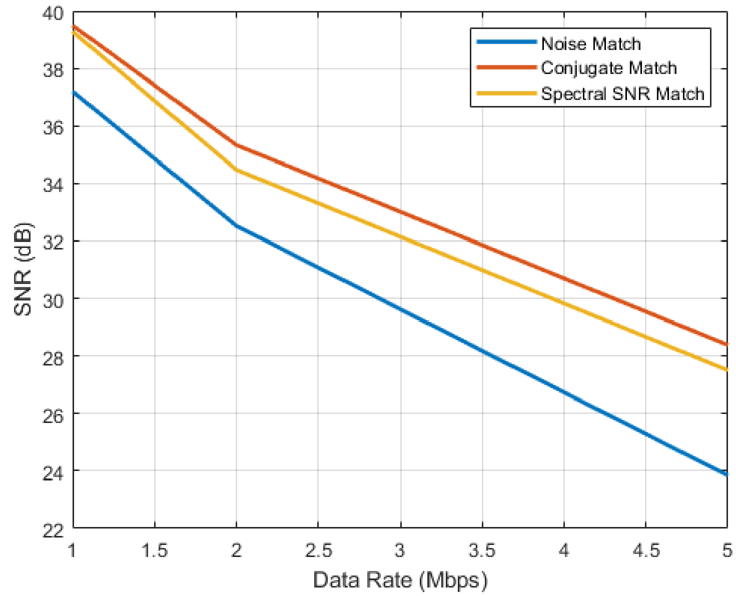

Figure 4.21: SNR for the different matching cases across data rate for a quiet rural external noise environment. The bandwidth used for the SNR calculation is equivalent to the data rate.

measured EVM. The matching cases studied here are the same conjugate match and noise match points as in the previous analysis as well as the matching network that produced the highest SNR in the rural and business external noise cases from the previous study.

The same two primary cases were studied as in the single frequency tone analysis. The quiet rural and business external noise environments were used alongside a 25 dB noise figure receiver with a lower power incident signal plane wave of 50 μV/m. The SNR results for the three different OOK data rates in the two different external noise environments are shown in Fig. 4.21 for the quiet rural environment and Fig. 4.22 for the business noise environment. The associated EVM results for the cases are shown in Fig. 4.23 and Fig. 4.24.

The results show a new aspect of signal fidelity as a function of input matching network that was not seen in the single frequency tone analysis: the effects of dis-

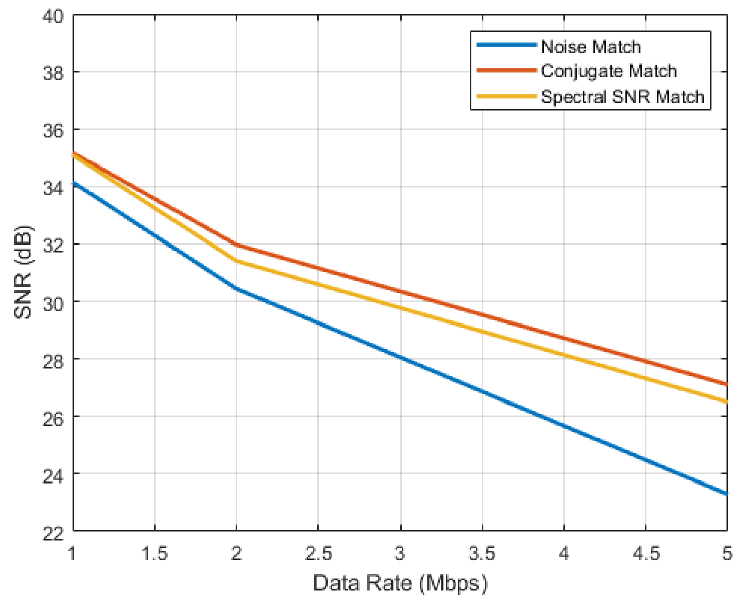

Figure 4.22: SNR for the different matching cases across data rate for a business external noise environment. The bandwidth used for the SNR calculation is equivalent to the data rate.

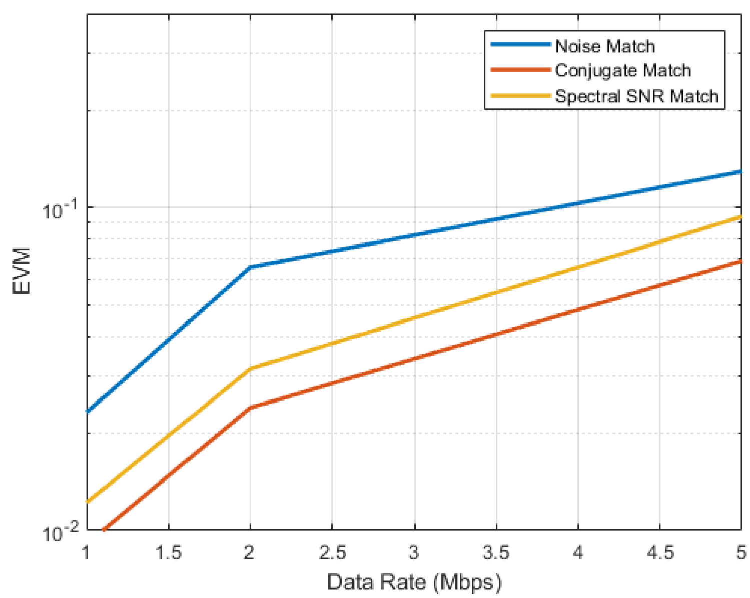

Figure 4.23: EVM for the different matching cases across data rate for a quiet rural external noise environment.

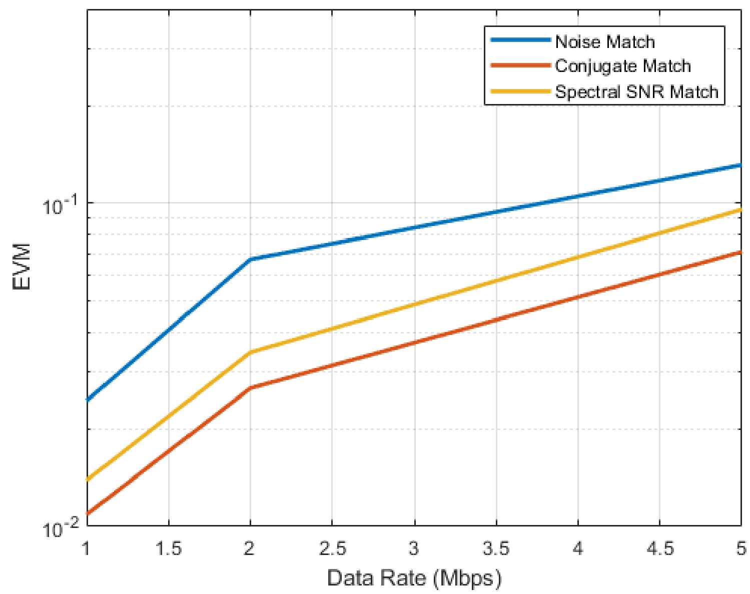

Figure 4.24: EVM for the different matching cases across data rate for a business external noise environment.

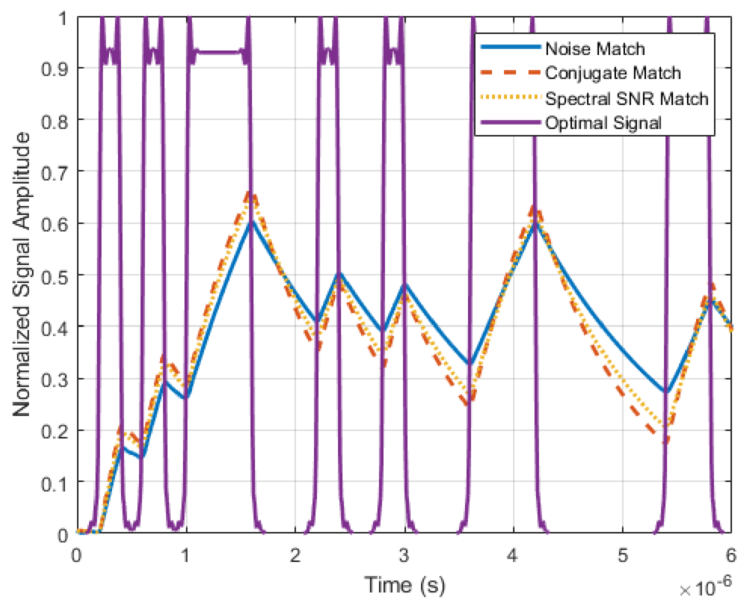

Figure 4.25: Normalized signal amplitude of the different matching cases for a 5 Mbps OOK signal downconverted to baseband.

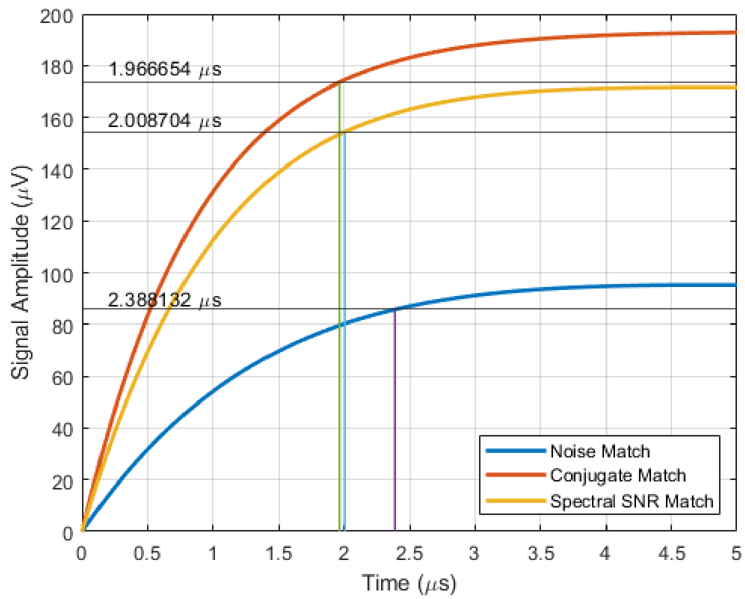

Figure 4.26: Rise times for the different matching cases for a 100 MHz single frequency tone with responses downconverted to baseband. The time taken for each signal to reach 90% of its maximum is shown for each matching case.

tortion. A much clearer impact of the input matching network on the distortion of the OOK signal can be seen in Fig. 4.25 where the 5 Mbps OOK case is plotted. The signal amplitudes of the different matching cases are normalized with respect to their own maximum amplitudes. The general trend seen is that the conjugate and SNR match cases are better able to follow the optimal signal while the noise match case has rise and fall times that cause it to lag further behind. This points to the conjugate match and SNR match cases having better bandwidth characteristics compared to the noise match case even if they all perform poorly due to the high data rate showcased in this specific example. The time domain rise times of the different matching cases for a single frequency tone can be seen in Fig. 4.26 where the conjugate match and SNR match cases have quicker rise times than the noise match case. The rise time for the wideband instrumentation amplifier that was showcased in Fig. 4.9 can be seen in Fig. 4.27 for comparison to the match-

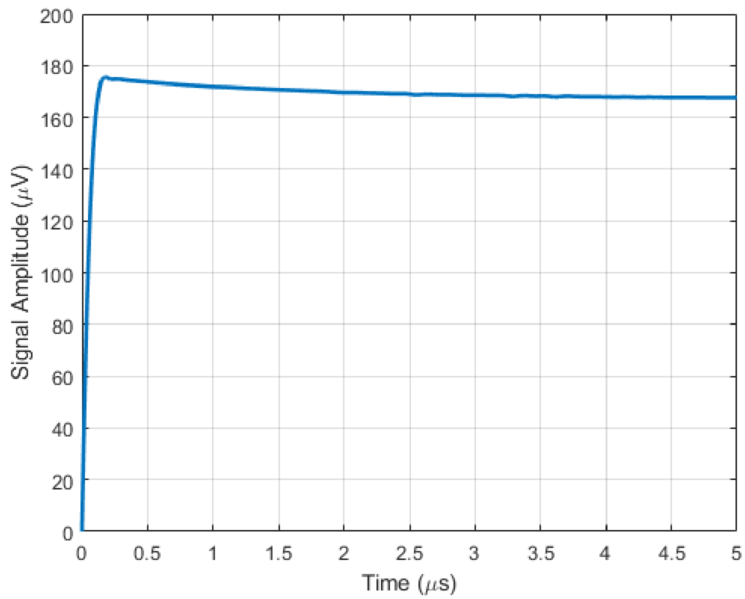

Figure 4.27: Rise time for the instrumentation amplifier for a 100 MHz single frequency tone with the response downconverted to baseband.

ing network implementations. This decrease in rise time pointing to an increased bandwidth is further corroborated by plotting the received power of the system for a 50 μV/m incident plane wave across frequency as shown in Fig. 4.28. The conjugate matched case clearly has the largest bandwidth and the noise matched case has the smallest bandwidth.

The extreme cases analyzed in the single frequency tone case were also investigated for the OOK signal matching cases. The SNR and EVM results for the extremely externally noise-limited case are shown in Fig. 4.29 and Fig. 4.30, respectively. As with the single frequency analysis, in cases where the external noise dominates over any internal noise, matching is unimportant for pure SNR. However, due to causing lower distortion in the OOK signal, the conjugate match and SNR match cases are superior compared to the noise match case for higher signal fidelity and lower EVM.

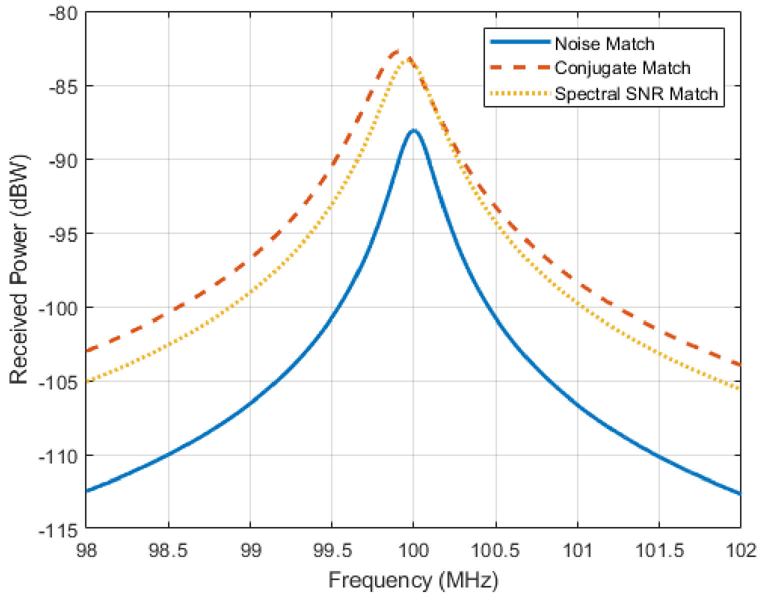

Figure 4.28: Power received by the LNA system across frequency for different matching cases for a 50 μV/m incident plane wave.

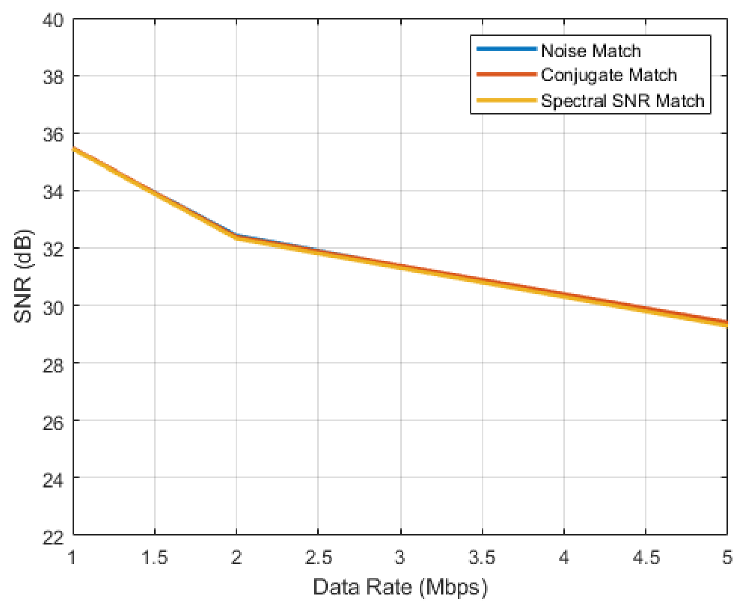

Figure 4.29: SNR for the different matching cases across data rate for an extremely externally noise-limited receive system. The bandwidth used for the SNR calculation is equivalent to the data rate.

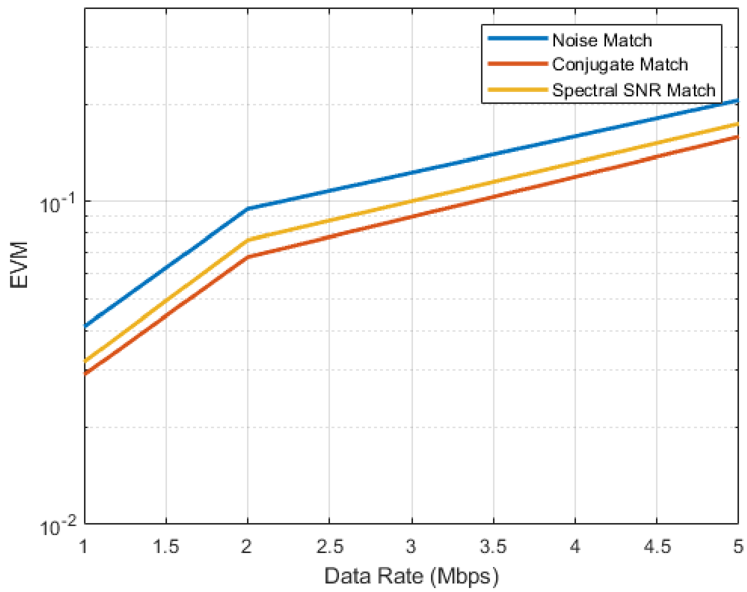

Figure 4.30: EVM for the different matching cases across data rate for an extremely externally noise-limited receive system.

When the system is internally noise-limited due to noise generated by the LNA, the SNR for the different matching cases follow the trend seen in Fig. 4.31 with the EVM trend seen in Fig. 4.32. Again, the SNR follows a similar trend to that seen in the single frequency tone analysis albeit with a smaller difference in SNR between the cases. The EVM, however, tells a different story once more due to the decreased distortion seen in the signal from the conjugate and SNR match points. While the noise match case boasts the highest SNR, it does not show a clear improvement in EVM over the other two cases even in this most ideal of noise match cases.

Finally, when the system is internally noise-limited and dominated by noise from the receiver, the SNR results in Fig. 4.33 are seen along with the corresponding EVM results seen in Fig. 4.34. The conjugate match case is clearly superior here in terms of both SNR and EVM. This is due to the conjugate match's higher SNR in this noise environment as well as the increased bandwidth minimizing distortion.

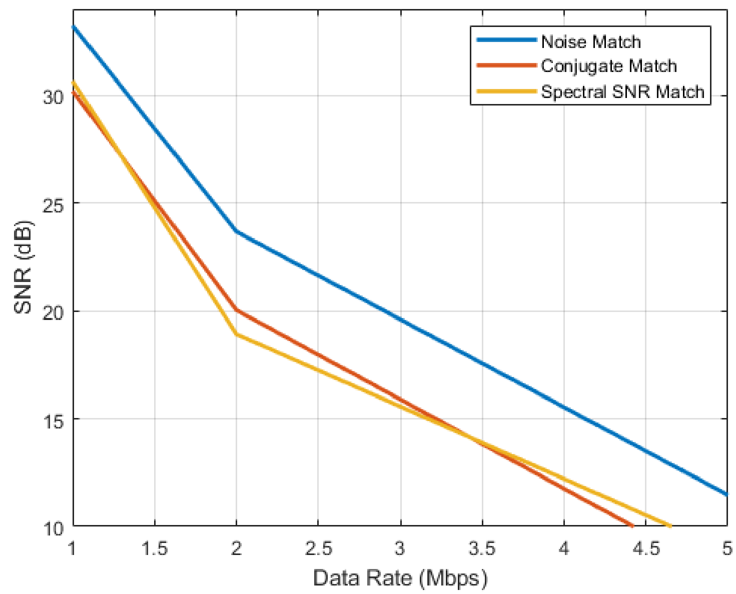

Figure 4.31: SNR for the different matching cases across data rate for an extremely internally noise-limited receive system with the LNA as the primary source of internal noise. The bandwidth used for the SNR calculation is equivalent to the data rate.

4.4 Parametrically-tuned Antenna Matching

The matching network of the parametrically-tuned receive antenna has a large impact on performance and stability as it sets the load impedance seen by the parametric amplifier implemented on aperture. The signal side matching network can be modified to increase the receive effective aperture at the cost of bandwidth or vice versa.

4.4.1 Parametric Amplifier Stability

Parametric amplifiers, like all amplifiers, must be kept stable to avoid oscillation and/or damage. Maximum gain of the parametric amplifier is achieved close to the instability point, but generally operating close to the instability point is avoided to

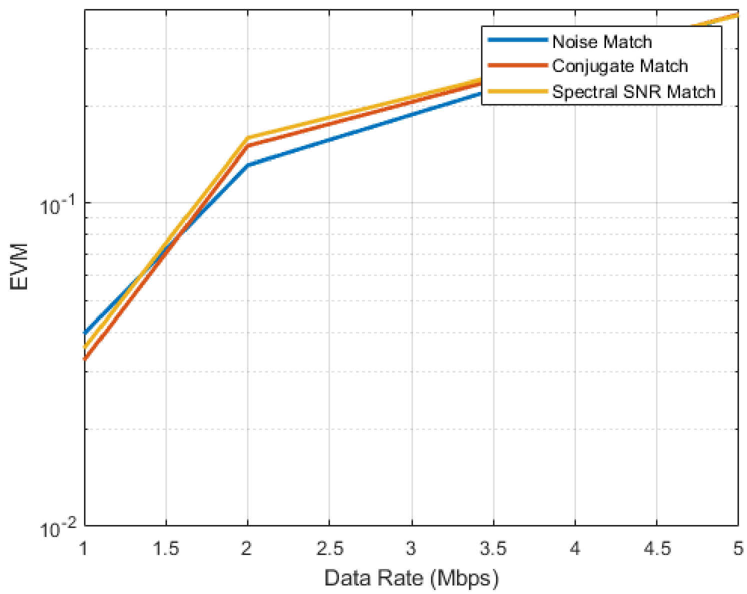

Figure 4.32: EVM for the different matching cases across data rate for an extremely internally noise-limited receive system with the LNA as the primary source of internal noise.

prevent sudden instability while operating. This is even more important when the parametric amplifier is incorporated into an antenna as changes in the environment can lead to changes in antenna impedance which can result in instability. Parametric amplifiers rely on local negative resistance for amplification, but to remain stable the signal branch of the parametric amplifier must have a positive resistance and thus must be loaded with some positive resistance to cancel out the negative resistance. Generally the more positive resistance that loads the antenna, the more stable the parametric receiver is. Stability of the general parametric amplifier discussed in more depth in Sec. 2.1.1 and [13].

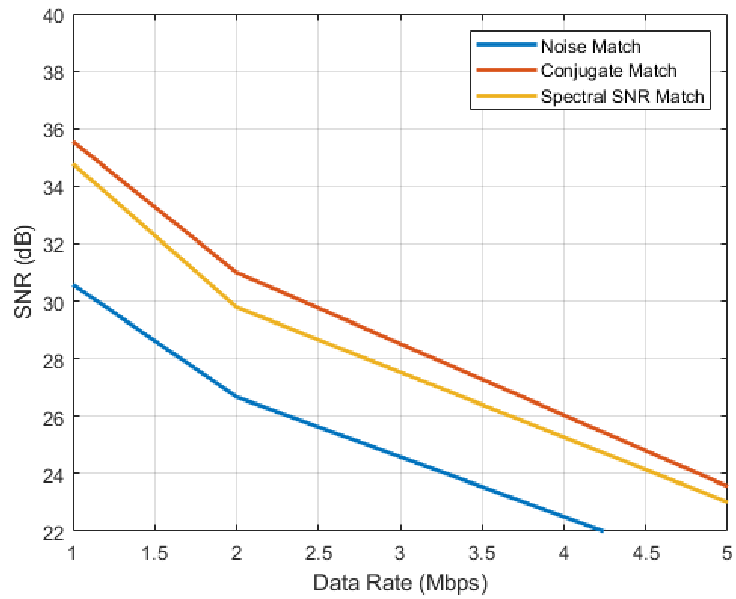

Figure 4.33: SNR for the different matching cases across data rate for an extremely internally noise-limited receive system with the receiver as the primary source of internal noise. The bandwidth used for the SNR calculation is equivalent to the data rate.

4.4.2 Optimizing Matching for the Parametrically-tuned Prototype Antenna

For this work, a single-ended L-matching network was designed to match the 50 Ohm receive system to the optimal load impedance for the parametrically-tuned antenna. This single-ended matching network was then transformed into a differential matching network according to [68] such that it could actually be implemented into the realistic antenna design which itself is differential. The optimal loading impedance was found using a load resistor on the receive port of the design in ADS and sweeping the load resistance. The various load resistances provide a range of received power values as seen in Fig. 4.35 with larger received power values representing larger realized amplification of the design. Taking cues from parametric

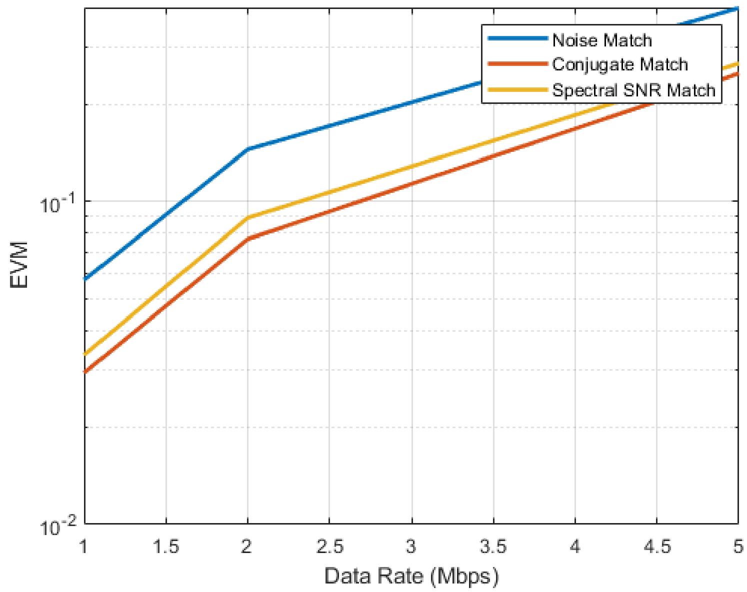

Figure 4.34: EVM for the different matching cases across data rate for an extremely internally noise-limited receive system with the receiver as the primary source of internal noise.

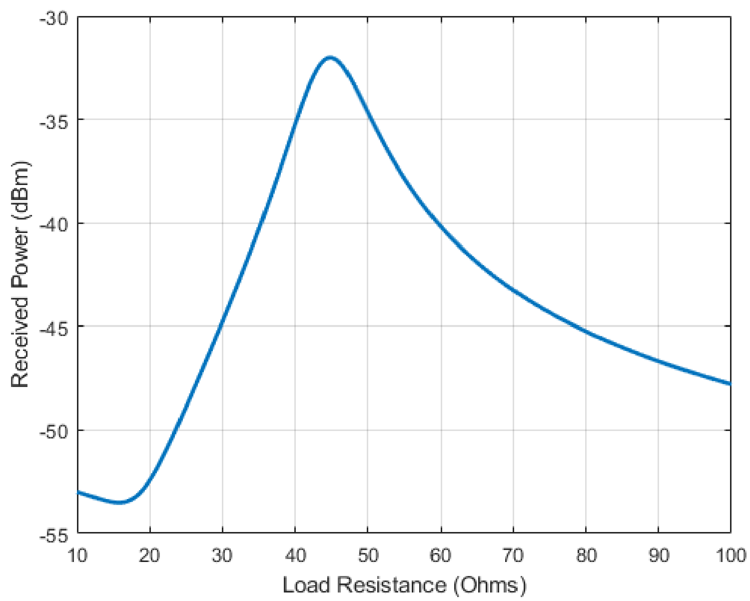

Figure 4.35: Received power at the load of the parametrically-tuned receive antenna in the ADS simulation as the load resistance is swept.

amplifier literature, the larger load resistances on the right side the peak of Fig. 4.35 were investigated using harmonic balance as well as transient simulations to ensure stability. The values to the left of the peak are known to be unstable as the load resistance is less than the negative resistance [13]. The differential matching network was design to match to 59 Ohm, resulting in peak received power from the parametrically-tuned receiver that matched that of the LTI antenna simulation. The resulting differential matching network can be seen implemented in ADS in Fig. 4.36. A highpass matching network configuration with series capacitors and a shunt inductor was chosen specifically to present the chosen load resistance at the signal frequency, while not presenting a large impedance at the idler frequency. A large resistance at the idler frequency would negatively impact the amplification of the parametrically-tuned receive antenna [33].

The load resistance seen by the antenna from the differential matching network can be tuned by adjusting the inductor value in the differential matching network. This tuning approach is leveraged in the fabricated prototype of the parametrically-tuned receiver by substituting different inductors in the matching network to match the peak realized effective aperture to that of the fabricated LTI antenna. The load resistance provided to the antenna via the matching network is also adjusted in simulation to investigate the trade-off between receive effective aperture and bandwidth in Ch. 8.

4.5 Conclusions

An investigation into different matching schemes for an electrically small LTI receive antenna has been completed. The optimal matching solution is heavily dependent on the noise environment in which the receive antenna and receive system

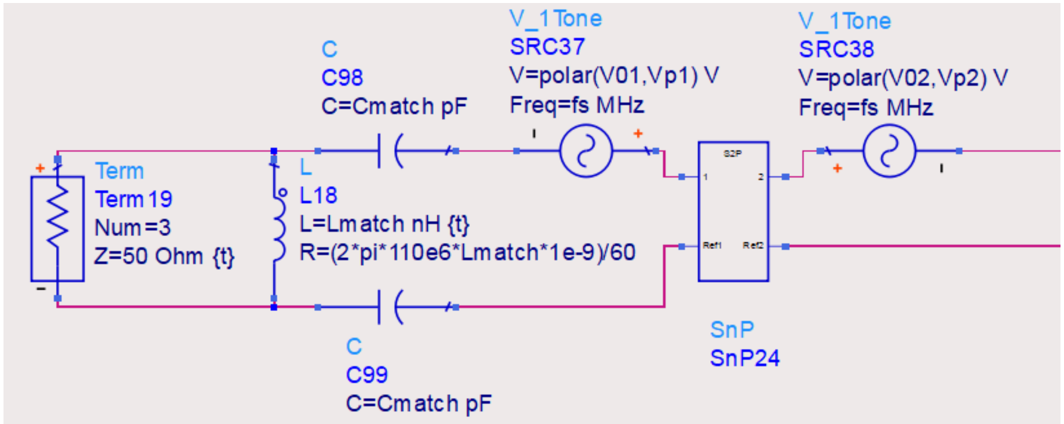

Figure 4.36: Differential matching network for the parametrically-tuned receive antenna in a highpass configuration.

operate. Conjugate matching of the antenna to the rest of the receive system leads to the optimal spectral SNR when the receive system is internally noise-limited from a source other than the LNA, while noise matching the antenna to the LNA is optimal when the LNA is the dominate source of noise. When the system is dominated by external noise, the matching scheme makes little impact on the spectral SNR. Additionally when bandwidth is taken into consideration through the use of modulated signals, conjugate matching appears to produce the optimal SNR in most realistic noise environments. Therefore conjugate matching is used for the concentric loop LTI antenna used later in this work.

Finally, matching in the parametrically-tuned receive antenna is discussed for both the signal portion and the pump portion of the design. Presenting different load impedances to the time-varying antenna results in different peak realized effective apertures and different bandwidths allowing for some trade-offs in the performance of the antenna. The matching for the pump portion of the design, in contrast, is focused purely on maximizing the voltage swing across the varactors from the pump source to help minimize the required pump power for the desired effective aperture.

Chapter 5

Received and Emitted Power Characterization

For this work, the receive parameters of the antennas under test is of great importance as the parametrically-tuned antenna is designed strictly for receive applications. The characterization of the parametrically-tuned receive antenna as well as the comparison LTI antenna on receive is outlined below. In addition, the emissions of the time-varying antenna is investigated to characterize how much power is emitted from the antenna during operation due to the pump source.

5.1 Received Power Measurements

A key parameter to characterize for receive antennas is the ability to capture power from signals incident on said antenna. Though most LTI antennas have this ability measured in gain even on receive, the true receive parameter of interest is the effective aperture of the antenna. The effective aperture is a measure of the antenna's ability to capture power incident upon it and can be characterized for an LTI antenna by

$$A_{eff} = \frac{P_r 4\pi d^2}{P_t G_t}, \tag{5.1}$$

where P_r is the power receive at the terminals of the antenna under test, d is the distance between the transmit antenna and the antenna under test, P_t is the power at the terminals of the transmit antenna, and G_t is the gain of the transmit antenna [42]. An assumption built into Eqn. 5.1 is that the transmitted signal and the signal measured on receive occur at the same frequency. For standard LTI antennas this is a valid assumption, but time-varying antennas–and non-LTI antennas in general–will generate harmonics and intermodulation products at frequencies that are not just at the transmitted signal frequency. This means on receive, incoming signals at these harmonics and intermodulation products can affect the behavior of the antenna at the signal frequency [25]. As such, a more general effective aperture known as cross-frequency effective aperture is needed to describe these cross-frequency coupling effects [25], [42].

For the measurements in this work, cross-frequency effective aperture is used for both the LTI and non-LTI antennas and compared against each other. The LTI antenna has cross-frequency effective aperture equal to zero everywhere but the zeroth harmonic–the signal frequency of interest. The time-varying prototype antenna, on the other hand, receives power at the signal frequency and generates harmonics as the signal interacts with power present at the pump frequency. This means that cross-frequency coupling occurs and must be analyzed to correctly capture the full response of the non-LTI antenna. Measurement of the cross-frequency effective aperture is defined in [42] as

$$A_{eff}(f_{tx}, f_{rx}) = \frac{P_r(f_{rx})4\pi d^2}{P_t(f_{tx})G_t(f_{tx})}, \tag{5.2}$$

where the parameters are similar to those defined earlier, but with the added definition of what frequencies they are based on. The power received, $P_r(f_{rx})$, is reliant on the frequency being measured on receive, f_{rx} and not on the transmit frequency, f_{tx}. An example of the received power seen at the RTSA for the non-LTI antenna

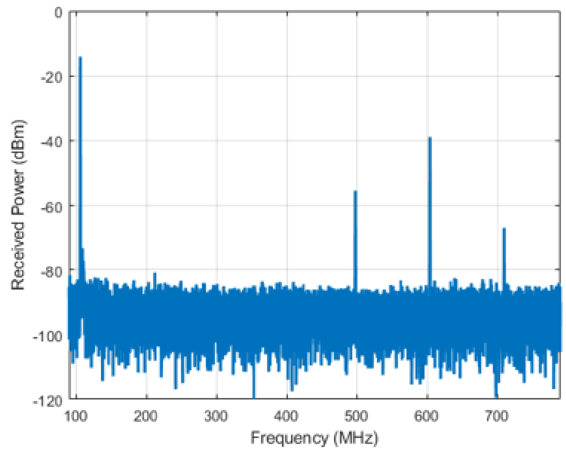

Figure 5.1: Power received at the RTSA from the parametrically-tuned receive antenna across frequency for a single transmitted frequency.

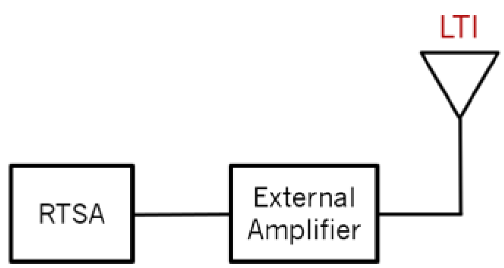

Figure 5.2: Receive side block diagram for the cross-frequency effective aperture measurement for the LTI comparison antenna.

can be seen in Fig. 5.1, where the signal at 108 MHz is clearly seen along with pump power at 605 MHz and the harmonics at 497 MHz and 714 MHz. It should be noted that in the parametrically-tuned antenna's case, there is a filter after the antenna aperture that serves to further attenuate the pump power leaking into the receive chain causing the pump power to look artificially lower at the RTSA. This filter is used for all subsequent testing of the time-varying antenna to ensure that high pump power does not degrade the sensitivity of the RTSA.

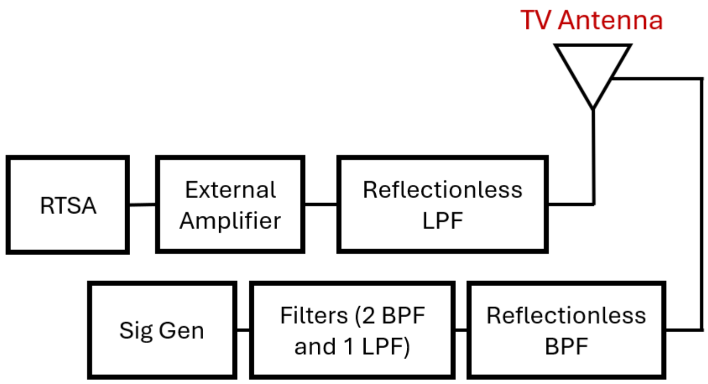

Figure 5.3: Receive side block diagram for the cross-frequency effective aperture measurement for the parametrically-tuned receive antenna.

5.1.1 Cross-Frequency Effective Aperture

Typical receive gain measurements for antennas use a VNA such that a single frequency is sent and received at one time and then swept for different frequencies. This measurement method is valid for LTI antennas as no other relevant frequency behavior is expected other than that at the signal frequency. However, for non-LTI antennas, frequency behavior other than that at the signal frequency is expected and therefore necessary to measure and characterize using cross-frequency effective aperture. In order to do so, a spectrum analyzer is used in tandem with a signal generator to send a single frequency but capture a broad range of frequency behavior. This allows for the study of the expected harmonic behavior from the non-LTI antenna which is key to fully characterizing the device.

The block diagram for the receive side of the cross-frequency effective aperture measurement is shown in Fig. 5.2 for the LTI prototype antenna and Fig. 5.3 for the time-varying prototype antenna. While the measurement setups for the two prototype antennas are generally the same, the time-varying antenna must make use of an additional signal generator on the receive side to generate power at the pump frequency necessary for parametric amplification. This also requires additional filtering on the time-varying antenna's pump port to reduce noise leakage from the signal generator. A reflectionless lowpass filter is used after the signal port in the time-varying antenna measurement setup to decrease the power at the harmonics and pump frequency before the LNA. This filter is not used in the LTI measurement setup as the lowpass filter is treated as part of the time-varying antenna rather than part of the measurement setup. The primary purpose of the LNA is to decrease the apparent noise figure of the rest of the receive system increasing the measurement SNR. The use of the LNA also allows for minimal changes to be made between the received power measurement setup and the noise characterization setup. A representation of the measurement setup in the anechoic chamber for the parametrically-tuned receive antenna case can be seen in Fig. 5.4. Not pictured in the chamber block diagram is the use of discrete barrel DC blocks on the spectrum analyzer and the pump signal generator for added protection against errant DC signals. The DC power supplies that allow for the DC biasing of the varactor diode on the aperture of the time-varying antenna and the operation of the LNA after the antenna under test are also omitted for simplicity.

To begin the measurement, a calibrated receive antenna is used in place of the LTI antenna with the same setup as in Fig. 5.2. For this work, the calibration antenna used is a TEKBOX TBMA1 biconical antenna. This antenna serves as part of a calibration step to provide an offset to apply to subsequent antenna measurements that calibrates out losses or gains in the rest of the receive side as well as in the transmit side. This is the same method commonly used in standard antenna gain measurements when a calibrated antenna with a known gain is available. A very wideband calibration antenna or multiple calibrated antennas might be necessary for cross-frequency effective aperture measurements due to the wide frequency ranges necessary to capture the harmonic behavior of non-LTI antennas. Once the received

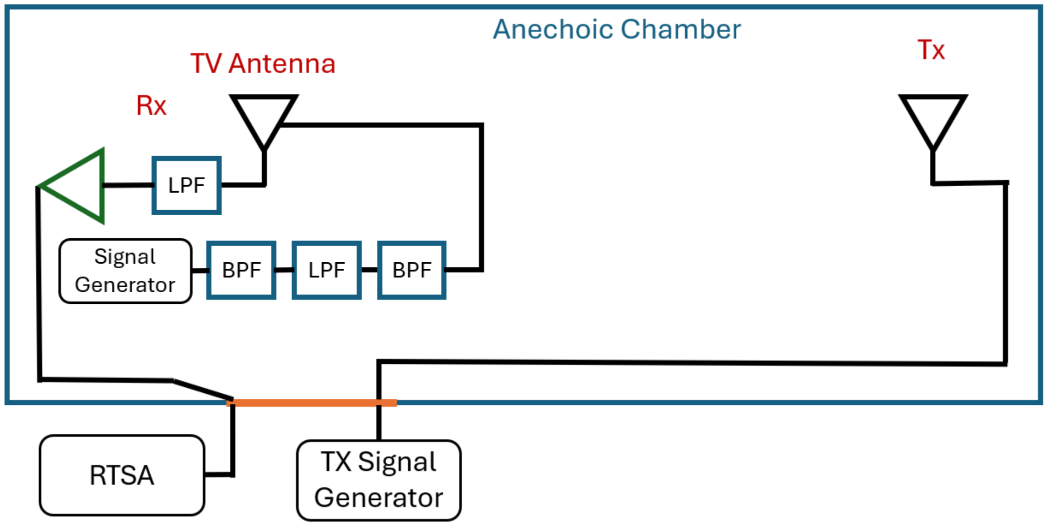

Figure 5.4: An overview of the time-varying antenna setup for the various measurements taken in the work. The blue rectangle represents the anechoic chamber with the orange line at the bottom of the chamber representing the bulkhead connections to the outside.

power for the calibration antenna(s) is measured, the known effective aperture can be applied to create an offset to be used with the received power measured from the true antennas under test. It should be noted that any supporting components like amplifiers used in the setup and the transmit antenna must be able to adequately support the wide frequency range necessary to characterize the harmonics of the antenna under test. How many harmonics can be measured will be governed by the harmonic generation of the antenna under test and the dynamic range available in the measurement setup.

The effective aperture results for the parametrically-tuned receive antenna and the comparison LTI antenna around the signal frequency can be seen in Fig. 5.5. The measured results are shown with the simulated results obtained from the combined use of HFSS and ADS. The measured results shown good agreement with simulation with the peak effective apertures measured to be within 0.5 dB of simulation. The measured 3 dB effective aperture bandwidths also compare favorably to simulation with agreement to within 0.15 MHz of bandwidth. The measured LTI antenna has a peak effective aperture of -3.2 dBsm and bandwidth of 0.9 MHz and the parametrically-tuned receive antenna has a peak effective aperture of -3.3 dBsm and a bandwidth of 3.2 MHz. This results in the time-varying antenna boasting over a 3.5x effective aperture bandwidth improvement over the comparison LTI antenna.

The cross-frequency effective aperture of the parametrically-tuned receive antenna was also measured. The results can be seen in the plots shown in Fig. 5.6. The transmitted frequency was swept along the x-axis of the plots while the measured frequency content is shown along the y-axis. The color of each pixel in the plot corresponds to the effective aperture measured at each receive frequency for each transmitted frequency with values below -65 dBsm not plotted. The power seen at the pump frequency of 591 MHz is due to leakage from the pump port to the signal port and is not due to transmitted power. It can be seen that as the transmit frequency is swept, it is received by the time-varying antenna which generates two measurable harmonics–the first sum and difference harmonics of the time-varying antenna. Other harmonics are no doubt present on the aperture of the antenna, but are at levels too low to be easily captured using this measurement method.

5.2 Emissions Measurements

The measurement of the unintended emissions of the parametrically-tuned receive antenna is of importance as they can interfere with the operation of other RF systems nearby. The main unintended emissions studied in this section is of the pump frequency. A fairly strong pump power of approximately 16.6 dBm is presented to the pump port of the time-varying antenna in normal operation which can

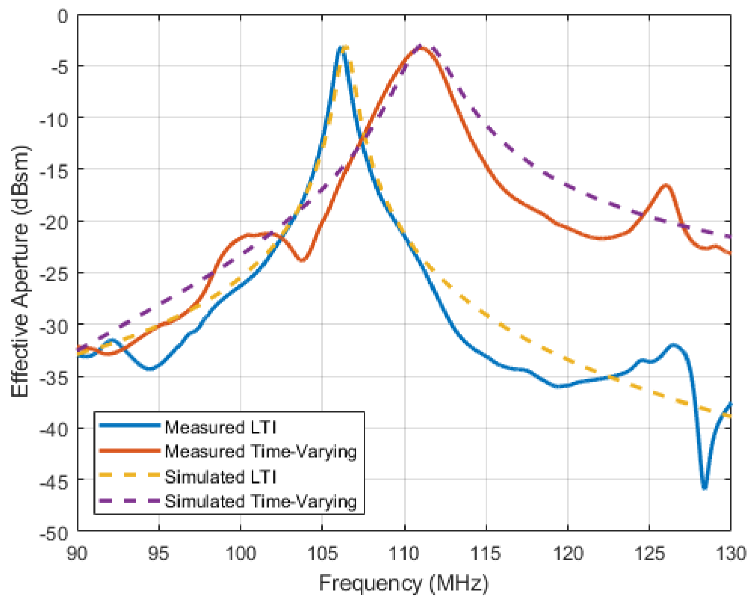

Figure 5.5: Effective aperture results comparing the LTI antenna and the parametrically-tuned receive antenna with each other and with the results from simulation.

then be unintentionally radiated to the outside environment.

The measurement setup differs from the other setups described earlier in this work as a result of effectively swapping the transmit and receive antennas. The LTI transmit antenna, in the form of a biconical antenna which had previously been used to transmit a single continuous wave frequency to the parametrically-tuned receive antenna and LTI antenna for the received power measurements, is now used as the transmit antenna. The parametrically-tuned receive antenna is then biased and pumped with 16.6 dBm of power at the pump frequency. The unintended radiation is then received by the biconical antenna and measured by the spectrum analyzer. A representation of the over-the-air unintended emissions testing measurement setup is shown in Fig. 5.7.

The measured results of the emissions test can be seen in Fig. 5.8. As expected, the power at the pump frequency is reradiated by the parametrically-tuned receive

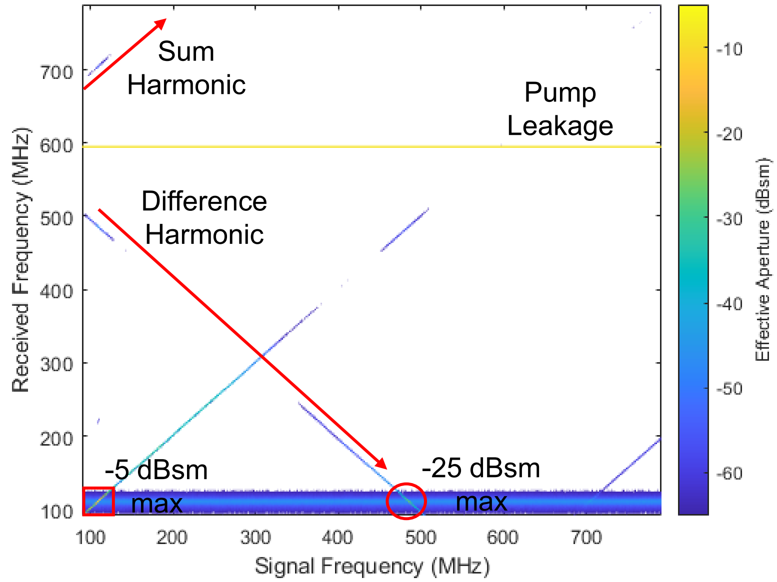

(a) Total measurement space.

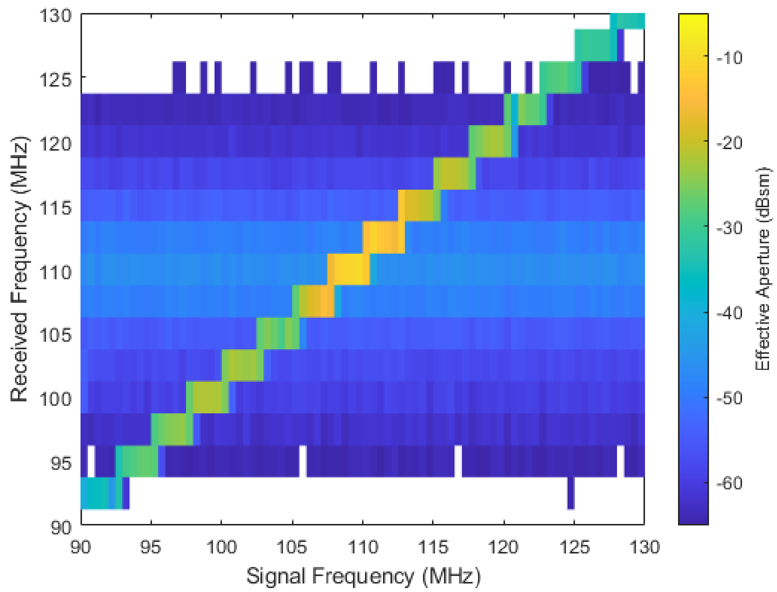

(b) Zoomed in on the primary signal frequencies.

Figure 5.6: Results from the realized cross-frequency effective aperture measurement. The transmitted signal frequency is swept while measurements are taken across a wide frequency spectrum for every transmitted frequency iteration.

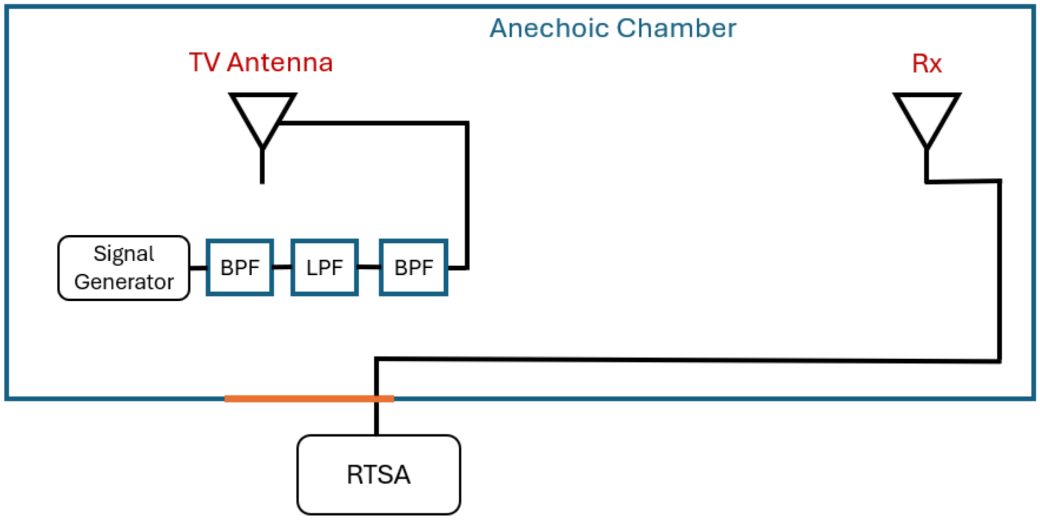

Figure 5.7: Measurement setup for emissions testing of the parametrically-tuned receive antenna within the anechoic chamber.

antenna into free space and is captured by the measuring antenna. The re-radiated signal at the pump frequency is somewhat attenuated by the filters on the aperture, but the issue persists.

Future improvements could be made to this measurement method to better align with existing LTI radiated emissions standards and testing procedures such as those outline in CISPR 16-2-3 [69]. This would include more rigorous methods and definitions for a number of items such as specific measurement distances between receive antenna and device under test, as well as cable placement of the device under test.

5.3 Conclusions

The receive aspects revolving around purely power–that is effective aperture and cross-frequency effective aperture–have been examined for the parametrically-tuned receive antenna and the LTI concentric loop antenna. The measured effective

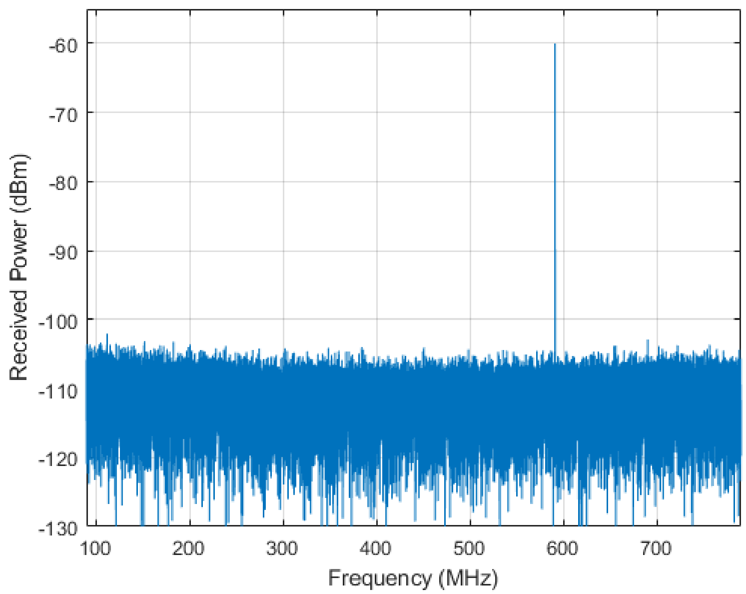

Figure 5.8: Power measured at the spectrum analyzer using a biconical antenna 7 meters from the parametrically-tuned receive antenna. The unintended emissions of the time-varying antenna comes from pump power leaking onto the aperture and being re-radiated.

aperture of both tested antennas align closely to simulation with the peak receive effective aperture being within 0.5 dBsm and the 3 dB bandwidth being within 0.15 MHz. As expected, the time-varying antenna produces measurable harmonics while the LTI comparison antenna does not. Finally, the unintended emission of power at the pump frequency from the time-varying prototype was studied and documented. Although the power receiving attributes of the prototype antennas have been considered, the modulated signal and noise characteristics remain to be discussed.

Chapter 6

Modulated Signal Characterization

Using modulated signals, especially those common in modern communication systems, provides a framework for testing receive systems in a realistic setting. Modulated signals, especially those that use both amplitude and phase information, can help highlight distortions that a receive antenna imparts onto a signal that wouldn't be caught using only received power and noise testing. This is especially important for parametrically-tuned receive antennas that use the degenerate architecture as they have been shown to have performance that is reliant on the phase relationship between the incoming signal and the pump frequency [32]. Since the phase of the incoming signal can't easily be controlled on receive and adjusting the phase of the pump frequency on the fly to line up with the incoming signal is extremely complicated, the performance of degenerate parametrically-tuned receive antennas cannot be guaranteed. While the receive based time-varying antenna shown in [10] does do this, it suffers from only being able to handle simple, smoothly varying frequency content like that found in FM data. For modulated signals that rely on phase information, the sudden changes in phase can result in distortions and increase the error in the received signal. The phase-reliant performance is notably absent in the non-degenerate architecture used for the prototype discussed in this work, making it a significantly better candidate for use in commu-

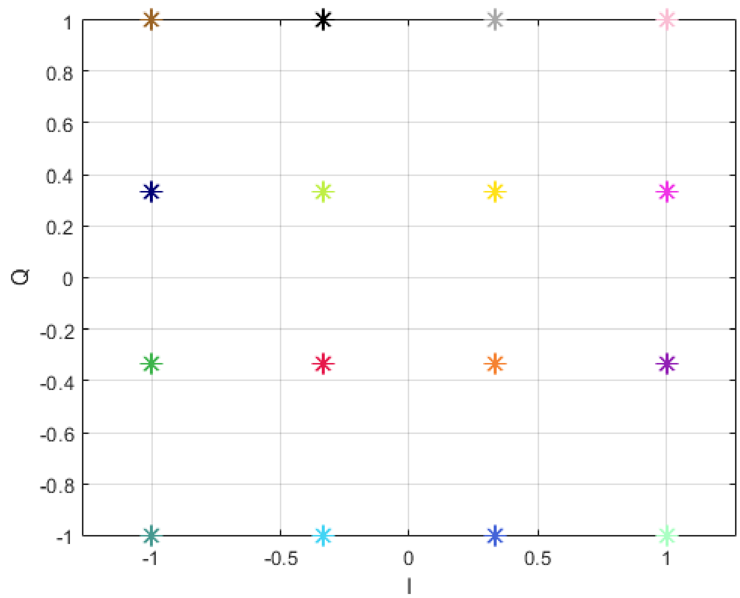

Figure 6.1: Constellation diagram for a 16-QAM modulation scheme with ideal symbol points marked.

nications on receive.

The figure of merit for the testing here, and a key figure of merit for communication systems in general, is error vector magnitude or EVM. This is a measure of how far the received symbol strays from the ideal symbol in terms of its in-phase and quadrature (I and Q) components. The received symbols can be plotted on a graph of the in-phase versus quadrature components known as a constellation diagram. For different modulation schemes, the ideal symbols correspond to different positions on the constellation diagram based on the relative value of their in-phase and quadrature components. An example of the constellation diagram for a 16-QAM modulation scheme can be seen in Fig. 6.1 with the ideal symbol points marked. As the name would suggest, a 16-QAM modulation scheme is composed of 16 different symbols with each symbol being composed of four bits. The EVM of a particular received symbol is measured as the distance between the received

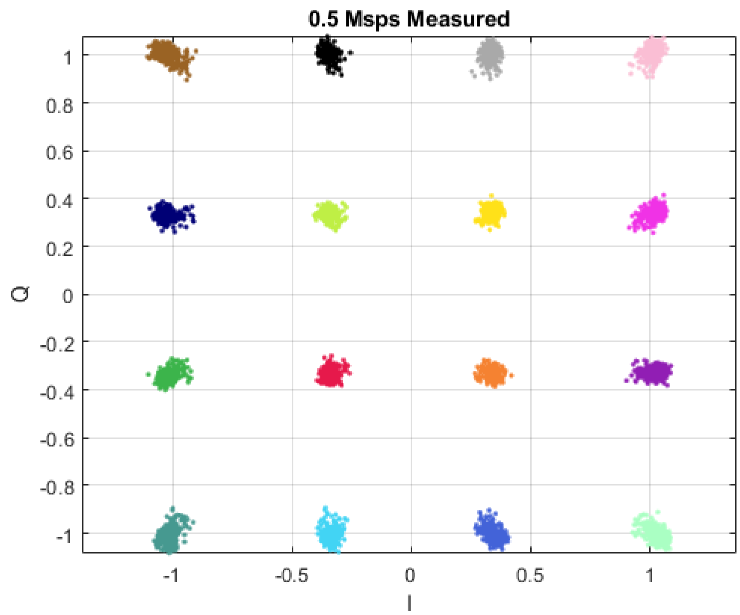

Figure 6.2: Constellation diagram for a measured received signal using a 16-QAM modulation scheme.

symbol on the constellation diagram and the ideal location of where the received symbol should have been. An example of what measured results might look like can be seen in Fig. 6.2 with receive symbols clustering near where the ideal symbols should be.

The measurement setups for the parametrically-tuned receive antenna and the LTI antenna remain the same as those discussed in 5.1.1 but using modulated signals rather than sweeping single frequency continuous waves. The measurement setup in the anechoic chamber can once again be seen in Fig. 6.3. For the OOK signal, an amplitude shift keyed signal is generated using the SMCV100B signal generator while for the 16-QAM testing the built in 16-QAM modulation scheme is used. For all the testing a known 4096 symbol sequence is used.

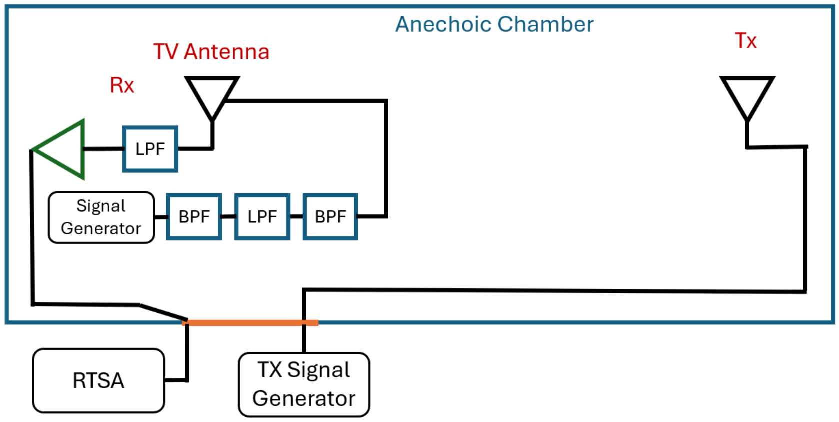

Figure 6.3: An overview of the time-varying antenna setup for the modulated signal testing. The blue rectangle represents the anechoic chamber with the orange line at the bottom of the chamber representing the bulkhead connections to the outside.

6.1 OOK in the Time Domain

Looking at received On and Off Keyed (OOK) signals in the time domain can help build an intuition for modulated signals and how distortions caused by receive systems affect them. These distortions are typically caused by a lack of bandwidth in the receive system for the received signal. In the time domain for an OOK modulated signal this manifests as rise and fall times that are too large to accurately represent the true transmitted signal. An example of this can be seen in Fig. 6.4 with the true OOK signal shown in purple and the distorted receive signals caused by a lack of bandwidth shown in blue, orange, and yellow. When the rise and fall times are too long, the previous symbol impacts the current symbol, resulting in intersymbol interference or ISI. This distortion can destroy a receive system's ability to accurately discern the information being sent. In receive systems that utilize electrically small antennas employing standard conjugate matching, the matched antenna can be a primary bandwidth bottleneck. This bandwidth bottleneck limits the maximum data throughput of the receive system even when the SNR is high.

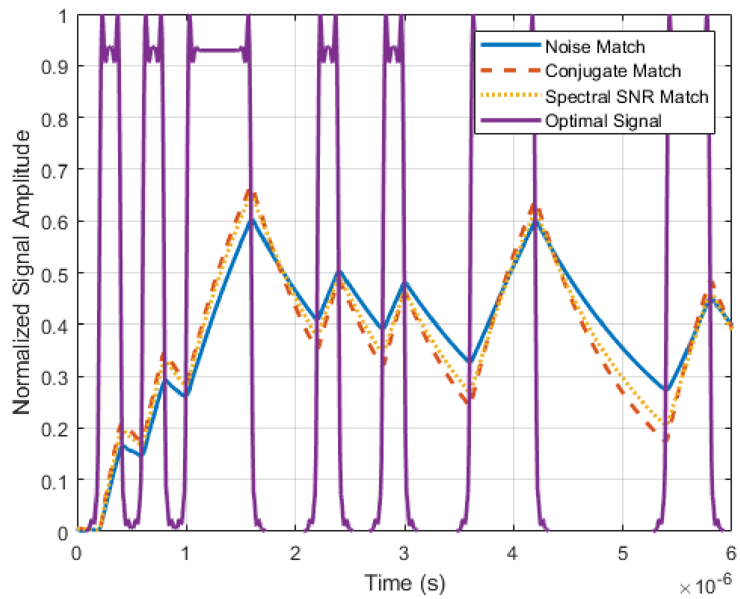

Figure 6.4: Time domain of a normalized OOK signal with the true transmitted signal as well as distorted received signals.

6.2 16-QAM Signal Characterization

Since the point of the modulated signal measurement is to test the receive antennas ability to receive information, a 16-QAM test signal is a good benchmark. A 16-QAM modulation scheme incorporates both amplitude and phase modulation, which would help identify any amplitude or phase distortions that might occur with the antenna under test. In addition, a 16-QAM modulation scheme is widely used in communications today allowing for a realistic test bed.

The 5120 symbol 16-QAM signal is generated using an SMCV100B signal analyzer and transmitted using a Tekbox TMBA2 antenna. This signal is then received using the antenna under test, passed through a low noise amplifier, and then received by the spectrum analyzer. The spectrum analyzer then demodulates and equalizes the signal using a 10 symbol length real time equalizer with two samples per symbol.

6.2.1 Instantaneous Channel Bandwidth

To corroborate that the increased effective aperture bandwidth of the time-varying prototype over the LTI comparison antenna seen in 5.1.1 is usable, a 16-QAM signal is sent to each test receive system at their respective center frequency with various symbol rates. Looking at EVM as the symbol rate is increased for a single data stream at the center frequency of the antenna under test can be used as a proxy for bandwidth. For a signal with high SNR, a sudden increase in EVM as symbol rate is increased indicates intersymbol interference which can be a major source of distortion. This distortion in the received signal occurs when the bandwidth of the receive system is not adequate to support the symbol rate of the modulated signal. While this distortion can be overcome with the use of equalizers, this comes at the cost of computational power and time. Equalizers that are able to compensate for larger and larger distortions caused by the signal bandwidth outstripping the receive system bandwidth take more time and more computational resources to restore the signal to usable levels. In addition, equalizers can degrade the SNR of the received signal as it amplifies both the signal and the noise to compensate for drooping.

The EVM performance of the LTI and time-varying antenna for the 16-QAM test signal using various symbol rates can be seen in Fig. 6.5. As the symbol rate is increased, the EVM slowly increases until the intersymbol interference becomes too great for the equalizer to overcome after which the EVM increases rapidly. A threshold value of 12.5% RMS EVM is chosen as the comparison point between the two antennas as this corresponds to the maximum allowable EVM for 5G NR 16-QAM signals [70]. At this threshold value, the LTI antenna is able to successfully receive a 16-QAM signal with a symbol rate of approximately 1.71 Msps while the parametrically-tuned receive antenna is able to receive the same signal with a

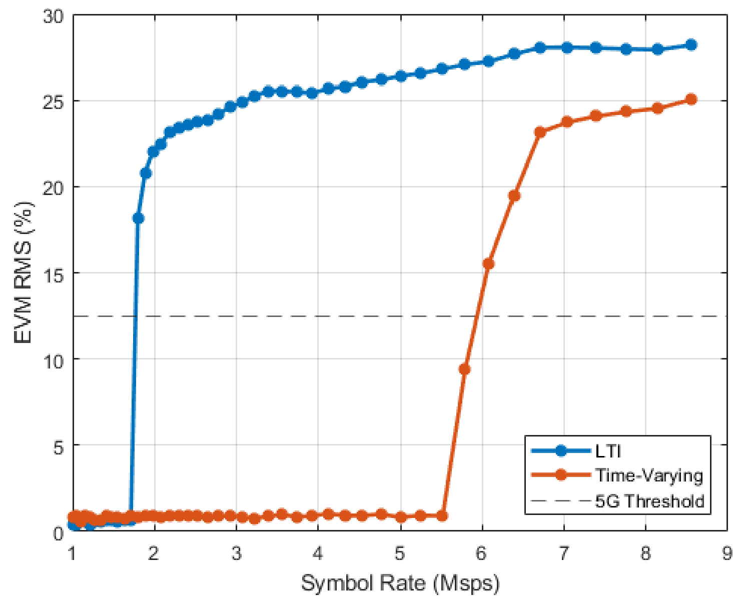

Figure 6.5: Measurement results for the instantaneous channel bandwidth test comparing the EVM results between the LTI antenna and the parametrically-tuned receive antenna for various data rates using a 16-QAM signal.

symbol rate of approximately 5.92 Msps. This represents an approximately 3.5 time increase in the maximum achievable symbol rate for this 16-QAM modulated signal using this receive system and matches the effective aperture bandwidth increase seen in Fig. 5.5.

6.2.2 Multi-Channel Bandwidth

While the previous section focused on a single receiving channel with a growing bandwidth, also of concern is the multiplexing of multiple signal channels using the same receive system. This requires a receive system, and therefore the receive antenna, to be able to support multiple small channels of smaller bandwidths at the same time. This is widely used in common communications schemes like orthogonal frequency-division multiplexing (OFDM) where a larger band of frequencies is

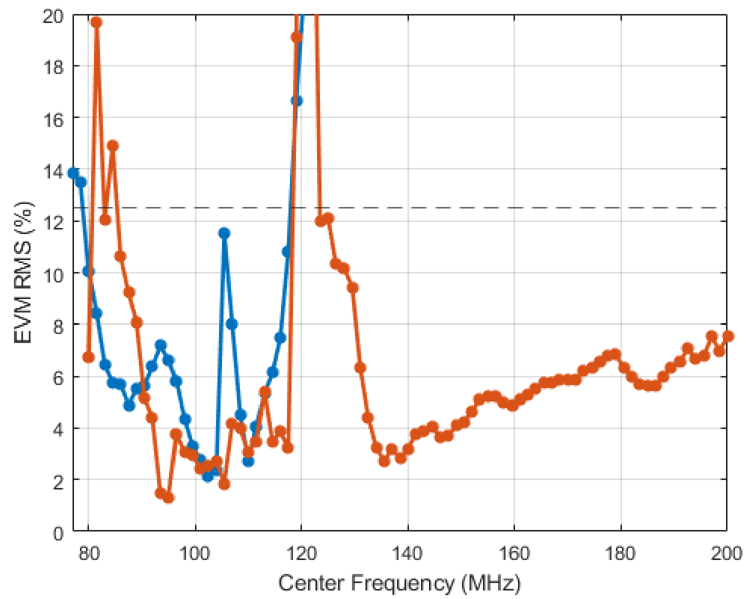

Figure 6.6: Measurement results for the multi-channel EVM test comparing the parametrically-tuned receive antenna and the LTI antenna using a 16-QAM modulated 1.5 Msps signal shifted to different center frequencies.

subdivided into many channels, each sending and/or receiving information.

To measure the ability of a receive antenna to support multiple smaller channels the following test was run with both the time-varying and LTI antennas. A 16-QAM modulated signal with a fixed symbol rate of 1.5 Msps is sent to the antenna under test at its center frequency. The center frequency of the transmitted signal is then swept in steps of 1.5 MHz both above and below the center frequency of the antenna under test. The EVM for each 1.5 MHz channel is then recorded for the two test antennas.

The results of the multi-channel EVM measurement can be seen in Fig. 6.6 for the LTI antenna and the parametrically-tuned receive antenna. The frequency band for which the EVM remains below the acceptable 12.5% threshold for the time-varying antenna is significantly larger than the LTI comparison antenna with the exception of the large spike at approximately 125 MHz. The LTI antenna also experiences a spike in EVM at this frequency, but the EVM never returns below the 12.5% threshold after this point unlike the time-varying antenna. The spike in EVM is caused by multipath interference as a result of the anechoic chamber in which the measurement was taken and not due to the antennas under test.

Measurement Issues

Unfortunately, issues during measurement occurred due to the limitations of the anechoic chamber used. The anechoic chamber is composed of predominately 40 cm long pyramid foam absorber which is rated down to approximately 300-500 MHz–significantly higher than the operating of the antennas under test around 110 MHz [71]. The foam is not able to adequately absorb the energy of the non-direct paths from the transmit antenna to the antenna under test leading to multipath issues. While larger foam absorber is present in the chamber in many of the areas where the main non-direct paths are most likely to occur, it is absent right behind the transmit antenna. This is likely due to the assumption that the transmit antenna is directive, but the antenna used for this testing is a non-directive biconical antenna. A directive antenna around 110 MHz was not available for use and would otherwise be prohibitively large for use in this chamber.

The potential multipath issue discussed above manifests itself as a large null in the receive power of all of the antennas under test around 127 MHz which can be seen in Fig. 6.7. This is further corroborated by viewing raw S_{21} data of the biconical antenna in the time-domain as in Fig. 6.8. The first large response, highlighted in orange, corresponds to the desired direct path from the transmit antenna to the antenna under test while the second peak is the main multipath interference. The time delay between the two responses gives a distance of 2.8 meters which is twice the distance between the transmit antenna and the back wall of the chamber.

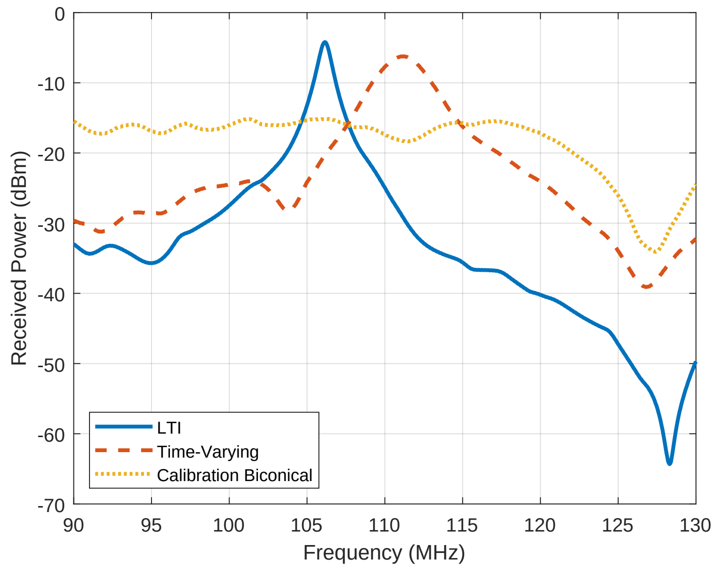

Figure 6.7: Received power of the various antennas under test with a null in received power due to multipath at approximately 127 MHz.

This lends credence to the idea that the large null seen in all the receive antennas is indeed multipath and that the multipath is coming from the reflection off the wall behind the transmit antenna.

The multipath is not much of an issue for the other measurements discussed in this work as it lies outside the main band of interest. In addition, since the drop in power from multipath happens at approximately the same frequency for all of the antennas, including the biconical antenna used for calibration, the multipath can be calibrated out. The mitigation via calibration only works, however, for measurements that rely purely on received power and therefore does not mitigate the multipath issues for modulated signals. For modulated signals multipath not only impacts the received power of the signal, but it also can results in intersymbol interference as the antenna receives multiple copies of the same stream of data slightly delayed in time. The intersymbol interference was the largest contributor to the EVM spike seen in Fig. 6.6 at approximately 125 MHz.

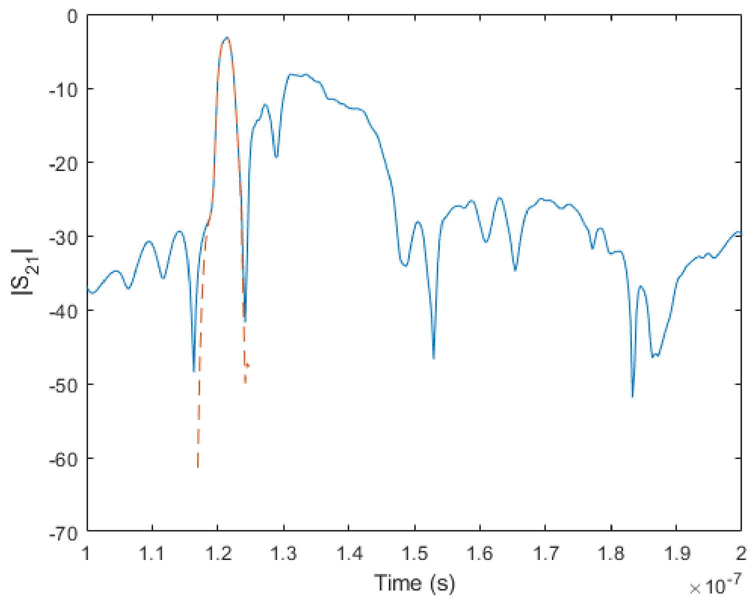

Figure 6.8: Time domain of an S_{21} measurement using the calibration biconical antenna which showcases the second spike in received power from the multipath.

A number of methods were attempted to mitigate the multipath issue for the multi-channel EVM measurement, but none were ultimately successful in fully eliminating it. The transmit power was calibrated using a calibration antenna to try to minimize the impact of chamber effects on the receive power. This improved the consistency of the multi-channel EVM measurement, but the EVM spike was still present due to ISI. The height of the transmit antenna was also varied in an attempt to change the interfering multipath. This did indeed shift the multipath issue slightly in frequency, but it did not ultimately fix it. A smaller transmit biconical antenna was used to increase the distance between the back wall and the antenna and additional foam absorber was added. This slightly decreased the prevalence of the multipath, but the large spike in EVM was still present. Finally, the transmit antenna was extended further into the middle of the chamber, increasing the distance between it and the back wall. This moved the multipath issue slightly down in frequency to approximately 118 MHz, but it did not eliminate the issue.

6.3 Conclusions

Modulated signal testing was conducted using 16-QAM modulated signals in an effort to ensure that the bandwidth increase of the time-varying antenna showcased in Ch. 5 was usable for information. The single channel, instantaneous bandwidth EVM measurement corroborated this by showing that the 3.5 times improvement in effective aperture bandwidth of the time-varying antenna over the LTI antenna also results in a 3.5 times improvement in symbol rate throughput with a modulated signal. A pseudo-multi-channel measurement was also attempted to showcase the usefulness of the parametrically-tuned receive antenna in an OFDM use case. Unfortunately, multipath issues in the anechoic chamber led to degradation in the performance of the antennas under test. This was not an issue of the antennas themselves and some attempts to mitigate the impact of the multipath was discussed.

Chapter 7

Receive System Noise Characterization

The noise characteristics of a receive system is of utmost importance when trying to maximize the performance of said receive system. The noise in a receive system can and will directly impact the maximum data throughput a receive system can process in a communications environment and can degrade sensitivity in power sensing applications. Since the noise in a receive system has such a large impact on performance it becomes very important then to accurately characterize the noise contributed by components in a receive chain. One of the most significant components to study in a receive system is the receive antenna as it sets the maximum instantaneous signal-to-noise ratio achievable by the receive system.

An investigation and analysis of two different techniques for measuring the noise contribution of both linear, time-invariant (LTI) and time-varying antennas in a practical manner is presented here. In Section 7.1, a method for measuring the noise figure of a receive system including the receive antenna is discussed that relies on isolated measurements of the gain of the antenna as well as a signal-less received power measurement similar to that used in [72]. In Section 7.2, the more well known Y-Factor measurement method is applied to the LTI and time-varying receive systems. The results of the two different methods are then compared and the noise figures of the LTI and time-varying antennas are showcased.

7.1 Isolated Received Noise Measurement

The isolated noise measurement method requires the gain of the antenna device under test which in turn requires a calibration measurement using an antenna with a known gain. The calibration measurement ensures that any additional losses from the transmit antenna, or the rest of the receive system are accounted for as with a standard antenna gain measurement method. The only non-standard procedure used to measure the calibration antenna and the antenna device under test is the use of a signal generator and RTSA rather than the more common vector network analyzer (VNA). This is to capture information from the harmonics of the non-LTI antenna device under test which would not be accurately captured with just a VNA. Once the gain of the antenna device under test is known, the same receive system setup is used to measure the received power without transmitting any signal. In effect, only the external noise captured by the antenna device under test and the noise internal to the system is measured. These results, as well as the noise figure of the RTSA by itself, are then used to find the noise figure of the total receive system using

$$NF = 10\log_{10}(1 + \frac{N_a}{N_i G_{AUT}}), \tag{7.1}$$

where G_{AUT} is the gain of the antenna under test, N_i is the ideal noise floor of the RTSA based on the pre-amplifier and the resolution bandwidth used, and N_a is the total measured noise at the RTSA from the isolated noise measurement using the AUT. For these measurements the RTSA is set to a resolution and video bandwidth of 10 kHz with an average detector averaging 500 times in order to reduce the noise floor of the RTSA.

An isolated noise measurement with no transmitted signal is collected and combined with the gain results of the corresponding antenna shown in Fig. 5.5 to find the noise figure of the two antenna receive systems under tests shown in Fig 7.1. The areas of minimum noise figure for the two receive systems occur when the antennas reach their peak gain as this increased gain minimizes the impact of noise further along the receive chain. The receive system with the LTI antenna has a lower minimum noise figure compared to the receive system with the non-LTI antenna. However, non-LTI antenna has a significantly wider bandwidth for which the noise figure of the receive system is at 23 dB compared to when the receive system using the LTI antenna is at 23 dB of noise figure. The increased minimum noise figure of the non-LTI antenna is due to noise and harmonics generated by the pump signal generator being amplified and mixed down into the signal band. The added filtering on the pump signal generator is not perfectly eliminating all of the noise and generates thermal noise of its own. The wideband amplifier present on the signal generator used generates wideband thermal noise which falls into the highly sensitive idler frequency of the time-varying antenna. This is a known issue that can be resolved in future iterations through the use of a dedicated voltage-controlled oscillator (VCO) as the pump source [12]. This can be further highlighted by removing one of the bandpass filters on the output of the pump source which results in a 6 dBm increase in the isolated noise measurement as seen in Fig. 7.2. By removing a filter, more noise from the pump source is able to leak onto antenna aperture and be coupled down into the observation frequency.

7.2 Y-Factor Noise Measurement

The Y-factor method is a widely used method to characterize the noise contribution of radio frequency components. It is valid for both LTI and time-varying

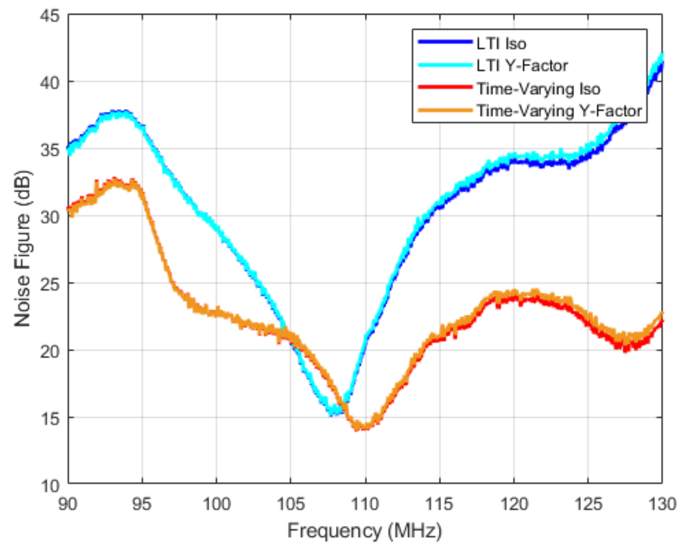

Figure 7.1: Calculated noise figures of the LTI and non-LTI receive systems using the isolated noise method.

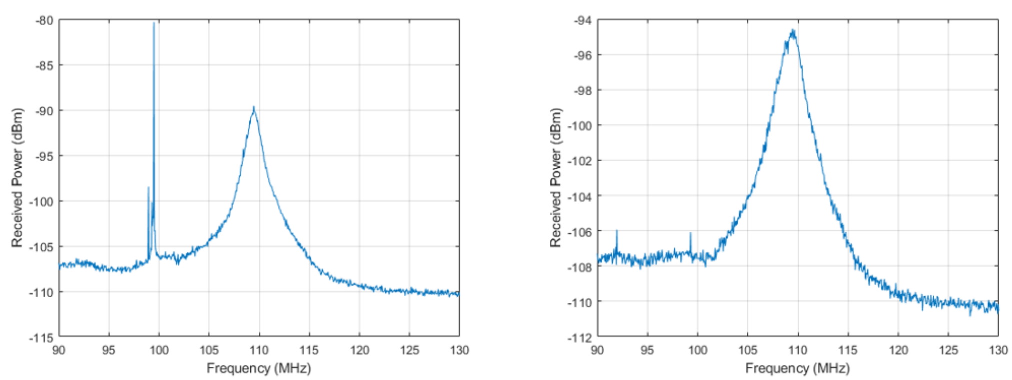

Figure 7.2: Receive power from the time-varying antenna with no signal present. (a) Isolated noise measurement without one of the bandpass filters present on the output of the pump source. A noise peak of -89 dBm is captured. An interferer is present at 99.7 MHz and is ignored. (b) Isolated noise measurement with all of the bandpass filters present on the output of the pump source. A noise peak of -95 dBm is captured. The cause of the interference at 99.7 MHz was found and turned off.

components, but does rely on an assumption of linearity. Typically this method is applied to two-port components using a noise source with a known output noise power. The device under test, or DUT, is connected to some measurement device capable of measuring power across frequency such as a spectrum analyzer on one side and connected to the noise source on the other side. A power measurement is then taken with the noise source in its off or “cold“ state, followed by a measurement with the noise source in its on or “hot” state. These two measurements are taken as a ratio known as the Y-ratio as seen in the equation

$$Y = \frac{P_{hot}}{P_{cold}}, \tag{7.2}$$

where P_{hot} is the receive power from the hot measurement in linear units and P_{cold} is the receive power from the cold measurement in linear units [73].

With the power ratio between the hot and cold measurements known, as well as the effective noise temperature output by the noise source in its hot and cold states, the effective noise temperature of the DUT can be found with the equation

$$T_{eq} = \frac{T_{hot} - Y \cdot T_{cold}}{Y - 1}, \tag{7.3}$$

where T_{hot} is the equivalent noise temperature of the hot measurement at the input of the device under test and T_{cold} is the equivalent noise temperature of the cold measurement at the input of the device under test [73].

This noise measurement method can also be applied to antennas and has been shown in the literature for directive antennas used in radio astronomy [74] - [76]. Instead of a noise source, these measurements typically use “cold“ portions of the sky with only small amounts of noise contributed by galactic emissions and cosmic background radiation as the cold source. The hot source typically used is the sun or anechoic foam at room temperature covering the antenna aperture.

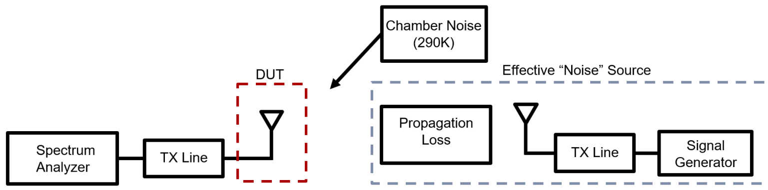

Figure 7.3: Block diagram of the proposed antenna Y-Factor measurement setup.

Unfortunately this same approach cannot be used for non-directive antennas like electrically small antennas, as small patches of hot and cold sky cannot be effectively targeted. Instead, a different approach is used with all measurements taking place inside an anechoic chamber to combat outside noise and interference that may corrupt the measurements. Instead of a wideband noise source that is typically used, a signal generator is used here to produce a continuous wave output at a single frequency. This single frequency can then be swept across to produce noise measurements across frequency one frequency at a time. This approach allows for finer control of output power used at each frequency for the Y-factor measurements. This can be leveraged when measuring time-varying antennas to produce controllable amounts of noise at the harmonics for additional noise characterization.

The block diagram for the proposed antenna Y-Factor measurement is shown in Fig. 7.3. The output power from the signal generator is transmitted to the DUT antenna with a transmit antenna with known radiation and noise characteristics. The signal generator outputs a signal at two different power levels, the lower power level corresponding to the cold measurement and the higher power level corresponds to the hot measurement. The DUT antenna receives the signal which is then sent to a spectrum analyzer for measurement. A second Y-factor measurement needs to be done to characterize the noise contributed to the measurements by the spectrum analyzer itself as well as the transmission line connecting the DUT to the spectrum analyzer. The noise contributed by the spectrum analyzer and transmission line is then subtracted from the first Y-factor measurement to find the noise contributed by the DUT.

7.2.1 Step-by-step Antenna Y-Factor Derivation

The Y-Factor method has been shown for antennas, but a derivation walking through the methodology is helpful [49], [74], [75], [76]. To begin, a continuous wave signal at a single frequency is generated with the signal generator. This signal is then carried to the transmit antenna with a transmission line resulting in a power delivered to the transmit antenna of

$$P_{TxAnt} = \frac{N_{pow}}{\text{TxLoss}_{Tx}} + kT_0 B_{RBW}(\text{TxLoss}_{Tx} - 1), \tag{7.4}$$

where N_{pow} is the power of the signal from the signal generator, TxLoss_{Tx} is the loss of the transmission line – or the reciprocal of the gain – on the transmit side in linear units greater than one, k is Boltzmann's constant, T_0 is the reference temperature typically taken to be 290K, and B_{RBW} is the resolution bandwidth of the spectrum analyzer [59]. The transmit antenna then contributes its own noise based on its radiation efficiency, η_t, mismatch efficiency τ_t, and physical temperature T_{pt}, and transmits the combined noise with some gain, G_t [38]. This results in an overall transmitted power of

$$P_t = G_t \left(\frac{N_{pow}}{\text{TxLoss}_{Tx}} + kT_0 B_{RBW}(\text{TxLoss}_{Tx} - 1) \right). \tag{7.5}$$

This power is then wirelessly transmitted through free space a distance d to the antenna device under test (DUT). The power is first assumed to spread isotropically with a relationship of $\frac{1}{4\pi d^2}$ and is modified by the focusing effect of the transmitting antenna's gain, G_t. In addition, the anechoic chamber and the absorbing foam inside gives off a noise power proportional to the chamber's physical temperature, $T_{chamber}$. The portion of the power transmitted by the signal generator and affected by spreading losses is then modified by the antenna device under test's effective aperture, A_e. This gives the total power available to the DUT as:

$$P_{av} = \frac{A_e G_t \left(\frac{N_{pow}}{\text{TxLoss}_{Tx}} + kT_0 B_{RBW} (\text{TxLoss}_{Tx} - 1) \right)}{4\pi d^2} + kB_{RBW} T_{chamber}. \quad (7.6)$$

This total power available to the DUT is exactly what is needed to calculate the hot and cold temperatures for the Y-Factor measurement. All that remains is to turn P_{av} into an effective noise temperature by dividing by k and B_{RBW}:

$$T_{eff} = \frac{A_e G_t \left(\frac{N_{pow}}{\text{TxLoss}_{Tx}} + kT_0 B_{RBW} (\text{TxLoss}_{Tx} - 1) \right)}{4\pi k B_{RBW} d^2} + T_{chamber}. \quad (7.7)$$

The hot effective noise temperature for the Y-Factor measurement would be given by Eqn. 7.7 when a larger signal is generated from the signal generator, and the cold effective noise temperature would be given when a smaller signal is generated from the signal generator. To calculate the effective "hot" noise temperature at the aperture of the antenna under test for use in the Y-Factor method, the power received at the measurement instrument must be to the backtracked to the plane of the aperture of the antenna under test. This means the losses and gains in the receive system including that of the calibration antenna must be accounted for resulting in

$$T_{hot} = \frac{\frac{P_{hot}}{G_{\text{rec}}}}{kB_{RBW}}, \quad (7.8)$$

where T_{hot} is the effective hot temperature at the aperture of the antenna under test, P_{hot} is the power measured at the spectrum analyzer for the hot calibration measurement, G_{rec} is the gain of the receive system including the calibration antenna used for this calibration measurement, k is the Boltzmann constant, and B_{RBW} is the resolution bandwidth of the spectrum analyzer.

This external effective noise temperature is then received by the antenna device under test and then modified by its radiation efficiency, η_r, and its mismatch efficiency, τ_r. In addition, the antenna device under test adds thermal noise from losses equal to

$$T_{AntLoss} = T_{pr}\tau_r(1 - \eta_r), \tag{7.9}$$

where T_{pr} is the physical temperature of the antenna under test in Kelvin. Lastly, the noise powers are transmitted to the receiver. The receiver in this example consists of a spectrum analyzer and a transmission line from the antenna under test to the spectrum analyzer. The spectrum analyzer has a noise temperature equal to T_{spec} while the transmission line has a noise temperature equal to

$$T_{\text{TxLoss}_{Rx}} = T_0(\text{TxLoss}_{Rx} - 1), \tag{7.10}$$

where T_0 is the physical temperature of the transmission line, and TxLoss_{Rx} is the loss in the transmission line. The total receiver noise temperature is then

$$T_{rec} = T_0(\text{TxLoss}_{Rx} - 1) + T_{spec}. \tag{7.11}$$

The loss in the transmission line applies to both the external noise temperature, T_{eff}, and the noise from the losses of the antenna $T_{AntLoss}$. Applying a kB_{RBW} factor then results in the power measured at the receiver for the hot measurement,

$$P_{hot} = \eta_r\tau_r kT_{hot}B_{RBW} + kT_{AntLoss}B_{RBW} + kT_{rec}B_{RBW}, \tag{7.12}$$

The same procedure can be done for a lower output power from the signal generator to obtain,

$$P_{cold} = \eta_r \tau_r k T_{cold} B_{RBW} + k T_{AntLoss} B_{RBW} + k T_{rec} B_{RBW}, \tag{7.13}$$

The Y-factor of the Y-factor measurement can then be represented by

$$Y = \frac{P_{hot}}{P_{cold}} = \frac{\eta_r \tau_r T_{hot} + T_{AntLoss} + T_{rec}}{\eta_r \tau_r T_{cold} + T_{AntLoss} + T_{rec}}, \tag{7.14}$$

where η_r is the radiation efficiency of the antenna under test and τ_r is the mismatch efficiency of the antenna under test. T_{hot} and T_{cold} are the effective noise temperatures at the aperture of the antenna under test from Eqn. 7.7 for a higher and lower power transmitted signal respectively. $T_{AntLoss}$ refers to the noise temperature due to the loss of an LTI antenna defined in Eqn. 7.9

Using Eqn. 7.14 in Eqn. 7.3 results in

$$T_{eq} = \frac{T_{pr} \tau_r (1 - \eta_r)}{\eta_r \tau_r} + \frac{T_{rec}}{\eta_r \tau_r}, \tag{7.15}$$

which is the noise of the antenna plus receiver system referred to the plane before the antenna under test.

To find the antenna loss noise temperature referred to the plane before the antenna under test, another Y-Factor measurement needs to be taken. This time the system under test consists of just the receive side transmission line and the spectrum analyzer. This is exactly the receive system in the previous measurement without the antenna under test. By finding the noise temperature of the receive system without the antenna and with Eqn. 7.15, the noise temperature contribution of just the antenna's loss can be found using

$$T_{DUT} = T_{eq} - \frac{T_{rec}}{G_{DUT}}. \tag{7.16}$$

Here G_{DUT} is the gain of the DUT found by the ratio of the differences between the two sets of hot and cold measurements from the two Y-Factor measurements

$$G_{DUT} = \frac{P_{hot} - P_{cold}}{P_{hot2} - P_{cold2}}. \tag{7.17}$$

For an LTI receive antenna this comes out to be $\eta_r \tau_r$, which is different than the typical antenna gain associated with directivity.

Solving for T_{DUT} results in a final equivalent antenna loss noise temperature of

$$T_{DUT} = \frac{T_{pr}\tau_r(1 - \eta_r)}{\eta_r \tau_r}, \tag{7.18}$$

which is exactly the internal noise temperature of a passive LTI antenna referred to the plane before the antenna. A linearity assumption is made for the Y-Factor method, but linear, time-varying antennas should be well modeled. Many more modifications not covered in this work need to be made if the Y-factor method is to be applied to non-linear devices [77].

Time-Varying Y-Factor

For time-varying antennas, the cross-frequency effective aperture properties of the antenna must be considered when using the Y-Factor method. The ability of time-varying antennas to couple power from their harmonics into the signal band of interest means that any noise present at these harmonics contribute to the degradation of the signal-to-noise ratio. This means that the Y-Factor method for time-varying antennas no longer measures just the noise figure due to the loss of the antenna as in the case of LTI antennas. The noise figure measured by the Y-Factor method for time-varying antennas is then heavily dependent on the external noise environment during the measurement.

Similar to the derivation of the Y-Factor method for LTI antennas shown previously, the form for time-varying antennas is given below. The same procedure is done starting with Eqn. 7.4 until Eqn. 7.14 with some modifications to account for the cross-frequency effective aperture properties of time-varying antennas. The modifications are primarily due to the two cross-frequency noise coupling phenomena: external noise coupling from harmonics to the signal frequency and thermal noise coupling from harmonics to the signal frequency. To accurately model coupled thermal noise from the harmonics to the signal frequency, a more detailed look at the time-varying antenna is necessary.

The time-varying antenna can be modeled using a method of moments (MoM) impedance matrix with conversion matrix method of moments (CMMoM) [16]. This breaks the antenna up into a multitude of different segments, each of which can potentially interact with each other segment at the same or at different frequencies. Using this representation of the time-varying antenna, the noise power delivered to the load R_0 at the observation port α from external noise at the 0^{th} harmonic is

$$T_{ext}^{ant} = \frac{R_0}{2k}[\hat{\mathbf{Z}}^{-1}\hat{\mathbf{C}}^V\hat{\mathbf{Z}}^{-H}]_{\alpha\alpha,00}, \tag{7.19}$$

where $\hat{\mathbf{Z}}$ is the uncompressed CMoMM representation of the antenna [25]. Here, k is the Boltzmann constant and $\hat{\mathbf{C}}^V$ is the associated spectral noise voltage covariance matrix given by

$$\hat{\mathbf{C}}_p^V = \frac{2\eta_0 k T_b^p}{\lambda_p^2}\int_\Omega \hat{\mathbf{V}}_{\hat{\mathbf{k}},p}\hat{\mathbf{V}}_{\hat{\mathbf{k}},p}^H \mathrm{d}\Omega. \tag{7.20}$$

T_b^p is the external brightness temperature and λ_p^2 is the free space wavelength at harmonic p. This assumes an isotropic background and that the excitation vector used to find the cross-frequency effective aperture, $\hat{\mathbf{V}}_{\hat{\mathbf{k}},p}$, comes from a direction $\hat{\mathbf{k}}$. Summing this for all the harmonics gives the $\hat{\mathbf{C}}^V$ term necessary in Eqn. 7.19 to find the power at the load R_0 for the signal frequency from external noise. This can then be presented in the more simplified form of

$$T_{ext}^{ant} = 4\pi \sum_p \frac{T_b^p A_e^p}{\lambda_p^2}, \tag{7.21}$$

where A_e^p is the cross-frequency effective aperture that maps the pth harmonic onto the signal frequency [25].

With the noise temperature contribution from external noise captured, the thermal noise contribution of the time-varying antenna can be studied. The same CMMoM representation is used as in Eqn. 7.19, but the noise contribution now captures thermal noise coupling rather than external noise coupling. This means that the spectral noise voltage covariance matrix for the thermal noise portion is now proportional to the loss resistance of each segment of the uncompressed CMMoM matrix:

$$\hat{\mathbf{C}}^V = kT \begin{bmatrix} R_1 & 0 & 0 \\ 0 & \ddots & 0 \\ 0 & 0 & R_N \end{bmatrix}, \tag{7.22}$$

where T is the physical temperature of the segments [64]. This culminates in the noise from the loss of the time-varying antenna observed at the 0^{th} harmonic, T_{int}^{ant}, and in general describes the cross-frequency coupling of thermal noise on time-varying structures.

The new equivalent noise temperatures of the time-varying antenna can then be input into Eqn. 7.12 and Eqn. 7.13 to obtain the new Y-Factor for the time-varying antenna of

$$Y_{TV} = \frac{P_{hot}}{P_{cold}} = \frac{T^{ant}_{extHot} + T^{ant}_{int} + T_{rec}}{T^{ant}_{extCold} + T^{ant}_{int} + T_{rec}}. \tag{7.23}$$

Plugging this into Eqn. 7.3 with arbitrary hot and cold effective noise temperatures present at each harmonic p we get:

$$T_{TVeq} = \frac{\left(T^0_{cold} - T^0_{hot}\right)\left(T^{ant}_{int} + T_{rec}\right) + 4\pi \sum_{p\neq 0} \frac{A^p_e\left(T^0_{cold}T^p_{hot} - T^p_{cold}T^0_{hot}\right)}{\lambda^2_p}}{4\pi \sum_p \frac{A^p_e\left(T^p_{cold} - T^p_{hot}\right)}{\lambda^2_p}}, \tag{7.24}$$

where T^p_{hot} and T^p_{cold} are the hot and cold effective noise temperatures at each harmonic, T^{ant}_{int} is the thermal noise from loss on the antenna at the observation frequency including the effects of cross-frequency coupling, and A^p_e is the cross-frequency effective aperture.

Not only is the noise figure of the time-varying antenna as measured by the Y-Factor method dependent on the thermal noise coupled from the harmonics to the signal frequency, the noise present at each harmonic has a noticeable impact on the result. While Eqn. 7.24 is the generalized result for arbitrary effective noise temperatures at the harmonics, it can be simplified for the case where the noise environment is consistent across frequency. When $T^p_{hot} = T^0_{hot}$ and $T^p_{cold} = T^0_{cold}$, Eqn. 7.24 becomes

$$T_{TVeq} = \frac{T^{ant}_{int} + T_{rec}}{4\pi \sum_p \frac{A^p_e}{\lambda^2_p}}, \tag{7.25}$$

greatly simplifying the result.

7.2.2 Uncertainties in the Antenna Y-Factor Measurement

Theoretical Measurement Uncertainty

There are a number of uncertainties that arise from the various components used in the Y-Factor measurement of an antenna including impedance mismatch present between components. While this has been factored into the antenna portion of the above derivation through the antenna's mismatch efficiency, there still remains some mismatch between the source and measurement instruments as well as the transmission lines that needs to be taken into account. In addition, there are uncertainties in the output power from the source as well as display jitters on the spectrum analyzer as it captures the received power. Taking multiple measurements and averaging can help reduce the uncertainties associated with these input and output jitters. By far the largest uncertainty contributor for this setup is due to the spectrum analyzer's high noise figure and the low gain from the electrically small antenna DUT. Small discrepancies in the measurement of the noise figure of the spectrum analyzer, which is on the order of 20 to 25 dB will overshadow the noise contributed by the antenna DUT which will has a noise figure on the order of 0.5 to 2.5 dB.

In order to mitigate the low gain of the antenna DUT and the large noise figure of the spectrum analyzer which has a negatively impact on the measurement uncertainty, a low-noise pre-amplifier between the DUT and the spectrum analyzer can be inserted. This serves to decrease the noise figure of said spectrum analyzer. By improving the gain between the DUT and spectrum analyzer, the effects of different cascaded uncertainties can be decreased.

The typical method to calculate the uncertainty is given by the equation,

$$\text{Measurement Uncertainty} = \sqrt{\begin{array}{r}\left(\frac{F_1}{F_{DUT}}\Delta F_{1\_dB}\right)^2 + \left(\frac{F_2}{F_{DUT}G_{DUT}}\Delta F_{2\_dB}\right)^2 \\ + \left(\frac{F_2 - 1}{F_{DUT}G_{DUT}}\Delta G_{DUT\_dB}\right)^2 \\ + \left(\left(\frac{F_1}{F_{DUT}} - \frac{F_2}{F_{DUT}G_{DUT}}\right)\Delta Source_{\_dB}\right)^2\end{array}}, \tag{7.26}$$

where F_1 is the noise factor of the entire measured system obtained from the Y-factor measurement, F_2 is the noise factor of the part of the system that constitutes the calibration portion of the measurement (the spectrum analyzer, receive side transmission line, and pre-amplifier if used), and ΔF_{1_dB}, ΔF_{2_dB}, ΔG_{DUT_dB}, and $\Delta Source_{\_dB}$ are in units of dB and are defined below [73].

The first uncertainty, ΔF_{1_dB}, is primarily due to the mismatch between the noise source and the input of the DUT as well as the uncertainty of the spectrum analyzer's noise figure and is given by:

$$\Delta F_{1\_dB} = \sqrt{\left(20\log_{10}\left(1 - \Gamma_{source}\Gamma_{DUTinput}\right)\right)^2 + \left(SA_{NF\_Uncertainty\_dB}\right)^2}, \tag{7.27}$$

where Γ_{source} is the output reflection coefficient of the noise source, $\Gamma_{DUTinput}$ is the input reflection coefficient of the DUT, and $SA_{NF\_Uncertainty\_dB}$ is the uncertainty in the noise figure of the spectrum analyzer in dB.

The second term in Eqn. 7.26 is similar to the first with the only major change being in the reflection coefficients used. This time the reflection coefficient for the input of the spectrum analyzer is used in place of the input of the DUT. The equation is

$$\Delta F_{2\_dB} = \sqrt{\left(20\log_{10}\left(1 - \Gamma_{source}\Gamma_{SAinput}\right)\right)^2 + \left(SA_{NF\_Uncertainty\_dB}\right)^2}. \tag{7.28}$$

It should be noted that if an external pre-amplifier is used in between the DUT and the spectrum analyzer, the pre-amplifier's input reflection coefficient must be used in place of the spectrum analyzer's input reflection coefficient.

The third term in the measurement uncertainty equation takes into account all of the mismatch uncertainties including the reflection coefficients of the source, the spectrum analyzer (or pre-amplifier), and the input and output reflection coefficients of the DUT. In addition, the spectrum analyzer's gain uncertainty will be taken into account. Again, if a pre-amplifier is used before the spectrum analyzer, the pre-amplifier's gain uncertainty is used. The equation is given by:

$$\Delta G_{DUT\_dB} = \sqrt{\begin{aligned}&(20\log_{10}(1-\Gamma_{source}\Gamma_{SAinput}))^2 + (20\log_{10}(1-\Gamma_{source}\Gamma_{DUTinput}))^2\\ &+ (20\log_{10}(1-\Gamma_{DUToutput}\Gamma_{SAinput}))^2 + (SA_{gain\_Uncertainty\_dB})^2\end{aligned}}. \tag{7.29}$$

The final term in the uncertainty equation is due to the uncertainty in the output power of the noise source. This should be simply given by the manufacturer of the noise source whether the noise source is a typical diode-based noise source or a signal generator. An example of the dramatic effect of the DUT's low gain on the measurement uncertainty can be seen in Fig. 7.4 for a fairly realistic example for the proposed measurement setup. In addition to decreasing the spectrum analyzer's noise figure through the use of a pre-amplifier, measuring the antenna's impact on the total system noise figure can help decrease uncertainty. Instead of having to work backwards through two Y-factor measurements, only one Y-factor measurement needs to be taken to find the overall system noise figure. Comparisons can then be made between a system using an LTI reference antenna and a system using a non-LTI antenna with higher certainty.

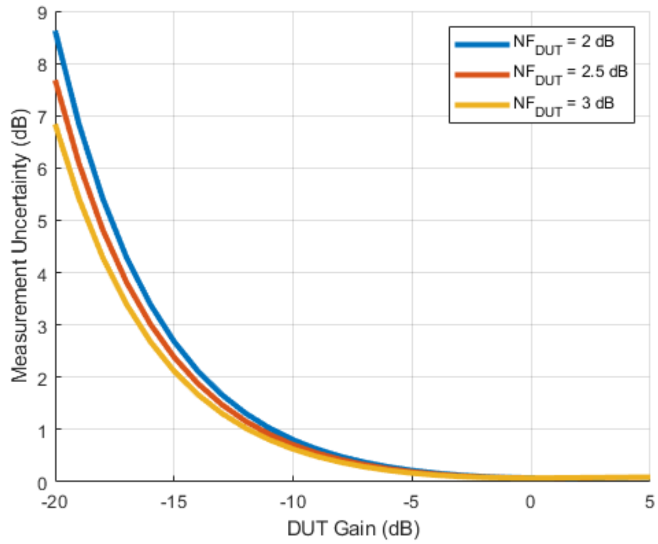

Figure 7.4: Y-factor measurement uncertainty for measuring DUTs of different noise figures using parameters from the proposed measurement setup.

Hot and Cold Temperature Uncertainty

Another source of uncertainty that is rarely discussed is the uncertainty associated with the difference between the expected hot and cold temperatures and the actual measured values. The delta between the expected and measured values is usually quite low, less than 0.5 dB, and is dependent on the noise figure and gain uncertainty of the spectrum analyzer. However, the impact of this uncertainty can vary tremendously. A theoretical example was produced in MATLAB using a DUT with a noise figure of 1.5 dB and an uncertainty factor added into the calculation for either the hot or cold temperature. If the cold temperature of the Y-factor measurement is relatively high, for example -100 dBm to -70 dBm, a slight difference between the expected and measured cold powers can drastically alter the noise figure of the DUT as seen in Fig. 7.5. If the cold temperature is taken to be 290 K, with the noise source off, the cold power that is measured is simply the spectrum analyzer's noise floor. This means there is almost no disconnect between the ex-

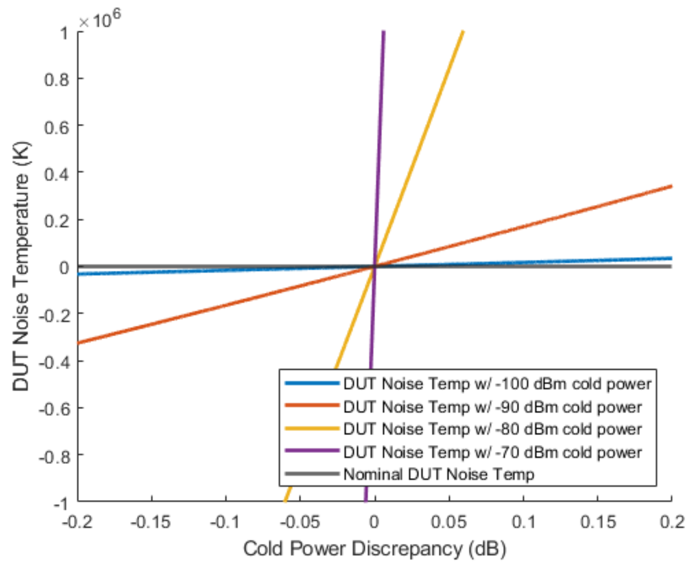

Figure 7.5: Measured noise figure of DUT for varying delta values between the expected and measured cold power.

pected and measured cold power. If the measured hot power is then varied from the expected value, the resulting difference in measured DUT noise figure is negligible as seen in Fig. 7.6.

7.2.3 Y-Factor Measurement Results

The Y-Factor measurement method was implemented in an anechoic chamber using a signal generator as the "noise" source and a real-time spectrum analyzer as the measurement device. The measurement uses the setup as in Fig. 7.7 for the LTI receive system and as in Fig. 7.8 for the time-varying receive system and seeks to measure the noise figure of the entire receive chain. An output power of 5 dBm from the signal generator was used for the hot measurement while the cold measurement was done with no transmit signal. The cold temperature was taken to be approximately 297 K corresponding to the physical temperature inside the anechoic chamber. A calibration biconical antenna was used to find the noise

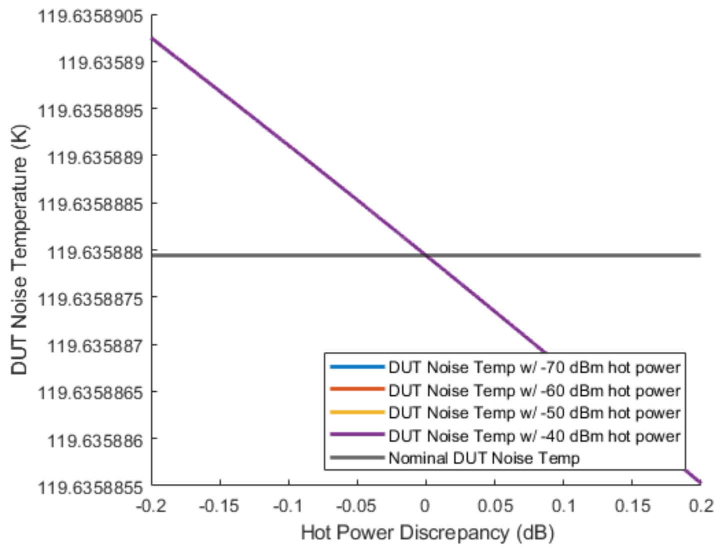

Figure 7.6: Measured noise figure of DUT for varying delta values between the expected and measured hot power with the cold temperature set to 290 K.

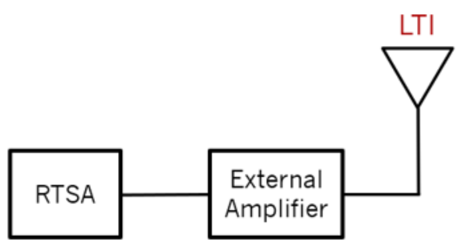

Figure 7.7: Block diagram of the LTI receive system used during noise testing.

temperature available at the aperture of the different antenna devices under test for the hot measurement.

The results for the Y-Factor measurements of the receive system using the LTI comparison antenna and the time-varying antenna is shown in Fig. 7.9. These vary slightly from the results comparing the isolated noise method and Y-Factor method showcased in Fig. 7.1 due to slight changes in the measurement setup and tuning of the antennas as they were taken on different days. The LTI antenna receive system is able to achieve a 1.5 dB lower minimum noise figure than the time-varying receive system shown in orange primarily due to the lack of cross-frequency thermal

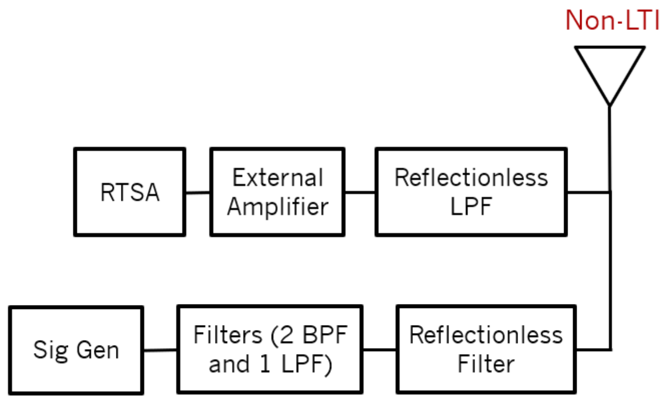

Figure 7.8: Block diagram of the non-LTI receive system used during noise testing.

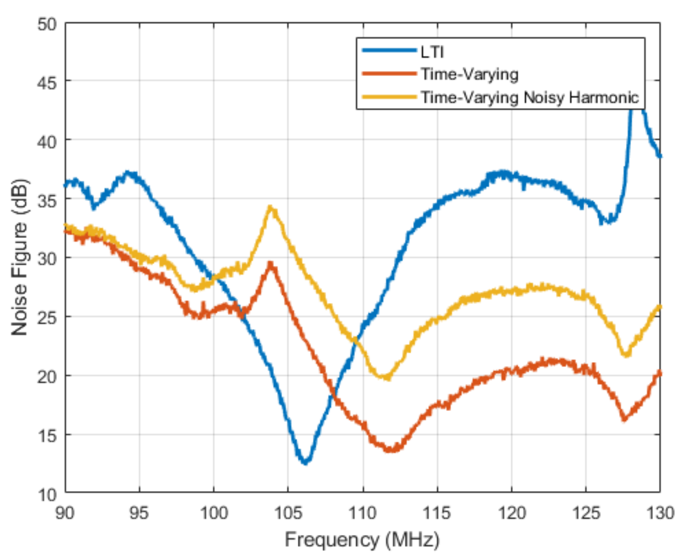

Figure 7.9: Noise figure results for the LTI and time-varying receive systems using the Y-Factor method.

noise coupling and lower overall antenna loss. The time-varying antenna system, on the other hand, is able remain below a system noise figure of 20 dB for 2.5 times as much frequency. The time-varying antenna system was also measured with an additional 40 MHz of -96 dBm/Hz additive white Gaussian noise (AWGN) centered at the idler harmonic which is shown in yellow. This additional noise at the idler frequency is able to couple down into the signal frequency and increase the apparent measured noise figure by approximately 6.5 dB.

The increased measured noise figure as a function of external noise present at the harmonics is a key characteristic of time-varying antennas to keep in mind when operating in a potentially congested frequency environment. Even if the primary signal band is free from interferers, out-of-band operators and noise may negatively impact the time-varying antenna receive system due to the antenna's ability to couple power from the harmonics down to the signal frequency.

7.2.4 Prediction of Cross-Frequency Noise Coupling

Since the cross-frequency effective aperture defines the cross-frequency coupling behavior of any power incident on the aperture of the time-varying antenna including external noise, the impact of noise at the harmonics on the noise figure measured at the observation frequency can be predicted. The additional noise present at the observation frequency, ω_0, due to some additional noise power flux density, S_{noise}, at the idler harmonic, ω_{-1} is given by

$$\text{Noise}_{\text{added}} = A_{\text{eff}}^{-1}(\omega_0) S_{noise}(\omega_{-1}) B_{RBW}, \tag{7.30}$$

where $A_{\text{eff}}^{-1}(\omega_0)$ is the cross-frequency effective aperture mapping power from the idler harmonic to the observation frequency and B_{RBW} is the resolution bandwidth

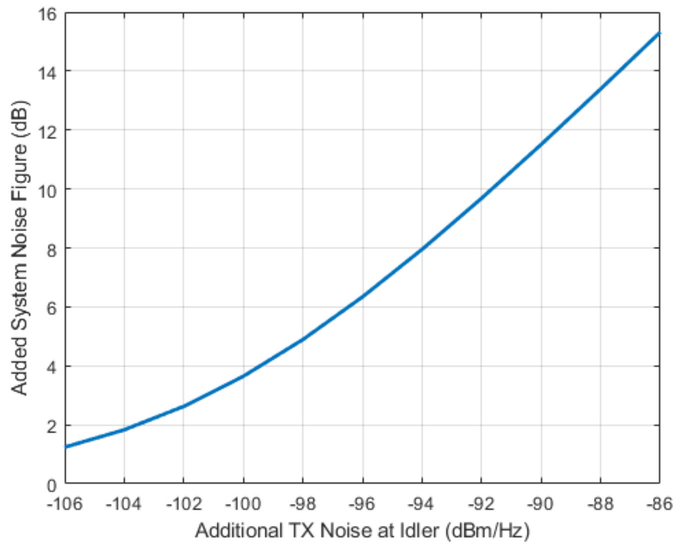

Figure 7.10: Increased noise figure of the receive system using the time-varying antenna at 111 MHz as a result of increased noise at the idler harmonic.

of the spectrum analyzer. This gives rise to the increased noise figure seen in Fig. 7.10 at the observation frequency of 111 MHz when additional noise is present at the idler harmonic. This noise figure is increased in comparison to the case where no additional noise is present at the idler harmonic with the increase calculated by

$$\mathrm{NF}_{\text{added}} = 10\log_{10}\left(\frac{S_{\text{sig}}/N(\omega_0)}{S_{\text{sig}}/\left(N(\omega_0)+\text{Noise}_{\text{added}}\right)}\right), \tag{7.31}$$

where S_{sig} is the signal power measured at the receiver for the observation frequency, $N(\omega_0)$ is the noise power measured at the receiver for the observation frequency, and $\text{Noise}_{\text{added}}$ is the added noise power due to noise coupling from the idler harmonic given by Eqn. 7.30. The result predicted from the -96 dBm/Hz case is within 0.2 dB noise figure of the measured difference between the orange and yellow cases seen in Fig. 7.9.

7.3 Conclusions

Measurement methods to quantify the noise characteristics of both LTI and time-varying antennas have been described with a focus on the Y-Factor method applied to electrically small antennas. This appears to be the first application of the Y-Factor method to time-varying antennas in order to measure their apparent noise figure in the literature. As such, derivations for both the LTI antenna Y-Factor method and the time-varying antenna Y-Factor method are provided. The results of the Y-Factor noise measurements highlight that while the time-varying antenna system has a 1.5 dB higher minimum system noise figure compared to the LTI antenna system, the noise figure bandwidth is larger. Additionally, the negative impact of external noise present at the harmonics of the time-varying antenna on the measured noise figure of the system is shown.

Chapter 8

LTI and Non-LTI Comparison

This comparison on the gain-bandwidth trade-off trends of the parametrically-tuned receive antenna and the LTI antenna still needs to be discussed. The primary focus of the comparison will be based on simulated and closed form results, but the measured results of the the current fabricated prototypes are included as well. The time-varying parametric receiving antenna boasts a wider 3 dB bandwidth at the same level of effective aperture around the signal frequency compared to a conjugate matched LTI antenna of the same footprint. A comparison between the time-varying antenna and a resistively loaded LTI antenna is warranted to show the different bandwidth versus gain trade-off trends that occur for each. For the parametrically-tuned receive antenna, the gain discussed in this section refers to transducer gain rather than antenna gain in order to provide a better comparison of the simulated and fabricated antenna to the theoretical results.

8.1 LTI Antenna Gain-Bandwidth Trade-off

The gain-bandwidth trade-off for electrically small antennas is well studied and documented in the literature. For a given antenna Q or antenna footprint as well as a given radiation efficiency, the optimal gain-bandwidth relationship can be computed. This is investigated further using simulations with specific attention paid to the LTI prototype design described in 3.

8.1.1 Resistive Loading

The trade-off space is first investigated in simulation using the circuit models of the time-varying and LTI antennas discussed in 3.2.1. The electrically small LTI antenna is resistively loaded thereby decreasing the radiation efficiency. This in turn decreases the total quality factor of the antenna and increases the bandwidth as quality factor and bandwidth are inversely proportional. This can be modeled with closed form equations such as the gain of the electrically small loop antenna given by

$$G = \eta D, \tag{8.1}$$

where η is the radiation efficiency of the antenna and D is the directivity of the antenna. For electrically small loop antennas D tends towards 1.5 which is what is used for the LTI performance bound seen in Fig. 8.1 [26]. The bandwidth of the electrically small loop antenna is inversely proportional to the quality factor of the antenna as previously mentioned.

In order to study the trade-off between the gain of the electrically small loop antenna and the bandwidth it can be helpful to instead look at the radiation quality factor of the antenna rather than just the total quality factor of the antenna. The radiation quality factor of the antenna Q_{rad} takes into account only the radiation behavior of the antenna and not any behavior related to typical loss and can be found by looking at the lossless version of the antenna under test. For this investigation, a lossless version of the concentric loop antenna was simulated in HFSS and the resulting radiation quality factor was found to be 730. The approximate quality factor of the antenna at resonance can be found using the equation

$$Q(\omega_0) = \frac{\omega_0}{2R(\omega_0)}\sqrt{[R'(\omega_0)]^2 + [X'(\omega_0) + |X(\omega_0)|/\omega_0]^2}, \tag{8.2}$$

where R and X are the resistance and reactance of the antenna respectively [78]. The radiation efficiency of the antenna can then be applied to the radiation quality factor to find the total quality factor of the antenna as

$$Q = \eta Q_{rad}. \tag{8.3}$$

With the gain of the antenna and the bandwidth of the antenna–through its total quality factor–expressed in terms of radiation efficiency, the ideal trade-off trend of the concentric loop antenna can be calculated. By varying η from close to zero to one, the trade-off trend between gain and bandwidth of the concentric loop antenna can be seen in the black dotted line in Fig. 8.1.

The concentric loop antenna was also analyzed in simulation using ADS with the schematic shown in Fig. 8.2. The LTI antenna is loaded with an equal amount of resistance on both of the balanced lines of the antenna. This total impedance of the antenna including the resistive loading is then used to design a differential matching network to match to the hybrid coupler that is used as a balun.

8.2 Parametrically-Tuned Antenna Gain-Bandwidth Trade-off

The transducer gain-bandwidth trade-off of a parametrically-tuned antenna depends on a large amount of parameters. These parameters include the antenna Q and resistance at both the signal frequency and the idler frequency, the series resistance of the time-varying capacitor, the center capacitance and modulation factor of

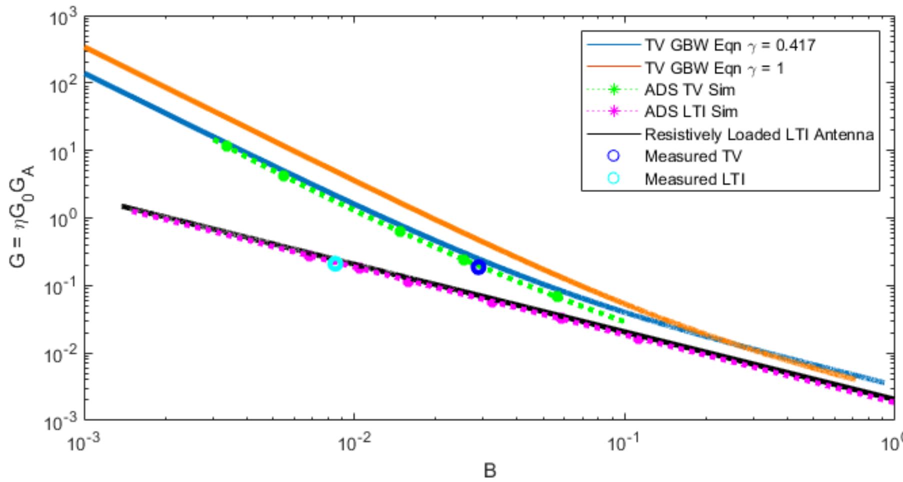

Figure 8.1: Gain-bandwidth comparison between parametrically-tuned receive antenna and the LTI antenna as load resistance is varied. The blue and orange lines represent the closed form trends for the parametrically-tuned antenna given that the antenna Q and modulation factors are fixed. The green markers represent the results from the ADS simulation of the realized parametrically-tuned receive antenna. The magenta markers represent the LTI antenna with resistive loading. The measured results of the fabricated prototypes are shown with the open circle markers

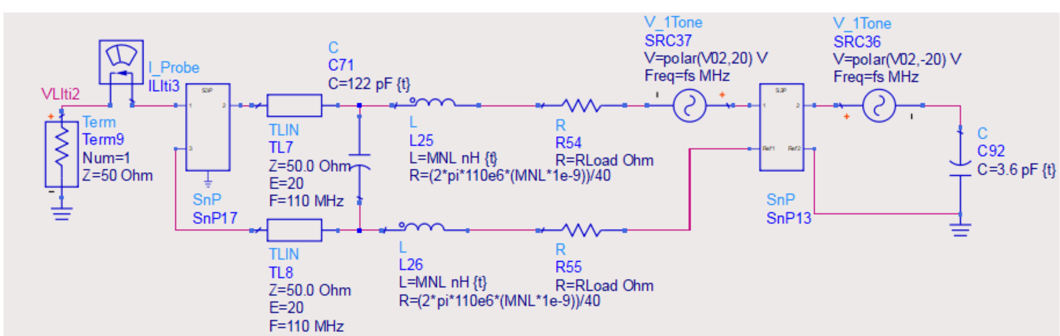

Figure 8.2: Schematic of the LTI antenna with additional resistive loading, a differential matching network, and a hybrid coupler used as a balun.

the time-varying capacitor, and the signal and idler frequencies [13]. These parameters can be used to find the maximum transducer gain of the parametrically-tuned receive antenna with

$$G_t^{max} = \frac{4R_L R_s}{[R_s^{net}(1 - |\gamma|^2 Q_s^C Q_i^C/4)]^2}, \tag{8.4}$$

where R_L is the load resistance, R_s is the resistance of the physical antenna itself at the signal frequency, and γ is the modulation factor of the time-varying capacitance [13]. R_s^{net} is the total resistance of the parametrically-tuned receive antenna at the signal frequency, defined as

$$R_{s/i}^{net} = R_L + R_s + R_c, \tag{8.5}$$

for the signal and idler frequencies respectively where R_L and R_s are as previously defined and R_c is the series resistance associated with the time-varying capacitor [13]. For the parametrically-tuned receive antenna described in this work, R_c is the total series resistance of the two SMV1232 varactors used in parallel. Q_s^C and Q_i^C are the loaded quality factors of the time-varying capacitance's effective static capacitance at the signal and idler frequencies, respectively. This can be found with

$$Q_{s/i}^C = \frac{1}{\omega_{s/i} R_{s/i}^{net} C_1}, \tag{8.6}$$

where $\omega_{s/i}$ is the signal and idler frequencies respectively and $C_1 = C_0(1 - \frac{1}{4}|\gamma|^2)$ is the effective static capacitance of the time-varying capacitor which itself is based on C_0, the average capacitance of the time-varying capacitor [13].

The theoretical bandwidth of the parametrically-tuned receive antenna can also be calculated and is given by

$$b = \frac{r_\omega(1-\overline{R})}{\sqrt{(Q_i\overline{R}+r_\omega Q_s)^2 - Q_i^2(3\overline{R}^2 - 4\overline{R}+1)}}, \tag{8.7}$$

where $r_\omega = \frac{\omega_i}{\omega_s}$ is the ratio of the idler and signal frequency [13]. $\overline{R}$ is the normalized negative resistance found with

$$\overline{R} = |\gamma|^2 Q_s^C Q_i^C/4, \tag{8.8}$$

and $Q_{s/i}$ are the loaded quality factors for the subcircuits representing the signal and idler frequencies respectively [13]. These correspond to the quality factor of the resonant base antenna at the signal frequency and the idler frequency and can be found with

$$Q_{s/i} = \frac{C_{s/i}+C_1}{\omega_{s/i}R_{s/i}^{net}C_{s/i}C_1}, \tag{8.9}$$

where $C_{s/i}$ are the capacitance values associated with the antenna at the signal and idler frequency, respectively. More details regarding the derivation of these quantities can be found in [13].

Using the transducer gain and bandwidth equations above allows for a theoretical gain-bandwidth trend line for the particular parametrically-tuned receive antenna that was implemented, fabricated, and measured as a part of this work. The trend line for modulation factor $\gamma = 0.417$ is represented in Fig. 8.1 with the solid blue line and $\gamma = 1$ is represented with the solid orange line. This rest of the parameters needed for the closed form trends such as the quality factors and resistances of the parametrically-tuned receive antenna aside from the load resistance are fixed and taken from the simulated version. The value of $\gamma = 0.417$ was chosen to match the approximate modulation factor of the simulated time-varying antenna. This was obtained by looking at the voltage swing across the varactors and referencing the datasheet for the SMV1232 [18].

The gain-bandwidth trend of the parametrically-tuned receive antenna was also investigated in simulation. The goal of the investigation in simulation was to identify the gain-bandwidth behavior of the design as the inductor in the signal matching network was adjusted. Changing this inductor would change the load impedance presented to the parametrically-tuned receive antenna thereby changing the gain and bandwidth of the device. Adjusting the load impedance seen by the parametrically-tuned receive antenna via the inductor in the signal matching network leads to the green markers shown in Fig. 8.1. The higher load impedances generated from the higher inductor values leads to an increase in bandwidth at the cost of gain. The slight discrepancy in the simulated and measured results from the closed-form results is likely due to additional losses in the simulated and fabricated design that are not accurately captured in the closed-form solution as the modulation factor between all the designs should be the same. The simulated and measured results can only extend so far due to realistic fabrication concerns. For the high gain cases, the parametrically-tuned receive antenna becomes incredibly sensitive to parasitics and other fabrication tolerances making those cases harder to simulate and measure. On the other extreme, large bandwidth cases rely on a larger load impedance which can be challenging to achieve while only changing the signal matching network inductor value. These larger inductor values also come with challenges regarding their low self-resonant frequency and increasing amounts of loss. A redesign of the signal matching network would be necessary to apply these large load impedances to the parametrically-tuned receive antenna which is not quickly feasible for the fabricated version.

While in the LTI case the gain-bandwidth trade-off is linear, the gain-bandwidth trend for the parametrically-tuned receive antenna follows a more quadratic relationship. This non-linear trend becomes more obvious in the extreme gain or extreme bandwidth regimes as more easily seen in the theoretical trend line. For the reasons discussed earlier, these extreme cases are prohibitively difficult to achieve for the fabricated prototype at this time. Dotted curve fit lines based on the marked measured and simulated results for the time-varying antenna and the LTI antenna show the approximate trends compared to the solid lines of the closed form trends. In the high gain regime, the simulated time-varying antenna is able to achieve a significant improvement in the gain-bandwidth product over the LTI counterpart, over 6.5 times. This improvement decreases as the gain decreases, but in the mid gain region where the fabricated prototypes sit the improvement factor is 3.5.

8.3 Conclusions

A comparison in the gain-bandwidth trade-off trend between the concentric loop antenna and the parametrically-tuned receive antenna has been shown. Closed form solutions for the transducer gain and bandwidth of the time-varying antenna where used from [33] along with closed form solutions of the gain and bandwidth of an electrically small LTI antenna were compared to the results found using simulation. The measured results of the fabricated prototypes were also shown and match the simulated results and trends. The parametrically-tuned receive antenna allows for a 3.5 times improvement in gain-bandwidth product, but this improvement can be further increased if bandwidth is sacrificed for higher gain. This is corroborated by the trends shown in Fig. 8.1 where the gap between the gain-bandwidth of the time-varying and LTI antennas increases in the higher gain regime.

Chapter 9

Conclusion and Future Work

In this work an electrically small, parametrically-tuned receive antenna has been implemented, fabricated, and measured. This time-varying antenna was compared to a concentric loop antenna which used the same physical footprint. The optimal matching regime for highest spectral SNR for an electrically small receive antenna was investigated and shown to be heavily dependent on the noise environment. The investigation was extended to include modulated signal analysis which took into account the bandwidth characteristics of the various matching regimes tested. These findings were used to implement conjugate matching as the matching solution for the LTI antenna as it was shown that conjugate matching is typically the best solution at the operating frequency of approximately 110 MHz.

An accurate simulation methodology using existing techniques in the literature was used to model both the LTI and time-varying antenna designs. These designs were measured using a test suite specifically developed to characterize electrically small time-varying antennas on receive. The typical receive gain measurement was modified to a cross-frequency effective aperture measurement based on existing work in the literature to eliminate the reliance on reciprocity and also consider frequency coupling phenomena that occurs with time-varying and non-LTI designs. The noise figures of the antenna receive systems were also measured using a novel method extended from the antenna Y-Factor method. This new noise figure measurement method for time-varying antennas is able to take into account both external and internal noise coupling from different harmonics into the observation frequency–a key aspect for time-varying antennas not covered by previous methods. Finally, the measurement suite includes the use of modulated signals to ensure the antennas under test are able to receive information-laden signals rather than just sense power. This modulated signal testing is not novel, but is an important inclusion in testing time-varying receive antennas to ensure there is no additional distortion due to the time-varying nature of the design.

The parametrically-tuned receive antenna implemented and measured in this work was able to achieve a 3.5 times improvement in bandwidth for the same effective aperture over the comparison LTI antenna. The gain-bandwidth trends of these antennas were explored in simulation with the gain-bandwidth improvement factor of the time-varying antenna over its LTI counterpart increasing to over 6.5 times when in a high gain regime. This higher gain state is achieved simply by decreasing the load impedance presented to the antenna which in this design can be done by decreasing the inductor in the differential matching network. The potential of electrically small parametrically-tuned receive antennas for use in size and weight constrained environments has been showcase, but there remains improvements that could be made to the design and implementation of these time-varying antennas.

9.1 Future Work

Various improvements can be made to the time-varying antenna design implemented and fabricated in this work to improve the gain-bandwidth performance. These improvements would also serve to decrease the impact of the pump source on the noise figure of the antenna and also make the design more compact.

9.1.1 Additional Parametric Receiver Improvements and Designs

The parametrically-tuned receive antenna implemented in this work could be improved in future iterations in a number of ways. The design does improve performance over a standard LTI antenna of the same footprint, but does suffer from some noise and power requirement issues. These issues can be mitigated and overall performance improved with a new design that leverages a single-balanced non-degenerate parametric amplifier design. This involves replacing the singular varactors in the design with pairs of varactors in anti-parallel [79], [80]. In the case of the prototype showcased in this work, the change in structure results in four varactors with two sets of varactors in anti-parallel. The varactors in anti-parallel seeks to isolate the idler frequency to within the varactor ring and cancel out the idler frequency outside the ring. While the complexity of feeding the varactors might increase in this configuration, the increased gain performance and the increased resilience to noise at the idler frequency should result in an overall improved design.

Significant improvements to the pump source can also lead to improved performance of the time-varying antenna prototype. While a general broadband signal generator was used as the pump source for this work, a voltage-controlled oscillator would act as a much better source. The VCO would allow for the pump source to be implemented on aperture and the lack of the wideband amplifier the signal generator incorporates would meaningfully decrease the noise present at the idler frequency. This would in turn decrease the measured noise figure of the parametrically-tuned receive antenna. The VCO and supporting circuitry could be implemented in the center of the loop antenna footprint where a null occurs in the fields of the antenna.

Potentially turning the idler resonance from a loop antenna into a lumped element circuit would also simplify the physical design. It would need to be investigated, however, if a lumped element circuit would be able to present a low enough loss and resistance at the idler and signal frequencies to enable acceptable gain-bandwidth performance.

9.1.2 Improvements to Time-Varying Receive Antenna Characterization

While this work has used a number of different measurements to characterize time-varying antennas on receive, improvements could be made to improve the implementation. The unintended emissions characterization shown in 5.2 is fairly rudimentary in its current state and could be improved to better mimic FCC or CISPR testing standards by defining elements such as device under test placement and cable layout. The multi-channel modulated signal testing in 6.2.2 could also be improved by testing in an environment better suited to low frequency measurements such as a quiet outdoor range or a larger anechoic chamber featuring lower frequency absorber. A larger test environment would eliminate the multipath issue and provide a clearer comparison between the time-varying antenna and the LTI antenna. Finally, the Y-Factor measurement could be improved by decreasing the noise figure of the receive system that does not include the antenna under test. By decreasing the noise figure of the system after the antenna, the measurement uncertainty associated with ascertaining the noise figure of the antenna by itself could be decreased. If the noise figure of the measurement system without the antenna could be decreased to below 2 dB, the noise contribution of the antenna would dominate the result and allow for a clearer understanding of the antenna noise by itself.

References

[1] L. J. Chu, "Physical limitations of omni-directional antennas," *Journal of Applied Physics*, vol. 19, no. 12, pp. 1163–1175, 1948.

[2] H. A. Wheeler, "Fundamental limitations of small antennas," *Proceedings of the IRE*, vol. 35, no. 12, pp. 1479–1484, 1947.

[3] R. F. Harrington, "Effect of antenna size on gain, bandwidth, and efficiency," *Journal of Research of the National Bureau of Standards: Radio propagation. D*, vol. 63, 1959.

[4] J. S. McLean, "A re-examination of the fundamental limits on the radiation Q of electrically small antennas," *IEEE Transactions on antennas and propagation*, vol. 44, no. 5, p. 672, 1996.

[5] M. Gustafsson, C. Sohl, and G. Kristensson, "Physical limitations on antennas of arbitrary shape," *Proceedings of the Royal Society A: Mathematical, Physical and Engineering Sciences*, vol. 463, no. 2086, pp. 2589–2607, 2007.

[6] M. Capek, M. Gustafsson, and K. Schab, "Minimization of antenna quality factor," *IEEE Transactions on Antennas and Propagation*, vol. 65, no. 8, pp. 4115–4123, 2017.

[7] D. F. Sievenpiper et al., "Experimental validation of performance limits and design guidelines for small antennas," *IEEE Transactions on Antennas and Propagation*, vol. 60, no. 1, pp. 8–19, 2011.

[8] X. Xu, H. C. Jing, and Y. E. Wang, "High speed pulse radiation from switched electrically small antennas," in *2006 IEEE Antennas and Propagation Society International Symposium*, IEEE, 2006, pp. 167–170.

[9] K. Schab, D. Huang, and J. J. Adams, "Pulse characteristics of a direct antenna modulation transmitter," *IEEE Access*, vol. 7, pp. 30 213–30 219, 2019.

[10] I. M. Broadbooks and D. F. Sievenpiper, "Coherent antenna modulation," *IEEE Transactions on Antennas and Propagation*, 2026.

[11] A. Mekawy, H. Li, Y. Radi, and A. Alù, "Parametric enhancement of radiation from electrically small antennas," *Physical Review Applied*, vol. 15, no. 5, p. 054 063, 2021.

[12] P. Loghmannia and M. Manteghi, "An active cavity-backed slot antenna based on a parametric amplifier," *IEEE Transactions on Antennas and Propagation*, vol. 67, no. 10, pp. 6325–6333, 2019.

[13] C. Blosser, "Theory and design of parametrically tuned electrically small receiving antennas," Ph.D. dissertation, University of Oklahoma, 2025.

[14] P. Loghmannia and M. Manteghi, "Broadband parametric impedance matching for small antennas using the bode-fano limit: Improving on Chu's limit for loaded small antennas," *IEEE Antennas and Propagation Magazine*, vol. 64, no. 5, pp. 55–68, 2022. DOI: 10.1109/MAP.2021.3089997

[15] A. Arora et al., "Enhancing the antenna radiation-bandwidth product with dual-tone temporal modulation," *Nature Communications*, 2026.

[16] S. F. Bass, A. M. Palmer, K. R. Schab, K. Kerby-Patel, and J. E. Ruyle, "Conversion matrix method of moments for time-varying electromagnetic analysis," *IEEE Transactions on Antennas and Propagation*, vol. 70, no. 8, pp. 6763–6774, 2022.

[17] S. R. Best and B. C. Kaanta, "A tutorial on the receiving and scattering properties of antennas," *IEEE Antennas and Propagation Magazine*, vol. 51, no. 5, pp. 26–37, 2010.

[18] *SMV123x series: Hyperabrupt junction tuning varactors*, 200058AA, Skyworks, Jan. 2020.

[19] *Frequency linear tuning varactors*, narda microwave-east.

[20] L. A. Blackwell and K. L. Kotzebue, "Semiconductor-diode parametric amplifiers," *(No Title)*, 1961.

[21] R. M. Fano, "Theoretical limitations on the broadband matching of arbitrary impedances," *Journal of the Franklin Institute*, vol. 249, no. 1, pp. 57–83, 1950.

[22] C. Tai, “On the definition of the effective aperture of antennas,” *IRE Transactions on Antennas and Propagation*, vol. 9, no. 2, pp. 224–225, 1961.

[23] S. R. Best, “Electrically small resonant planar antennas: Optimizing the quality factor and bandwidth,” *IEEE Antennas and Propagation Magazine*, vol. 57, no. 3, pp. 38–47, 2015.

[24] L. Blake, *Antenna and receiving-system noise-temperature calculation*. Naval Research Laboratory, 1961.

[25] K. Schab and K. Kerby-Patel, “Equivalent external noise temperature of time-varying receivers,” *IEEE Transactions on Antennas and Propagation*, 2025.

[26] C. A. Balanis, *Antenna theory: Analysis and design*. John Wiley & Sons, 2016.

[27] R. F. Harrington, “Time-harmonic electromagnetic fields,” *(No Title)*, 1961.

[28] B. Anderson and R. Newcomb, “On reciprocity and time-variable networks,” *Proceedings of the IEEE*, vol. 53, no. 10, pp. 1674–1674, 1965.

[29] S. Pavan and G. C. Temes, “Reciprocity and inter-reciprocity: A tutorial—Part ii: Linear periodically time-varying networks,” *IEEE Transactions on Circuits and Systems I: Regular Papers*, vol. 70, no. 9, pp. 3422–3435, 2023.

[30] J. M. Manley and H. E. Rowe, “Some general properties of nonlinear elements-Part i. general energy relations,” *Proceedings of the IRE*, vol. 44, no. 7, pp. 904–913, 1956. DOI: 10.1109/JRPROC.1956.275145

[31] J. Aumentado, “Superconducting parametric amplifiers: The state of the art in Josephson parametric amplifiers,” *IEEE Microwave magazine*, vol. 21, no. 8, pp. 45–59, 2020.

[32] C. Blosser, A. Bauer, J. E. Ruyle, K. Kerby-Patel, and K. Schab, “Signal fidelity in degenerate and nondegenerate mode parametric amplifier receiving antennas,” *IEEE Antennas and Wireless Propagation Letters*, 2024.

[33] C. Blosser, K. Schab, K. Kerby-Patel, and J. Ruyle, “Theoretical gain-bandwidth limit of parametrically tuned electrically small receiving antennas,” *IEEE Antennas and Wireless Propagation Letters*, 2026.

[34] J. Rollett, "Stability and power-gain invariants of linear twoports," *IRE Transactions on Circuit Theory*, vol. 9, no. 1, pp. 29–32, 1962.

[35] R. W. Jackson, "Rollett proviso in the stability of linear microwave circuits—A tutorial," *IEEE Transactions on Microwave Theory and Techniques*, vol. 54, no. 3, pp. 993–1000, 2006.

[36] H. T. Friis, "Noise figures of radio receivers," *Proceedings of the IRE*, vol. 32, no. 7, pp. 419–422, 1944.

[37] *Noise figure of passives*, Nov. 2010. [Online]. Available: https://www.microwaves101.com/encyclopedias/noise-figure-of-passives

[38] S. R. Best, "Realized noise figure of the general receiving antenna," *IEEE Antennas and Wireless Propagation Letters*, vol. 12, pp. 702–705, 2013.

[39] W. Lee and E. Afshari, "Low-noise parametric resonant amplifier," *IEEE Transactions on Circuits and Systems I: Regular Papers*, vol. 58, no. 3, pp. 479–492, 2010.

[40] J. Edrich, "Low-noise parametric amplifiers tunable over one full octave," *IEEE Journal of Solid-State Circuits*, vol. 7, no. 1, pp. 32–37, 1972.

[41] A. Yaghjian, "An overview of near-field antenna measurements," *IEEE Transactions on Antennas and Propagation*, vol. 34, no. 1, pp. 30–45, 1986.

[42] K. Kanaly, "Design and validation of measurement procedures for time-varying scatterers and antennas," M.S. thesis, University of Oklahoma, 2022.

[43] G. Huff, N. Soldner, W. D. Palmer, and J. Bernhard, "Study of error vector magnitude patterns (EVRP) for a transmit/receive pair of microstrip patch antennas," in *2006 IEEE Antennas and Propagation Society International Symposium*, IEEE, 2006, pp. 449–452.

[44] F. A. Miranda, C. H. Mueller, and M. A. B. Meador, "Aerogel antennas communications study using error vector magnitude measurements," in *2014 IEEE Antennas and Propagation Society International Symposium (APSURSI)*, IEEE, 2014, pp. 1149–1150.

[45] D. Brown and Y. Rahmat-Samii, “Error vector magnitude as a performance standard for antennas in the millimeter-wave era: Part 1: Metric comparisons and measurement concepts,” *IEEE Antennas and Propagation Magazine*, vol. 65, no. 5, pp. 25–34, 2023.

[46] D. Brown and Y. Rahmat-Samii, “Error vector magnitude as a performance standard for antennas in the millimeter-wave era: Part 2: Modeling, simulation, and measurement methods,” *IEEE Antennas and Propagation Magazine*, vol. 65, no. 6, pp. 10–24, 2023.

[47] Y. Yin et al., “A 37–42-GHz 8$\times$ 8 phased-array with 48–51-dBm EIRP, 64–QAM 30-Gb/s data rates, and EVM analysis versus channel RMS errors,” *IEEE Transactions on Microwave Theory and Techniques*, vol. 68, no. 11, pp. 4753–4764, 2020.

[48] K. Schab, A. Singh, and N. Bohannon, “Distortion analysis for the assessment of LTI and non-LTI transmitters,” *IEEE Transactions on Antennas and Propagation*, vol. 68, no. 7, pp. 5209–5217, 2020.

[49] K. F. Warnick, “Noise figure of an active antenna array and receiver system,” *IEEE Antennas and Wireless Propagation Letters*, vol. 21, no. 8, pp. 1607–1609, 2022.

[50] D. Buck, M. C. Burnett, and K. F. Warnick, “Experimental measurement of noise figure and radiation efficiency with the antenna Y-factor method at X-band,” *IEEE Transactions on Antennas and Propagation*, vol. 71, no. 5, pp. 3992–3996, 2023.

[51] G. J. Fisher and J. A. Connelly, “Modeling time-dependent elements for spice transient analyses,” *IEEE transactions on computer-aided design of integrated circuits and systems*, vol. 5, no. 3, pp. 429–432, 2004.

[52] K. Schab, *Multiport thevenin equivalent circuits for modeling loaded receive antennas*, Private Communication, Oct. 2022.

[53] S. E. Sussman-Fort and R. M. Rudish, “Non-Foster impedance matching of electrically-small antennas,” *IEEE Transactions on Antennas and Propagation*, vol. 57, no. 8, pp. 2230–2241, 2009.

[54] Y. E. Wang, “Theory of broadband noise matching for HF/VHF receivers with electrically small antennas,” *IEEE Access*, 2023.

[55] K. Sarabandi and M. Rao, "Bandwidth and SNR of small receiving antennas: To match or not to match," *IEEE Transactions on Antennas and Propagation*, vol. 71, no. 1, pp. 99–104, 2022.

[56] M. Microwave, "Theory of load and source pull measurement," *Application Note 5C-041*, 1999.

[57] A. Harter, "LNA matching techniques for optimizing noise figures," *RF Design*, vol. 2, no. 03, 2003.

[58] Infineon, *Infineon BFP720 SiGe:C NPN RF bipolar transistor*, https://www.infineon.com/cms/en/product/rf/rf-transistor/low-noise-rf-transistors/bfp720/, Accessed: (3/11/2024), 2018.

[59] D. M. Pozar, *Microwave engineering*. John Wiley & Sons, 2011.

[60] S. H. M. Lavasani and S. Kiaei, "A new method to stabilize high frequency high gain CMOS LNA," in *10th IEEE International Conference on Electronics, Circuits and Systems, 2003. ICECS 2003. Proceedings of the 2003*, IEEE, vol. 3, 2003, pp. 982–985.

[61] A. S. Sedra and K. C. Smith, *Microelectronic Circuits*. Oxford University Press, 2015.

[62] Texas Instruments, *OPA856 1.1-GHz unity-gain bandwidth, 0.9 nV/Hz , bipolar input amplifier*, https://www.ti.com/lit/ds/symlink/opa856.pdf?ts=1712323429682, Accessed: (3/17/2024), 2020.

[63] B. Şahinbaş, "Buffer amplifiers for an electrically small broadband antenna," M.S. thesis, Bilkent Universitesi (Turkey), 2015.

[64] K. C. Kerby-Patel and K. Schab, "Correlation properties of radio noise types in multiport systems," in *Proc. Antenna Applications Symposium*, 2023.

[65] J. A. Russer and P. Russer, "Modeling of noisy EM field propagation using correlation information," *IEEE Transactions on Microwave Theory and Techniques*, vol. 63, no. 1, pp. 76–89, 2015. DOI: 10.1109/TMTT.2014.2376962

[66] "Radio Noise," International Telecommunications Union, Geneva, Switzerland, Rec. ITU-R P.372-16, Sep. 2022.

[67] K. Schab, *D2023032_antennaandlossylctuner*, Private Communication, Mar. 2023.

[68] "Matching differential port devices, 201156b," Skyworks, Tech. Rep., Dec. 2012.

[69] "Amendment 2 - Specification for radio disturbance and immunity measuring apparatus and methods - Part 2-3: Methods of measurement of disturbances and immunity - Radiated disturbance measurements," International Electrotechnical Commission, Geneva, Switzerland: IEC, Standard, Jun. 2023.

[70] "5G; NR; User Equipment (UE) conformance specification; Radio transmission and reception; Part 1: Range 1 standalone," ETSI, Sophia Antipolis Cedex, FR, Standard, Apr. 2026.

[71] *Absorber series EHP*, v2.3, ETS-Lindgren, Mar. 2026.

[72] P. Loghmannia, "Time-Variant components to improve bandwidth and noise performance of antennas," 2021.

[73] M. Leffel and R. Daniel, "The y factor technique for noise figure measurements," Rohde & Schwarz, Munich, Germany, Tech. Rep. 1MA178, Oct. 2021. [Online]. Available: https://scdn.rohde-schwarz.com/ur/pws/dl_downloads/dl_application/application_notes/1ma178/1MA178_5e_NoiseFigure.pdf

[74] E. Woestenburg, L. Bakker, M. Ruiter, M. Ivashina, and R. H. Witvers, "THACO: A test facility for characterizing the noise performance of active antenna arrays," in *2011 41st European Microwave Conference*, IEEE, 2011, pp. 1277–1280.

[75] S. Manas, J. Gilmore, and E. Meyer, "A local hot-cold antenna measurement system," in *2021 51st European Microwave Conference (EuMC)*, IEEE, 2022, pp. 510–513.

[76] E. R. Kuhn et al., "Antenna characterization for the HIRAX experiment," in *Ground-based and Airborne Telescopes IX*, SPIE, vol. 12182, 2022, pp. 745–764.

[77] A. Geens and Y. Rolain, "Noise figure measurements on nonlinear devices," *IEEE Transactions on Instrumentation and Measurement*, vol. 50, no. 4, pp. 971–975, 2002.

[78] A. D. Yaghjian and S. R. Best, “Impedance, bandwidth, and Q of antennas,” *IEEE Transactions on Antennas and Propagation*, vol. 53, no. 4, pp. 1298–1324, 2005.

[79] S. Hayasi and T. Kurokawa, “A balanced-type parametric amplifier,” *IRE Transactions on Microwave Theory and Techniques*, vol. 10, no. 3, pp. 185–190, 2003.

[80] J. Pearson and K. Lunt, “A broadband balanced idler circuit for parametric amplifiers,” *Radio and Electronic Engineer*, vol. 27, no. 5, pp. 331–335, 1964.